Universidade de São Paulo
Instituto de Física

Estudo experimental e computacional sobre a geração de macro-emulsões e outros sistemas mediante dispositivos microfluídicos

Juan Enrique Rivero Cervantes

Orientador: Prof. Dr. Adriano Mesquita Alencar

Dissertação de mestrado apresentada ao Instituto de Física para a obtenção do título de Mestre em Ciências

Banca Examinadora:

Prof. Dr. Adriano Mesquita Alencar (IFUSP)
Prof. Dr. Prof. Mario Ricardo Gongora Rubio (IPT-USP)
Prof. Dr. Maria Cecília Barbosa da Silveira Salvadori (IFUSP)

São Paulo
2017

FICHA CATALOGRÁFICA
Preparada pelo Serviço de Biblioteca e Informação
do Instituto de Física da Universidade de São Paulo

Rivero Cervantes, Juan Enrique

Estudo experimental e computacional sobre a geração de macro-emulsões e outros sistemas mediante dispositivos microfluídicos / Experimental and computational study of generation of macro-emulsions and other systems by microfluidic devices. São Paulo, 2017.

Dissertação (Mestrado) – Universidade de São Paulo. Instituto de Física. Depto. de Física Geral.

Orientador: Prof. Dr. Adriano Mesquita Alencar
Área de Concentração: Física

Unitermos: 1. Dinâmica dos fluídos; 2. Física computacional; 3. Eletrônica; 4. Química aplicada; 5. Compostos de silício.

USP/IF/SBI-115/2017

University of São Paulo
Institute of Physics

Experimental and computational study of generation of macro-emulsions and other systems by microfluidic devices

Juan Enrique Rivero Cervantes

Adviser: Prof. Dr. Adriano Mesquita Alencar

Dissertation submitted to the Institute of Physics of the University of São Paulo in partial fulfillment of the requirements for the degree of Master of Science

Examining Committee:

Prof. Dr. Adriano Mesquita Alencar (IFUSP)
Prof. Dr. Prof. Mario Ricardo Gongora Rubio (IPT-USP)
Prof. Dr. Maria Cecília Barbosa da Silveira Salvadori (IFUSP)

São Paulo
2017

Dedicated to my family,
especially to my first parents, my grandfathers.

Acknowledgments

I want to thanks:

- My research group and family, the**LabM**^{2}, for its constantly support: the prof. Adriano, prof. Ligia, Caio, Isis, Adriana, Antonio, Alexandre, Mariana, Marcel, Jennifer, André, Yan and Luis. Many words for everyone of them. Another thesis I will write at the end of my life. I wish special thanks too, those are not longer participated; Wagner, Mariana Menegon, Marcia, Diana, Fabio, Mirian and those who I do not remember their names.
- My first mentor Juliana Schianti who introduced me the marvellous complexity and insanity of microfluidics. Special thanks to the IPT staff for allowing me the first contact with microfluidic tools.
- A special thanks to CNPEM - LMF staff for providing me the tools for microfabrication.
- Our scientific partners, FAPESP and our donor CAPES for supporting and providing me the scholarship in Master's Degree level.
- Marcelo, Marcelino and Ricardo. 70% of the Minidrop 1.0 is the result of their collaborative effort.
- Francisco Tovar and prof. Murilo Pereira for their valuable knowledge in CFD and programming. An inspirational motivation to learn more about how computers work.
- Garoa Hacker Clube, this people were and are very helpful when I am in technological troubles. Their humanity and kindness is truly contagious. I encourage to everyone to visit them to check.
- Professor Politi, one of the most strictly and serious professor I ever known in my life, but surprisingly with a very big heart.
- Vanessa Ieto, for her time and dedication in extracting that lost words from the inner of my soul and the pettiness of my mouth.
- Ao grupo de consultoria esportiva da RACE, em especial ao prof. Ricardo Arap quem me adotou numa época difícil e na qual precisava explodir como um motor guardado e superaquecido, kkkk. Ao Fabrício, os Danilos, e dezenas de amizades e irmaos que ganhei... e de graça!
- O Fernando Arruda, seu extremo carisma e grande coraçao. Espero algun dia poder te compensar, amigo.
- Opus Dei, especialmente os padres Alexandre e Adilson. Prezados amigos y mentores de toda uma vida e alma por recuperar.
- Os meus antigos amigos: Nacho, Rosita, Ingrid, Ana, Héctor e atuais irmaos da pastoral Sao Joao Baptista. A todos eles pela sua paciência infinita. Nossa, tanta coisa errada que fiz e ainda me aguentam!
- O Nedher, o Mario, o Waldir, o Denis. Amigos do alma que nunca esquecerei. As conversas, as oraçoes, seus coraçoes!, os encontros, e seus estranhos sorrisos apesar de tudo. Nunca esquecerei... com certeza.
- A Antonio De Pasq., jejeje. Caramba, jamás conocí un tipo tan extraordinario, simple y complejo en una misma persona. Uno de los regalos que pocas veces uno se encuentra en el camino, sin duda. Que nuestra amistad dure para siempre, hermano. Y sí existe el cielo, huevonazo!
- Fernando Aliaga y Fabian Firavitova. Amigos muy desiguales y diferentes uno del otro, del mío y del nuestro. Estoy agradecido por su apoyo en estos últimos meses de correría, pedaladas sanguinarias, y miles de anécdotas.
- À firma Opulence Co., quem me permitiu viver, correr, e trabalhar por novos sonhos. Encontrei ele numa lembrança com tomatos dos 8 anos.

- À comunidade do Perú, da Colômbia, da Venezuela, do Paquistao, da gringolândia. Cara, quando faltou para comer ou dormir, foram eles a quem procurei e sempre conseguí neles a minha segunda família. Cada vez que vejo atrás, penso que o mundo é um lugar possível para viver.
- Those old globetrotters, men and women I have known and I am still knowing. Thanks to your experiences and free mentorships. We will make a big house for all of us, with green meadows, forests, lakes and hundreds of ducks.
- Os companheiros moradores do CRUSP. Aprendi a descobrir a tolerância, a importância da ordem, e as minhas próprias fraquezas. Fico agradecido especialmente ao Michel, a Fabi e o Agnelo.
- À CPG da Física, O Eber, a Andreia W., e demais pessoal que vai me linchar por entregar muito tarde esta disertaçao. Obrigado pela sua paciência comigo e com todos os pósgraduandos.
- Nelson y Ana María, últimos amigos que conocí en este desvío del mestrado o como se llame. El primero por ser un amigo fiel, bondadoso y extraño... y la segunda por muchas y pequeñas cosas, por aquellas borboletas descontraídas, curiosas y antenas morenas... aquella voz cantante y feliz que incomoda mi cabeza porque ya no podré escucharla más.
- Finalmente a mi padre y madre aún en vida. Aquellos señores les doy las gracias por la vida. Todo lo que soy, 1% lo tengo de ellos y ellos 100% de mi. Son tan iguales a mi, y yo tan diferente de ellos. Los quiero, padrecitos.

Tudo é permitido, mas nem tudo é oportuno.
Tudo é permitido, mas nem tudo edifica
São Paulo

Resumo

A microfluídica consiste na manipulação de fluidos da ordem de picolitros, o que leva ao uso mínimo de reagentes assim como o baixo custo de material químico e analitos [1]. Há alguns anos, muitos desenvolvimentos e aplicações têm focado em mostrar que métodos tradicionais de alto custo podem ser simplificados em dispositivos de grandeza consideravelmente menores, mais conhecidos como sistemas "lab-on-a-chip". Alguns exemplos deles podemos mencionar: dispositivos baseados em materiais viscoelásticos mediante soft-lithogaphy [2], sistemas baseados em papel ouμPADs - microfluidics paper analytical devices [3], entre outros. Alternativamente, métodos numéricos como o método dos elementos finitos (FEM) [4] tem permitido o desenvolvimento da fluidodinâmica computacional, a qual permite uma análise e adaptação ao nível da microfluídica.

Neste trabalho, nós focamos na geração de emulsões simples, tanto na parte experimental, desde a fabricação dos dispositivos com microcanais e a construção de bombas de infusão, como a parte computacional baseado em OpenFoam. Esta última aplicação usando como princípio a hidrofobicidade [5, 6] das paredes internas dos dispositivos microfluídicos.

Palavras-chave: Microfluídica, Microcontroladores, Litografía suave, Dinânica dos fluidos computacional.

Abstract

Microfludics concerns the manipulation of fluids at the order of some picoliters, which leads to the use of minimum of reactant, and therefore relative low cost of chemical reactants and analytes [1]. Some years ago, multiple applications have been developed in order to show that traditional expensive experiments can be simplified into simple chips. Some examples: the use of certain elastomers like PDMS, some ceramic materials as low-temperature co-fired ceramic (LTCC) modules [7], the developement of μPADs - microfluidics paper analytical devices [3], among others. Alternatively, along some decades, the finite element methods (FEM) [4] has provided, the computational fluid dynamics (CFD) which permits the support and adaptation for analysis for microfluidics.

In this work, we focus in the generation of simple emulsions, and illustrate the experimental and theoretical method for reaching them. Experimentally, by using softlithography techniques for building microdevices on polydimethylsiloxane (PDMS) materials, and by using an open source hardware Arduino [8] for programming and controlling a system of syringe infusion. Parallelly, such emulsions are obtained too in an open source computational method based on OpenFoam [9], using a suitable method regarding the wettability [5, 6] of the inner microchannel walls.

Keywords: Microfluidics, Microcontrollers, Soft lithography, Fluid Dynamics Computational.

Contents

1. Introduction

What is microfluidics?

Microfluidics is the science and the set of technologies involved in the study and manipulation of fluids at the micrometer scale, this is operating in volumes between 10^{-9} and 10^{-18} litres [1]. Common devices include whole blood samples, bacterial cell suspensions, protein or antibody solutions and various buffers. Microfluidics devices can be used to obtain a variety of measurements including diffusion coefficients [10], fluid viscosity [11, 12], pH [13], and enzyme reaction kinetics [14, 15]. Other popular applications include cell manipulation [16, 17], cell separation [18] and cell sorting [19], DNA expression and transfection [20], capillary electrophoresis [2] and digital microfluidics [21, 22].

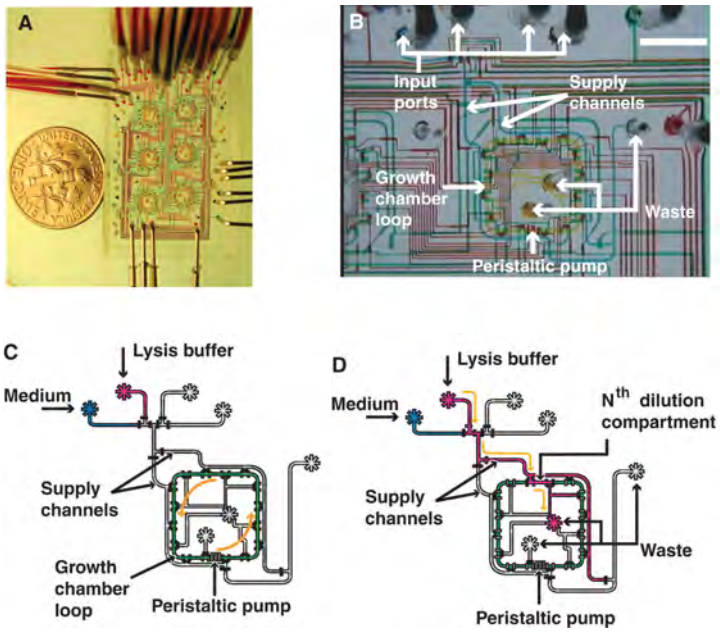

Figure 1.1.: Microfluidic systems for cell culture.

The implementation of microfluidics includes many technologies from the fabrication of microchannels, control or develepment of micropumping systems, optics arrangement, imaging processing for results, etc. The Fig. 1.1 shows a complex system for microfluidic cell culture.

The next Fig. 1.2, developed by the Royal Melbourne Institute of Technology (RMIT) in Australia, shows a microfluidic system that simulates the heart, which we are in strong collaboration. Our research group has enhanced cardiac cells culture methods during the past two years.

By the other hand, since more than 35 years, micropumping research has been an area of extensive research [23] for specialized applications, including electroosmotic, electrohydrodynamic and magnetohydrodynamic micropumps. Many efforts has been done in the

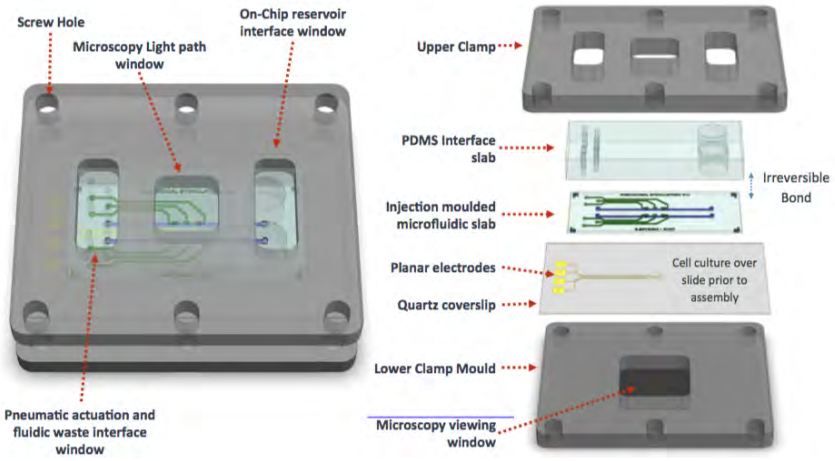

Figure 1.2.: Microfluidic system for heart simulink developed by the RMIT.

reciprocating displacement micropumps with piezoelectric drivers, used commonly in printers.

Present and future of microfluidics

Currently a high demand is leading by molecular diagnosis. Infectious diseases diagnostics are currently taking advantage of these developments at the sample preparation level. Tomorrow it enables new possibilities in oncology diagnostics (i.e. liquid biopsy and genetic testing). (Sebastian Clerc, Yole Developpment). See Fig. 1.3.

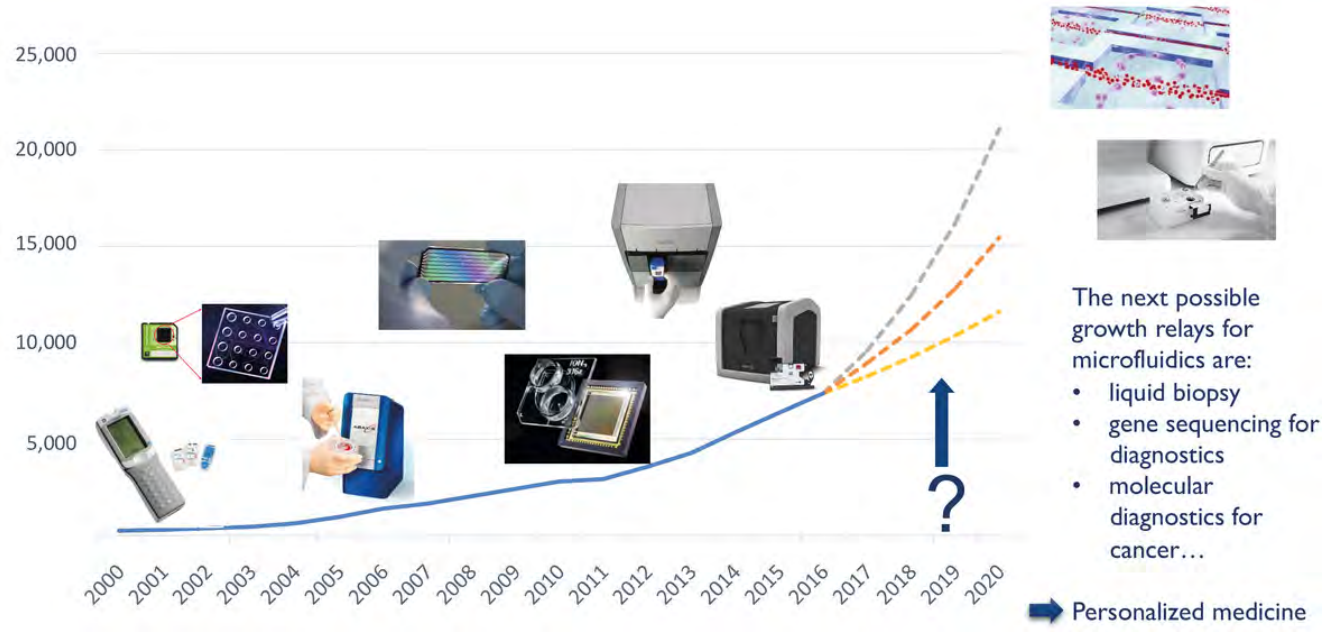

Figure 1.3.: Present and future of microfluidics. Source: Status of Microfluidics Industry 2017 report, May 2017, Yole Developpment.

Today, these applications are still driving the microfluidics industry's growth and struc-

ture. From microfluidic devices like manufactured chips, delivery tools, and dispensers, microfluidic-based products are then provided to end-users, offering numerous possibilities. Organs-on-Chips are a promising as an interesting application as well.

Interesting applications

Generation of emulsions

Microfluidic techniques can generate emulsion droplets with precisely controlled size, shape, and composition, which provide excellent templates for synthesis of functional microparticles with controllable size and shape and versatile compositions, MaojieZhang (2016). This is favorable under spatially patterned surface modification using flow confinement, Adam R. Abate (2010). See Fig. 1.4

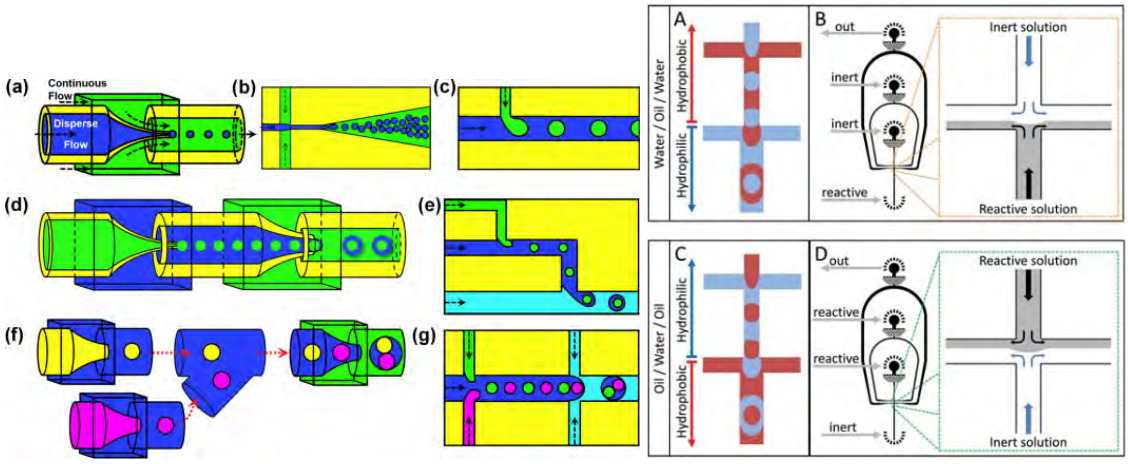

Figure 1.4.: Left: Microfluidic devices for controllable generation of monodisperse emulsions. MaojieZhang (2016). Right: Wettability pattern modification for multiple emulsion. Adam R. Abate (2010).

μPADs

Microfluidic paper-based analytical devices (μPADs) are a new class of point-of-care diagnostic devices that are inexpensive, easy to use, and designed specifically for use in developing countries. See Fig. 1.5

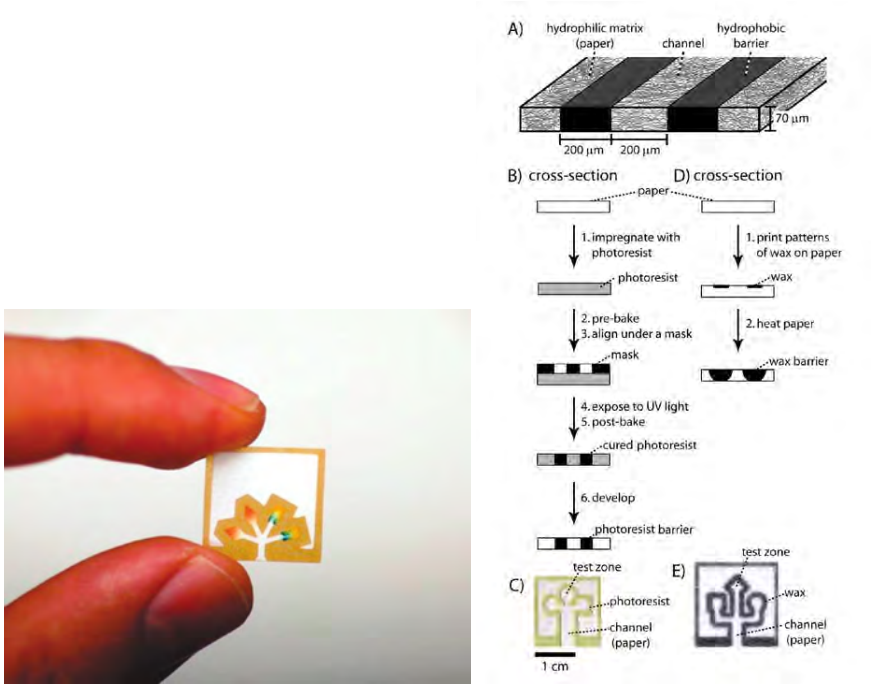

Figure 1.5.: Schematic of a paper-based microfluidic channel. The channel comprises a porous matrix of hydrophilic cellulose, Emanuel Carrilho (2010).

Oil recovery

Microfluidic devices can be useful tools in investigation and visualization of processes used in the oil and gas industry as fluid propagation, flooding, fracturing, emulsification and many others. Critical macro-scale processes that define oil extraction and recovery are controlled by the micro-scale processes based on wetting, adhesion, surface tension, colloids and other concepts of microfluidics. See Fig. 1.6.

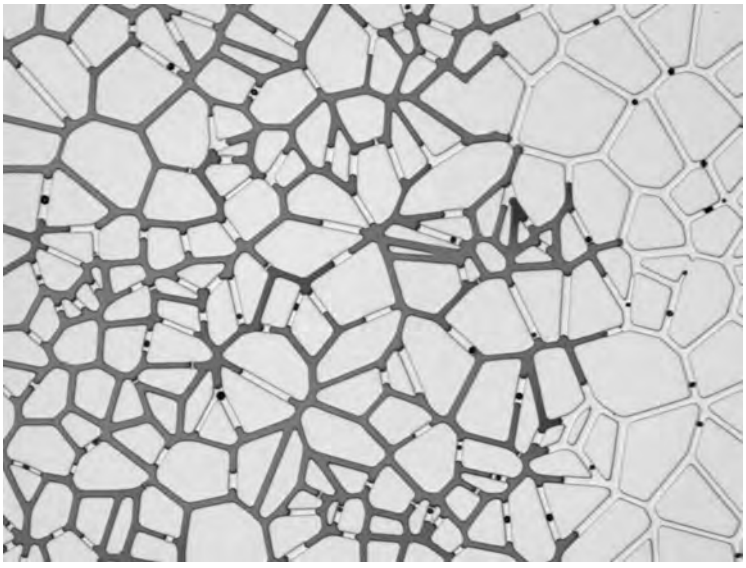

Figure 1.6.: Study of the effect of pore geometry and interfacial tension on water-oil displacement efficiency. Xiaolong Yin (2014).

1.1. Motivation

The lack of physicists in microfluidics, in the world and particularly in Brazil, the majority of research groups being analytical chemistry, biology, microbiology, etc. leads to us attracted in the real posibility of studying the world on micro-things manipulation. Particularly, we are interested in generating a complex fluid similar to blood: a fluid with emulsions in the size order of red blood cells in a chip. A collaboration with the RMIT group of microfluidics is shown in Fig. 1.7.

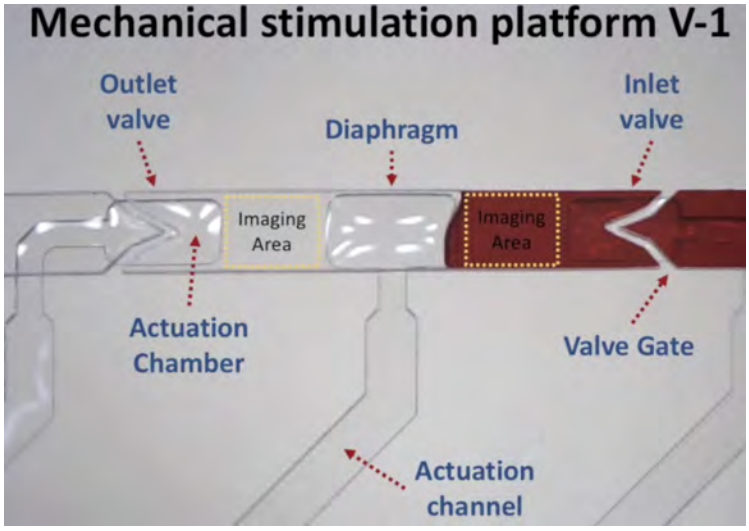

Figure 1.7.: Heart simulink generated in a microfluidic device.

In this work we focus in the generation of simple emulsions and illustrate the method for reaching such emulsions [6, 5] in microfludics, using an open source hardware Arduino [8], for pumping fluids on polydimethylsiloxane (PDMS) materials. Parallelly we show a open source computational method based on OpenFoam [9], using a suitable method for suitable multiphase mixture at the macroscale at the present stage.

Personally, the vast research areas for studying and developing has been and will be an enormous source of constantly learning.

1.2. Objectives

The main goal of our work was to build an experimental and theoretical microfluidics framework at $\mathbf{LabM}^2$ while investigating the generation and fluid flow of micro emulsions solutions at different flow rates and geometries. This is important under the perspective mimicking blood stream at small capillary vessels, among others applications.

Thus our specific aims to reach these goals was to:

- To develop and implement a system for microfluidics applications including the fabrication of microstructures as microchannels.
- Implement the control and automation of infusion liquids based on motor steppers controlled by an ATMega328 microcontroller.

- Focus in an application: to get simple emulsions by microfluidic devices.
- To adapt a computational based method for multiphase systems to generate such emulsions in an open source software for computational fluid dynamics (CFD), especifically OpenFOAM.

2. Governing equations

In this chapter we will formulate the general description of fluid dynamics necessary for the understanding of this work. Its mathematical description uses a variety of field variables as scalars, vectors and tensors. In the first part, we will refer to fluids which there are not internal forces and therefore the equations which represents the ideal fluids only contain *scalars*; such as density, pressure, temperature, etc., and *vectors*; such as velocity and external forces. In the second part, we will discuss non ideal fluids, where there are internal forces or energy dissipation and tensors are used.

2.1. Ideal Fluids

Fluid Dynamics concerns about the study of motion of fluids, liquids and gases. Usually as a macroscopic phenomena, in general, the fluid is considered as a continuous medium. From now on let us regard a fluid particle as a small volume element, very small compared with the volume of the body under consideration, but large compared with the distances between the constitutive molecules.

The mathematical description of a moving ideal fluid is completely determined by the three components of the velocity $\boldsymbol{v} = \boldsymbol{v}(x, y, z)$ of the element unit and any two thermodynamical quantities of the fluid such as pressure p, temperature T, density ρ, etc. It is frequently to use the pressure $p = p(x, y, z)$ and the density $\rho = \rho(x, y, z, t)$, since they are the most common quantities used. These thermodynamic quantities with the equation of state are enough to determine any other thermodynamic quantity.

Since we are dealing with five variables we need to derive five fundamental equations of fluid dynamics. In this chapter we discuss how to accomplish them.

2.1.1. The equation of continuity

The first of the fundamental equations of fluid dynamics concerns with the conservation of mass. Let us consider a fluid volume Ω and denote its surface by $\partial\Omega$ in which we analyze a mass of fluid passing through a surface element $\mathrm{d}a\,\mathbf{n}$, given by $\rho\boldsymbol{v} \cdot \mathrm{d}a\,\mathbf{n}$. The total flux of fluid mass through Ω is:

$$\phi_t = \oint_{\partial\Omega} \rho\boldsymbol{v} \cdot \mathrm{d}a\,\mathbf{n} \qquad , \tag{2.1}$$

where the integration was taken over the whole volume Ω. At the same time, the decrease, per unit time, of this volume is

$$\phi_t = -\frac{\partial}{\partial t}\int_\Omega \rho \mathrm{d}\mathbf{r} \qquad , \tag{2.2}$$

combining the two expressions,

$$\oint_{\partial\Omega} \rho\boldsymbol{\upsilon}\cdot \mathrm{d}a\,\mathbf{n} = -\frac{\partial}{\partial t}\int_\Omega \rho \mathrm{d}\mathbf{r} \qquad . \tag{2.3}$$

By using the Green's theorem to a volume integral, we obtain

$$\oint_{\partial\Omega} \rho\boldsymbol{\upsilon}\cdot \mathrm{d}a\,\mathbf{n} = \int_\Omega \boldsymbol{\nabla}\cdot(\rho\boldsymbol{\upsilon}) \mathrm{d}\mathbf{r} \qquad , \tag{2.4}$$

$$\int_\Omega \Big[\frac{\partial\rho}{\partial t} + \boldsymbol{\nabla}\cdot(\rho\boldsymbol{\upsilon})\Big]\mathrm{d}\mathbf{r} = 0 \qquad , \tag{2.5}$$

which must be hold for any volume,

$$\frac{\partial\rho}{\partial t} + \boldsymbol{\nabla}\cdot(\rho\boldsymbol{\upsilon}) = 0 \qquad \text{or} \qquad \partial_t\rho = -\boldsymbol{\nabla}\cdot\mathbf{J} \qquad , \tag{2.6}$$

which is called the *Equation of Continuity*, where the vector $\mathbf{J}(\mathbf{r},\, t) = \rho(\mathbf{r},\, t)\boldsymbol{\upsilon}(\mathbf{r},\, t)$ is the *mass flux density* vector defined as the mass density ρ times the convection velocity $\boldsymbol{\upsilon}$, where its magnitude indicates the mass of fluid moving out. Using the Einstein notation where the same index label implicity implies a summatory, the equation of continuity can be written as:

$$\partial_t\rho = -\partial_j(\rho\upsilon_j) \qquad . \tag{2.7}$$

At the microscopy scale, where the velocities are much smaller compared to propagation of sound in the fluid, we can treat the fluid as incompressible, ρ is constant in space and time,

$$\boldsymbol{\nabla}\cdot\boldsymbol{\upsilon} = 0 \qquad \text{or} \qquad \partial_j\upsilon_j = 0 \qquad , \tag{2.8}$$

which is a result we shall see extensively in this work.

2.1.2. Euler's equation

We have to remark that the velocity $\boldsymbol{v}(x, y, z, t)$ makes reference to the velocity at a given fixed point (x, y, z) in space and at given time t and not to a specific to particles of the fluid. The same remark is applied to density and pressure.

Considering a fluid into a volume Ω, by applying a force $\mathbf{f}$ due to the pressure in the surrounding of this volume we have,

$$\mathbf{f} = \oint_{\partial\Omega} p \cdot \mathrm{d}a\, \mathbf{n} \qquad . \tag{2.9}$$

which is equivalent, using the Green's theorem,

$$\mathbf{f} = -\oint_{\partial\Omega} p\mathrm{d}a\, \mathbf{n} = -\int_{\Omega} \boldsymbol{\nabla} p \mathrm{d}\mathbf{r} \qquad . \tag{2.10}$$

We can write now the equation of motion of a volume element in the fluid by expliciting this force to the resultant force,

$$\mathbf{f} = \int_{\Omega} \rho \frac{\mathrm{d}\boldsymbol{v}}{\mathrm{d}t} \mathrm{d}\mathbf{r} \qquad . \tag{2.11}$$

which is the product of mass per unit volume, ρ, and the acceleration, $\frac{\mathrm{d}\boldsymbol{v}}{\mathrm{d}t}$. Thus, we obtain

$$\rho \frac{\mathrm{d}\boldsymbol{v}}{\mathrm{d}t} = -\boldsymbol{\nabla} p \qquad . \tag{2.12}$$

Notice that from now on, everytime we refer to mass m we refering to ρ.

By extending the total derivative of the velocity, in terms of temporal and spatial terms,

$$\frac{\mathrm{d}\boldsymbol{v}}{\mathrm{d}t} = \frac{\partial \boldsymbol{v}}{\partial t} + (\boldsymbol{v} \cdot \boldsymbol{\nabla})\boldsymbol{v} \qquad , \tag{2.13}$$

which is called the *substantial* time derivative, to emphasize its connection with a moving substance. Combining these two last expressions, we reach to:

$$\frac{\partial \boldsymbol{v}}{\partial t} + (\boldsymbol{v} \cdot \boldsymbol{\nabla})\boldsymbol{v} = -\frac{1}{\rho} \boldsymbol{\nabla} p \qquad , \tag{2.14}$$

which is known as *Euler's Equation.*

The absent of heat exchange can be expressed in terms of the entropy s constancy,

$$\frac{\mathrm{d}s}{\mathrm{d}t} = 0 \qquad . \tag{2.15}$$

which is the adiabatic condition for ideal fluids. It expresses the idea of no having internal forces involved, as friction. Therefore, the Eq. (2.15) and the three Euler's equation, one for each component, are the last four equations needed for the mathematical description of any problem on ideal fluids.

2.1.3. Bernoulli's equation

Let us try to reduce the Euler's equation for a steady flow, by steady flow we mean that its velocity is constant in time, $\partial \boldsymbol{v}/\partial t = 0$. Considering the thermodynamic relations per unit mass,

$$\mathrm{d}h = T\mathrm{d}s + V\mathrm{d}p \qquad , \tag{2.16}$$

where h is the enthalpy per unit of mass of fluid, $V = 1/\rho$ is the specific volume and T is the temperature. Since s is constant, we may deduce straightforward that $(\boldsymbol{\nabla} p)/\rho = \boldsymbol{\nabla} h$. Therefore the Euler's equation can be expressed as:

$$\frac{\partial \boldsymbol{v}}{\partial t} + (\boldsymbol{v} \cdot \boldsymbol{\nabla})\boldsymbol{v} = -\boldsymbol{\nabla} h \qquad . \tag{2.17}$$

By using the vector identity,

$$\frac{1}{2}\boldsymbol{\nabla} v^2 = \boldsymbol{v} \times \boldsymbol{\nabla} \times \boldsymbol{v} + (\boldsymbol{v} \cdot \boldsymbol{\nabla})\boldsymbol{v} \qquad , \tag{2.18}$$

we may rewrite the Eq. (2.17) in the form:

$$\frac{\partial \boldsymbol{v}}{\partial t} - \boldsymbol{v} \times \boldsymbol{\nabla} \times \boldsymbol{v} = -\boldsymbol{\nabla}(h + \frac{1}{2}v^2) \qquad . \tag{2.19}$$

In the case of a steady flow, this reduces to

$$\boldsymbol{v} \times \boldsymbol{\nabla} \times \boldsymbol{v} = \boldsymbol{\nabla}(h + \frac{1}{2}v^2) \qquad . \tag{2.20}$$

In steady flow we use a recurrent term,*streamline* which we mean as a line such that the tangent at any point gives the direction of the velocity at that point. In steady flow, the

streamlines coincide with the paths of fluid particles, which no longer occurs in non-steady flow. The projection of $\boldsymbol{\nabla} h$ over the streamline at each point is $\partial h/\partial l$. The vector $\boldsymbol{v} \times \boldsymbol{\nabla} \times \boldsymbol{v}$ is perpendicular to $\boldsymbol{v}$, and its projection over such direction is zero. Thus, by projecting the Eq. (2.20) over the streamline we have,

$$\frac{\partial}{\partial l}(\frac{1}{2}v^2 + h) = 0 \qquad . \tag{2.21}$$

Therefore, along a streamline:

$$\frac{1}{2}v^2 + h = \text{constant} \qquad , \tag{2.22}$$

which is called *Bernoulli's Equation*.

2.2. Viscous Fluids

In this part, we introduce the concept of tensor through internal viscous forces or internal dissipation occurring during the motion of a fluid. In the next section we still concern about an ideal fluid to be explicitly more consistent in the successive about the importance of the components of a tensor field variable.

2.2.1. The momentum flux

Let us start by expanding the momentum derivative $\partial(\rho \boldsymbol{v})/\partial t$, and use the tensor notation.

$$\frac{\partial}{\partial t}\big(\rho v_i\big) = \rho \frac{\partial v_i}{\partial t} + v_i \frac{\partial \rho}{\partial t} \qquad . \tag{2.23}$$

From the continuity and the Euler's equations, Eq.(2.7) and Eq.(2.14) respectively, in the tensorial form,

$$\frac{\partial \rho}{\partial t} = -\frac{\partial(\rho v_k)}{\partial x_k} \qquad , \tag{2.24}$$

$$\frac{\partial v_i}{\partial t} = -v_k \frac{\partial v_i}{\partial x_k} - \frac{1}{\rho}\frac{\partial p}{\partial x_i} \qquad , \tag{2.25}$$

into the Eq. (2.23), we obtain,

$$\frac{\partial}{\partial t}\big(\rho \upsilon_i\big) = -\rho \upsilon_k \frac{\partial \upsilon_i}{\partial x_k} - \frac{\partial p}{\partial x_i} - \upsilon_i \frac{\partial (\rho \upsilon_k)}{\partial x_k} \qquad , \tag{2.26}$$

then grouping the first and third term of the right-hand side of the above equation,

$$\frac{\partial}{\partial t}\big(\rho \upsilon_i\big) = -\frac{\partial p}{\partial x_i} - \frac{\partial}{\partial x_k}(\rho \upsilon_i \upsilon_k) \qquad . \tag{2.27}$$

Writing the gradient of the pressure in the tensorial form,

$$\frac{\partial p}{\partial x_i} = \delta_{ik} \frac{\partial p}{\partial x_k} \qquad , \tag{2.28}$$

and from Eq. (2.27), we finally arrive to,

$$\frac{\partial}{\partial t}\big(\rho \upsilon_i\big) = \frac{\partial \Pi_{ik}}{\partial x_k} \qquad , \tag{2.29}$$

where Π_{ik} is defined as,

$$\Pi_{ik} = p\delta_{ik} + \rho \upsilon_i \upsilon_k \qquad . \tag{2.30}$$

This tensor is called the *momentum flux density tensor*. To see the meaning of this tensor field, let us make a volume integration in Eq. (2.29),

$$\frac{\partial}{\partial t} \int_\Omega \rho \upsilon_i \mathrm{d}\mathbf{r} = -\int_\Omega \frac{\partial \Pi_{ik}}{\partial x_k} \mathrm{d}\mathbf{r} \qquad , \tag{2.31}$$

which we transform into a surface integral by Green's theorem ,

$$\frac{\partial}{\partial t} \int_\Omega \rho \upsilon_i \mathrm{d}\mathbf{r} = -\oint \Pi_{ik} \mathrm{d}a_k \qquad . \tag{2.32}$$

The left-hand side is the rate of change of the ith component of the momentum contained in the volume considered, Ω. Meanwhile in the right-hand side, we have the amount of momentum flowing out through the bounding surface. Therefore $\Pi_{ik}\mathrm{d}a_k$ is the ith component of the momentum flowing through the surface element $\mathrm{d}a$. An interesting meaning of this component may be deduced by writing $\mathrm{d}a_k$ as $\mathrm{n}_k \mathrm{d}a$ where $\mathrm{d}a$ is the area of the surface

element and n_k is one of the components of the unit vector $\mathbf{n}$ along the outward normal. As a result, it is clear that $\Pi_{ik}n_k$ is the flux of the ith component of the momentum through the unit surface area.

Using the relation (2.30), $\Pi_{ik}n_k = pn_k + \rho v_i v_k n_k$. Which in vector form is,

$$p\mathbf{n} + \rho\boldsymbol{v}(\boldsymbol{v}\cdot\mathbf{n}) \qquad , \tag{2.33}$$

obtaining the momentum flux density in the direction of $\mathbf{n}$. That is, through a surface perpendicular to $\mathbf{n}$. In particular, taking the unit vector $\mathbf{n}$ to be in the same direction parallel to vector velocity, we have the longitudinal component of momentum transported in this direction, and its flux density as:

$$p + \rho v^2 \qquad . \tag{2.34}$$

On the other hand, if the unit vector is perpendicular to the velocity, only the transverse component of the momentum is transported. And its flux density being just p.

In summary, $\Pi_{ik} = \rho v_i v_k + p\delta_{ik}$, represents a completely reversible transfer of momentum due to mechanical transport of different particles of fluid from place to place and to the pressure forces acting in the fluid.

2.2.2. The Navier-Stokes equation

The effect of the energy dissipation, occurring during the motion of a fluid, is the result of thermodynamic irreversibility of the motion. This is thermal conduction. The equation of continuity remains unchangeable, due to the conservation of mass, whether the fluid is viscous or not. Meanwhile Euler's equation requires modification.

From the Euler's equation expressed in terms of the momentum flux tensor in the form of Eq. (2.29) with the tensorial term $\Pi_{ik} = \rho v_i v_k + p\delta_{ik}$, the motion of a viscous fluid (internal friction) is due to another irreversible transfer of momentum from points where the velocity is large to those where it is small. We represent this term by $-\sigma'_{ik}$, which gives the irreversible "viscous" transfer of momentum in the fluid,

$$\Pi_{ik} = \rho v_i v_k + p\delta_{ik} - \sigma'_{ik} \qquad , \tag{2.35}$$

or

$$\Pi_{ik} = \rho v_i v_k - \sigma_{ik} \qquad , \tag{2.36}$$

where the tensor σ_{ik} is called the *stress tensor*, and σ'_{ik} the *viscosity stress tensor*. Keeping in mind the following arguments about the nature of this last tensor: 1) The viscosity stress

processes occur when the fluid particles move with different velocities, so it is present a relative motion between the particles and therefore σ'_{ik} must depend in the space derivatives of the velocity. If we suppose these velocity gradients are small, σ'_{ik} will depend only on the first derivatives of the velocity; 2) In uniform rotation with angular velocity $\dot{\boldsymbol{\theta}}$ there is not relative motion, consequently not internal friction occurs. Considering these two facts we may give a trial function for the viscosity stress tensor,

$$\sigma'_{ik} = \frac{\partial \upsilon_i}{\partial x_k} + \frac{\partial \upsilon_k}{\partial x_i} \qquad . \tag{2.37}$$

This expression is a linear combination of the space derivatives and vanishes when $\boldsymbol{\upsilon} = \dot{\boldsymbol{\theta}} \times \mathbf{r}$, $\partial \upsilon_i / \partial x_k = \dot{\theta}_j$, $\partial \upsilon_k / \partial x_i = -\dot{\theta}_j$, where $\dot{\boldsymbol{\theta}}$ is a constant. We choose such symmetric form in Eq. (2.37) for σ'_{ik} just to maintain the original symmetry for the stress tensor. The most general tensor of rank two satysfying the mentioned conditions is

$$\sigma'_{ik} = \eta\Big(\frac{\partial \upsilon_i}{\partial x_k} + \frac{\partial \upsilon_k}{\partial x_i} - \frac{2}{3}\delta_{ik}\frac{\partial \upsilon_l}{\partial x_l}\Big) + \zeta \delta_{ik}\frac{\partial \upsilon_l}{\partial x_l} \qquad , \tag{2.38}$$

with η and ζ independent of the velocity[1], and called as *coefficients of viscosity* and further we show they both are positive. The coefficient ζ is known as *second viscosity*. The expression in parenthesis vanishes on contraction with respect to i and k.

To express the equation of motion of a viscous fluid, we add directly the expanded terms in $\partial \sigma'_{ik}/\partial x_k$ to the righ-hand side of Euler's equation

$$\rho\left(\frac{\partial \upsilon_i}{\partial t} + \upsilon_k \frac{\partial \upsilon_i}{\partial x_k}\right) = -\frac{\partial p}{\partial x_i} \qquad . \tag{2.39}$$

Thus we have,

$$\rho\Big(\frac{\partial \upsilon_i}{\partial t} + \upsilon_k \frac{\partial \upsilon_i}{\partial x_k}\Big) = -\frac{\partial p}{\partial x_i} + \frac{\partial}{\partial x_k}\Big\{\eta\Big(\frac{\partial \upsilon_i}{\partial x_k} + \frac{\partial \upsilon_k}{\partial x_i} - \frac{2}{3}\delta_{ik}\frac{\partial \upsilon_l}{\partial x_l}\Big)\Big\} + \frac{\partial}{\partial x_i}\Big(\zeta \frac{\partial \upsilon_l}{\partial x_l}\Big) \qquad , \tag{2.40}$$

$$\rho\Big(\frac{\partial \upsilon_i}{\partial t} + \upsilon_k \frac{\partial \upsilon_i}{\partial x_k}\Big) = -\frac{\partial p}{\partial x_i} + \eta\Big(\frac{\partial^2 \upsilon_i}{\partial x_k \partial x_k} + \frac{\partial}{\partial x_i}\frac{\partial \upsilon_k}{\partial x_k} - \frac{2}{3}\frac{\partial}{\partial x_i}\frac{\partial \upsilon_l}{\partial x_l}\Big) + \zeta \frac{\partial}{\partial x_i}\frac{\partial \upsilon_l}{\partial x_l} \qquad , \tag{2.41}$$

$$\rho\Big(\frac{\partial \upsilon_i}{\partial t} + \upsilon_k \frac{\partial \upsilon_i}{\partial x_k}\Big) = -\frac{\partial p}{\partial x_i} + \eta\frac{\partial^2 \upsilon_i}{\partial x_k \partial x_k} + \Big(\zeta + \frac{1}{3}\eta\Big)\frac{\partial}{\partial x_i}\frac{\partial \upsilon_l}{\partial x_l} \qquad . \tag{2.42}$$

[1]In the Eq. (2.43), the quantities of η and ζ are functions of pressure and temperature. What is more, in general p and T, and therefore η and ζ, are not constant throughout the fluid, so they strictly can not be taken outside any gradient operator.

In vector form we notice that $\partial v_l/\partial x_l \equiv \nabla \cdot \boldsymbol{v}$ and $\partial^2 v_i/\partial x_k \partial x_k \equiv \triangle v_i$ therefore the equation will be:

$$\rho\Big[\frac{\partial \boldsymbol{v}}{\partial t} + \Big(\boldsymbol{v}\cdot\boldsymbol{\nabla}\boldsymbol{v}\Big)\Big] = -\boldsymbol{\nabla}p + \eta\triangle\boldsymbol{v} + \Big(\zeta + \frac{1}{3}\eta\Big)\nabla(\boldsymbol{\nabla}\cdot\boldsymbol{v}) \qquad , \tag{2.43}$$

By considering the fluid as incompressible, $\nabla \cdot v = 0$, the equation of motion for an incompressible viscous fluid is

$$\rho\Big[\frac{\partial \boldsymbol{v}}{\partial t} + \Big(\boldsymbol{v}\cdot\boldsymbol{\nabla}\boldsymbol{v}\Big)\Big] = -\boldsymbol{\nabla}p + \eta\nabla^2\boldsymbol{v} \qquad . \tag{2.44}$$

which is known as *Navier-Stokes Equation*. And correspondingly, the stress tensor for an incompressible fluid in this kind of fluid is

$$\sigma_{ik} = -p\delta_{ik} + \eta\Big(\frac{\partial v_i}{\partial x_k} + \frac{\partial v_k}{\partial x_i}\Big) \qquad . \tag{2.45}$$

We can observe that viscosity of an incompressible fluid depends only of one coefficient, η. Most of fluids can be considered practically incompressible.

The ratio

$$\nu = \frac{\eta}{\rho} \qquad , \tag{2.46}$$

is called the *kinematic viscosity* (while η itself is called *dynamic viscosity*). At a temperature of 20 °C we have some values of η and ζ for various fluids:

	η(g/cm sec)	ν(cm^2/sec)
Water	0.010	0.010
Air	0.00018	0.150
Alcohol	0.018	0.022
Glycerine	8.5	6.8
Mercury	0.0156	0.0012

Two interesting remarks here, because of the water density, the kinematic and dynamic viscosity are the same. In alcohol and glicerine they both are approximately the same. Two opposite situations for the kinematic viscosity occurs in the air and mercury fluids. The air density is too low and mercury considerably high.

2.2.3. The dimensionless Reynolds number and Stokes flow

In the Navier-Stokes equation there is a non-linear term $(\boldsymbol{v}\cdot\boldsymbol{\nabla})\boldsymbol{v}$. All the interesting phenomena of fluid dynamics is due to this non-linearity, which ironically makes the equation

more complex and, even more, the solutions of the equation has never been characterized. However, in the regime of microfluidic systems the non-linear term is not relevant, leading to the *Stokes flow*[2]. A practical way to analyse this is making the Navier-Stokes equation dimensionless.

Using the parameters with dimensions $[U_0] = [\text{lenght} \cdot \text{seg}^{-1}]$, $[L_0] = [\text{lenght}]$, $[\rho] = [\text{mass} \cdot \text{lenght}^{-3}]$ and $[\eta] = [\text{mass} \cdot \text{lenght}^{-1} \cdot \text{seg}^{-1}]$, it is possible to bind a dimensionless number,

$$R_e = \frac{\rho U_0 L_0}{\eta} \quad , \tag{2.47}$$

which is the *Reynolds number*. We use the parameters, U_0 , L_0 , T_0 and P_0 to scale all the quantities in the Navier-Stokes equation and get: $\tilde{\mathbf{r}} = \mathbf{r}/L_0$, $\tilde{\boldsymbol{\upsilon}} = \boldsymbol{\upsilon}/U_0$, $\tilde{\nabla} = L_0\nabla$, and $\tilde{p} = pL_0/\eta U_0 = p/P_0$. Inserting them in the Eq. (2.44) and excluding the body forces, we reach to

$$\rho\Big[\frac{U_0}{T_0}\tilde{\partial}_t\tilde{\boldsymbol{\upsilon}} + \frac{U_0^2}{L_0}(\tilde{\boldsymbol{\upsilon}}\cdot\tilde{\nabla})\tilde{\boldsymbol{\upsilon}}\Big] = -\frac{P_0}{L_0}\tilde{\nabla}\tilde{p} + \frac{\eta U_0}{L_0^2}\tilde{\nabla}^2\tilde{\boldsymbol{\upsilon}} \quad . \tag{2.48}$$

By multiplying the expression by $\frac{L_0^2}{U_0\eta}$, we obtain

$$R_e\Big[\tilde{\partial}_t\tilde{\boldsymbol{\upsilon}} + (\tilde{\boldsymbol{\upsilon}}\cdot\tilde{\nabla})\tilde{\boldsymbol{\upsilon}}\Big] = -\tilde{\nabla}\tilde{p} + \tilde{\nabla}^2\tilde{\boldsymbol{\upsilon}} \quad . \tag{2.49}$$

We see for low Reynolds number, $R_e \ll 1$ the viscous term $\tilde{\nabla}^2\tilde{\boldsymbol{\upsilon}}$ dominates, whereas in steady state for $R_e \gg 1$, the inercia term $(\tilde{\boldsymbol{\upsilon}}\cdot\tilde{\nabla})\tilde{\boldsymbol{\upsilon}}$ dominates.

In the limit of low Reynolds number, the non-linear Stokes equation is reduced to the linear Stokes equation,

$$0 = -\boldsymbol{\nabla}p + \eta\nabla^2\boldsymbol{\upsilon} \quad , \tag{2.50}$$

in which is possible to find analytical solutions.

Similarly, the corresponding dimensionless incompresibility condition $\partial_i\upsilon_i = 0$, since $\partial_i = (1/L_0)\tilde{\partial}_i$ and $\upsilon_i = V_0\tilde{\upsilon}_i$ is just,

$$\tilde{\partial}\tilde{\upsilon}_i = 0 \quad . \tag{2.51}$$

On the other hand it is interesting how some terms in the Navier-Stokes equation can be neglected under controlled parameters. Say the oscillation period, where the intrinsic

[2]Also named *creeping flow*. It is a kind of fluid where typically the fluid velocities are very slow, the viscosities are very large, or the length-scales of the flow are very small.

time scale $T_0 = L_0/V_0$ makes the non-linear term comparable $\boldsymbol{v} \cdot \boldsymbol{\nabla}\boldsymbol{v}$ smaller[3] to the time derivative of the velocity,

$$\rho \partial_t \boldsymbol{v} = -\boldsymbol{\nabla} p + \eta \nabla^2 \boldsymbol{v} \qquad . \tag{2.52}$$

In the regime of incompressible fluids, let us define the vorticity,

$$\boldsymbol{\omega} = \boldsymbol{\nabla} \times \boldsymbol{v} \qquad , \tag{2.53}$$

and taking the rotational of the Stokes equation, Eq (2.44),

$$\partial_t \boldsymbol{\omega} = \frac{\eta}{\rho} \nabla^2 \boldsymbol{\omega} \qquad , \tag{2.54}$$

which is a tractable equation. In the same way, applying a divergence to such Stokes equation, and using $\boldsymbol{\nabla} \cdot \boldsymbol{v} = 0$, we obtain

$$\nabla^2 p = 0 \qquad , \tag{2.55}$$

this is a Laplace equation for pressure. The latter two equations shows the feasiblity in finding analytical solutions to the creeping flow problem.

For a more general approach see the Appendix A.1

[3] in case it occurs small oscillations where $\boldsymbol{v} \cdot \boldsymbol{\nabla}\boldsymbol{v} \sim U_0^2/L$ and the derivative $\partial_t \boldsymbol{v}$ is of the order of U_0^2/a where a is the amplitude of the oscillations.

3. Basic flow solutions

From the flow governing equations, the non-linearity of the Navier-Stokes increases the complexity of finding analytical solutions. In this chapter, we shall find them in a very few important cases. In all cases, the solution must respect boundary conditions of both Dirichlet and Newman type:

$$v_i(\mathbf{r},\, t) = a(\mathbf{r}) \quad , \text{for } \mathbf{r} \in \partial\Omega, \quad \text{(Dirichlet boundary condition)}, \tag{3.1}$$

$$(\mathbf{n} \cdot \boldsymbol{\nabla}) v_i(\mathbf{r},\, t) = b(\mathbf{r}) \quad , \text{for } \mathbf{r} \in \partial\Omega, \quad \text{(Newman boundary condition)}, \tag{3.2}$$

where $\mathbf{n}$ is the outward-pointing vector normal to the surface. In this chapter, consider we have *no-slip* boundary condition for the velocity field, that is

$$\boldsymbol{v}(\mathbf{r}) = \boldsymbol{v}_{\text{wall}} \quad , \text{for } \mathbf{r} \in \partial\Omega, \quad \text{(no-slip)}. \tag{3.3}$$

The microscopic explanation for this is to think in having a momentum relaxation between the molecules of the wall, which are at rest, and that of the fluid. At the molecular scales of the fluid, which for highly dense liquids is about 0.3 nm, this lenght is comparable to the intermolecular distance of the solid. For rarified gases, for which the mean free path is comparable to the channels dimensions, this assumption no longer holds.

3.1. Fluids in Mechanical Equilibrium

A fluid in mechanical equilibrium, with thermodynamic properties varying according to the themodynamic laws, must be at rest with respect to the walls and the velocity $\boldsymbol{v}(\mathbf{r}) = 0$ everywhere , otherwise there would be heat loss due to internal friction in the fluid. In other words, loss kinetic energy by heat conversion due to internal friction. The mathematical description for this problem is,

$$\boldsymbol{v}(\mathbf{r}) = \mathbf{0} \quad , \tag{3.4}$$

$$\mathbf{0} = -\boldsymbol{\nabla} p - \rho g \mathbf{e}_z \quad , \tag{3.5}$$

where we considered the gravitational effect. Solving this equation for an incompressible fluid,

$$p(z) = p^* - \rho g z \quad , \tag{3.6}$$

where p^* is determined by the boundary condition at a known level. Here we use $z = 0$. The z-dependent term is denoted as the *hydrostatic pressure*, which in microfluidics is the unique manifestation of gravity,

$$p_{\mathrm{hs}}(z) = -\rho g z \quad . \tag{3.7}$$

By rewriting the solution, Eq. (3.6) we arrive at

$$p_{\mathrm{tot}} = p + p_{\mathrm{hs}}(z) \quad , \tag{3.8}$$

where p is the auxiliary pressure, which will be used in the course of this work. Note that the resulting Navier-Stokes equation thus contains only this p because the gravitational body force cancels the gradient of the hydrostatic pressure. In the case of a compressible ideal fluid under isothermal conditions,

$$\rho = \frac{\rho^*}{p^*} p \quad , \tag{3.9}$$

where for one particular state of a gas, ρ^* and p^* is the density and the pressure, respectively. Therefore, the mathematical description is completely determined by the recalled Eqs. (3.4) and (3.5),

$$\boldsymbol{v}(\mathbf{r}) = \mathbf{0} \quad , \tag{3.10}$$

$$\mathbf{0} = -\boldsymbol{\nabla} p - \frac{\rho^*}{p^*} p g \mathbf{e}_z \quad , \tag{3.11}$$

whose solution by simply integration is,

$$p(z) = p^* \exp\Big(- \frac{\rho^* g}{p^*} z \Big) \quad . \tag{3.12}$$

3.2. Couette flow

This flow problem consists in a fluid contained between two infinite parallel plates, where one is moving with respect to the other. This setup is widely known in rheology since it allows a reasonable estimate of the viscosity η. In particular, a commom flow arrangement configuration consists in a fluid moving between two axysymmetric concentric cylinders.

Let us analize a simple case as shown in the Fig. 3.1 where a liquid is placed between two parallel plates, oriented horizontally, perpendicular to the gravitational acceleration $\mathbf{g}$. Take into account that the top plate, at $z = h$, is moving with constant velocity v_0 and the bottom plate, $z = 0$, is maintained fixed with respect to the bottom plate.

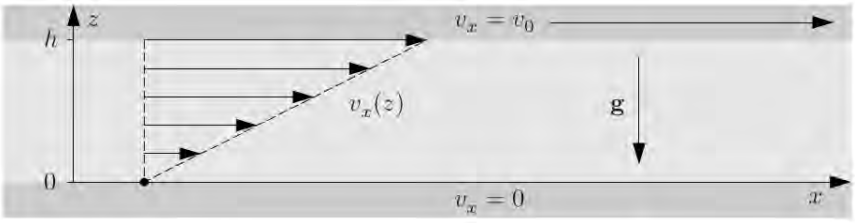

Figure 3.1.: A Couette flow consists in a fluid between two horizontally, placed and parallel plates where one of them is moving with respect to other with constant speed. Note that it is considering no-slip conditions at the boundaries.

As in the previous example, there is a translation invariance along the x-y plane and therefore the velocity field depends only on z. Moreover, since the driving force points in the x direction, only the x component of the velocity is non-zero,

$$\boldsymbol{v}(\mathbf{r}) = v_x(z)\mathbf{e}_x \quad . \tag{3.13}$$

In analogy with the previous case, an immediate consequence of Eq. (3.13) is that the non-linear term $(\boldsymbol{v} \cdot \boldsymbol{\nabla})\boldsymbol{v}$, is null. It follows the Navier-Stokes equation simply is,

$$\eta \partial_z^2 v_x(z) = 0 \quad , \tag{3.14}$$

with the boundary conditions,

$$v(0) = 0 \quad , \text{(no-slip)} \tag{3.15}$$

$$v(h) = v_0 \quad , \text{(no-slip)} \tag{3.16}$$

and thus,

$$v_x(z) = v_0 \frac{z}{h} \quad . \tag{3.17}$$

By applying this result for a long but finite plate with area $\mathcal{A}$ and using the viscous stress tensor σ', Eq. (2.45), it is possible to determine the external force needed to drag the plane with fixed speed v_0,

$$F_x = \sigma'_{xz}\mathcal{A} = \eta\frac{v_0\mathcal{A}}{h} \quad . \tag{3.18}$$

This result is useful to determine the viscosity η. One interesting feature of working in microfluidics is that the surface and viscous forces become dominant, while the inertial and buoyancy forces become negligible. This characteristic makes it possible to measure the viscosity using microfluidic devices.

3.3. Poiseuille flow

We analyze another class of analytical solutions for the Navier-Stokes equation. In a Poiseuille flow, the fluid flows through an arbitrary cross sectional shape, over a long, straight, and rigid channel by applying a pressure difference between the ends of the channels. Hagen and Poiseuille were the firsts whose studied channels with circular cross sectional shape. In microfluidics, depending on the fabrication technique one can obtain other shapes such as elliptical, rectangular, etc. The Fig. 3.2 shows a gaussian like cross-section.

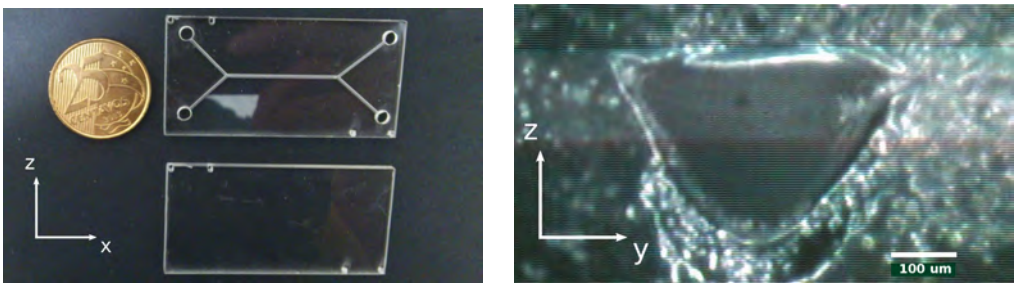

Figure 3.2.: On the left, fabrication of microchannels by laser heating printing. On the right, when selling the channels, the cross section shows a gaussian like form. The device was performed in collaboration with the Instituto de Química - USP at the Departamento de Química Fundamental under the coordination of Prof. Lúcio Angnes.

3.3.1. Arbitrary cross-sectional shape

Let us first study the Poiseuille-flow along the x-direction as shown in Fig. 3.3. A flow is driven through a cross-section under the effect of a pressure difference Δp along a segment of length L. In $p(0) = p^* + \Delta p$ with $p(L) = p^*$, where p is the auxiliary pressure mentioned in Eq. (3.8) without gravitational effects.

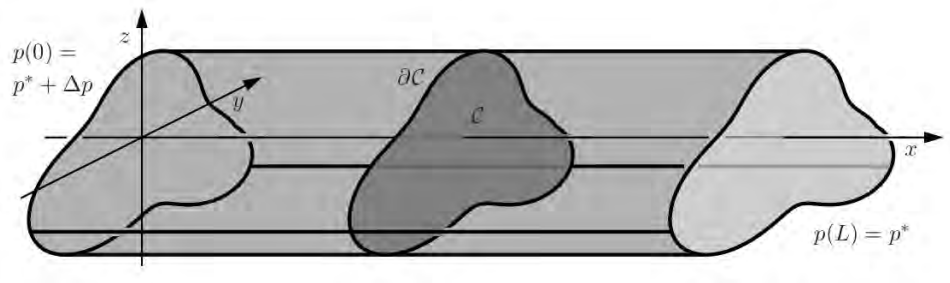

Figure 3.3.: A channel with a shaped cross-section $\mathcal{C}$ in the yz-plane. This Poiseuille-flow problem is translational invariant in the x direction. The boundary of $\mathcal{C}$ is denoted by $\partial\mathcal{C}$. Note the difference of pressure $\triangle p$ between the two ends.

By combining the translational invariance in the x direction and the lack of forces in the yz plane we deduce that the velocity field has the structure, $\boldsymbol{\upsilon}(\mathbf{r}) = \upsilon_x(y,z)\mathbf{e}_x$[1]. Therefore, with $(\boldsymbol{\upsilon}\cdot\boldsymbol{\nabla})\boldsymbol{\upsilon} = 0$ and considering the steady-state regime, the Navier-Stokes equation becomes,

$$\boldsymbol{\upsilon}(\mathbf{r}) = \upsilon_x(y,z)\mathbf{e}_x \quad , \tag{3.19}$$

$$-\boldsymbol{\nabla}p + \eta\nabla^2\Big(\upsilon_x(y,z)\mathbf{e}_x\Big) = 0 \quad , \tag{3.20}$$

it immediately follows that $\partial_y p = 0$ and $\partial_z p = 0$, meaning the pressure field depends only on x, $p(\mathbf{r}) = p(x)$. Consequently the Navier-Stokes equation is reduced to:

$$\eta\Big(\partial_y^2 + \partial_z^2\Big)\upsilon_x(y,z) = \partial_x p(x) \quad , \tag{3.21}$$

where we have a yz dependence on the left hand side and a x dependence on the right one, leading to the same constant for the solution of the Navier-Stokes equation.

A constant pressure gradient $\partial_x p(x)$ means that the pressure must be a linear funciton of x. Using the boundary conditions we obtain,

$$p(\mathbf{r}) = \frac{\triangle p}{L}(L-x) + p^* \quad , \tag{3.22}$$

from which we retrieve the second-order partial differential equation in the domain $\mathcal{C}$ with no-slip boundary conditions at $\partial\mathcal{C}$,

$$\Big(\partial_y^2 + \partial_z^2\Big)\upsilon_x(y,z) = -\frac{\triangle p}{\eta L} \quad \text{for} \quad (y,z)\in\mathcal{C} \quad , \tag{3.23}$$

[1]The translational invariance is only valid at low speeds. As the velocity increases the symmetry is broken.

$$\upsilon_x(y,z) = 0 \quad \text{for} \quad (y,z) \in \partial\mathcal{C} \quad . \tag{3.24}$$

In microfluidics it is customary to calculate the volumetric flow rate Q defined as:

$$Q \equiv \int_{\mathcal{C}} \mathrm{d}y\mathrm{d}z\upsilon_x(y,z) \quad , \tag{3.25}$$

In the Appendix we show an interesting approach based in the eigenfunction expansion to calculate the velocity $\upsilon_x(y,z)$ by solving the Poisson type Eq. (3.23) in the Dirac notation,

$$|\upsilon_x\rangle = \frac{\triangle p}{\eta L}\sum_{n=1}^{\infty}\frac{\langle\phi_n|1\rangle}{\kappa_n^2}|\phi_n\rangle \quad . \tag{3.26}$$

Therefore the flow rate in Eq. (3.25) becomes

$$Q = \int_{\mathcal{C}} \mathrm{d}y\mathrm{d}z1\upsilon_x(y,z) = \langle 1|\upsilon_x\rangle = \frac{\triangle p}{\eta L}\sum_{n=1}^{\infty}\frac{1}{\kappa_n^2}\langle\phi_n|1\rangle\langle 1|\phi_n\rangle \quad , \tag{3.27}$$

3.3.1.1. Case: Infinite parallel-plate channel

In microfluidics, it is customary to have geometries as shown in Fig. 3.4, with large aspect ratio. We observe a scheme similar to the Couette flow but with fixed plates instead.

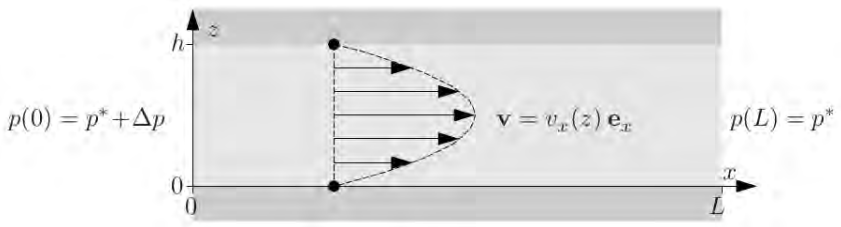

Figure 3.4.: A fluid moving in the x direction under a pressure difference. We consider the apect ratio so large that we can imagine the channel as an infinite parallel-plate channel

At the microscope scale the aspect ratio is so large that we can approximate it to an infinite parallel-plate configuration. Given the symmetry in the y direction, we reach

$$\partial_z^2\upsilon_x(z) = -\frac{\triangle p}{\eta L} \quad , \tag{3.28}$$

with the boundary conditions,

$$\upsilon_x(0) = 0 \quad \text{(no-slip)} \quad , \tag{3.29}$$

$$v_x(h) = 0 \quad \text{(no-slip)} \quad . \tag{3.30}$$

By taking into account the first derivative $\partial_z v_x = 0$ at $z = z_0$ we obtain, as a result, the simple parabola

$$v_x(z) = \frac{\triangle p}{2\eta L}(h - z)z \quad , \tag{3.31}$$

therefore, the flow rate Q through a section of width ω is calculated to be

$$Q = \int_0^{\omega} \mathrm{d}y \int_0^{h} \mathrm{d}z \frac{\triangle p}{2\eta L}(h - z)z = \frac{h^3 \omega}{12\eta L}\triangle p \quad . \tag{3.32}$$

For an aspect ratio $h = \omega/3$, the flow rate has an error of 23%, and falls to 7% for an aspect ratio of $h = \omega/10$.

In the following particular cases we propose trial functions according to the geometry of the cross-section of the form $v = v_0 \times \partial\mathcal{C}$ with centers at the origin $(y, z) = (0, 0)$ as is shown in the Fig. 3.5.

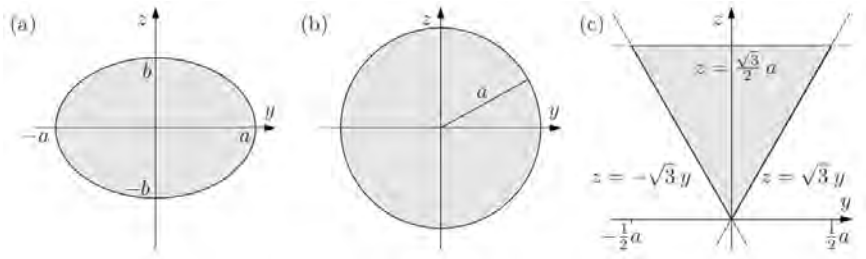

Figure 3.5.: Particular cross section cases for the Poiseuille flow problem. An ellipse (a) with semi-axis a and b, a circle (b) with radius a and an equilateral triangle (c) with side lenght a.

The elliptic, circular and triangula cross-sections lead to interesting results, which are analyzed in detail in the Appendix.

3.3.1.2. Case: rectangular cross-section

For lab-on-a-chip systems we have usually rectangular cross sections, which are widely present in this thesis, micro-devices fabricated by soft lithography, with replica molding technique using the epoxy-based polymer SU-8 we see in the successive last chapters.

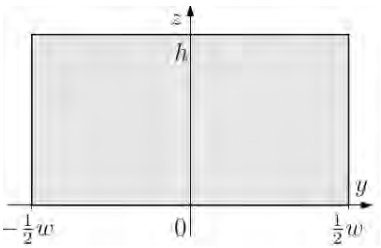

Figure 3.6.: A common reactangular cross section of height h and width w

Surprisingly there is no analytical solution for the Poiseuille-flow problem, the best we can do is to find a Fourier sum approximation. Considering the dimensions in Fig. 3.6, always $h < w$, and the symmetry we discussed in the previous cases, the Navier-Stokes equation and the associated boundary conditions are

$$\left(\partial_y^2 + \partial_z^2\right) v_x(y,z) = -\frac{\triangle p}{\eta L} \qquad \text{for} \quad -\frac{1}{2}w < y < \frac{1}{2}w\,, \quad 0 < z < h \quad , \tag{3.33}$$

$$v_x(y,z) = 0 \qquad \text{for} \quad y = -\frac{1}{2}w \quad , z = 0 \quad , z = h \quad . \tag{3.34}$$

To solve the corresponding Navier-Stokes equation (3.33) , let us use the Fourier series analysis.

Theorem. For a 2π-periodic function $F(x)$ integrable in the interval $[-\pi, \pi]$,

$$F(x) = a_0 + \sum_{k=1}^{n} \left(a_k \sin kx + b_k \cos kx\right) \quad , \tag{3.35}$$

we have

$$\begin{cases} a_0 = \frac{1}{2\pi}\int_{-\pi}^{\pi} & F(x)\mathrm{d}x \\ a_k = \frac{1}{\pi}\int_{-\pi}^{\pi} & F(x)\sin kx\mathrm{d}x \quad \text{, for} \quad 1 \le k \le n \\ b_k = \frac{1}{\pi}\int_{-\pi}^{\pi} & F(x)\cos kx\mathrm{d}x \quad \text{for} \quad 1 \le k \le n \end{cases} . \tag{3.36}$$

The Equation 3.35 is a function represented as a Fourier series.

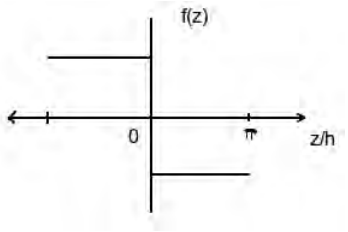

Figure 3.7.: We can expand a constant function as a square wave in the interval we are interested

In our Eq., (3.33), let us express the constant $-\triangle p/\eta L$ in a Fourier series according to the periodic function we have represented in Fig. 3.7 by using the former theorem,

$$-\frac{\triangle p}{\eta L} = -\frac{\triangle p}{\eta L}\frac{4}{\pi}\sum_{n,\,\mathrm{odd}}^{\infty}\frac{1}{n}\sin\left(n\pi\frac{z}{h}\right) \quad . \tag{3.37}$$

It must be noted we are using the change of variables $z \to \pi z/h$ and then finding the constants with the integration in the interval $[-h,\, h]$.

For a complete determination of the velocity let us express it by a Fourier series where the coefficients are y and z dependent, precisely the z ones in the form of the constant. See Eq. (3.37). That is

$$\upsilon_x(y,z) \equiv \sum_{n=1}^{\infty} f_n(y)\sin\left(n\pi\frac{z}{h}\right) \quad . \tag{3.38}$$

which replacing in the Navier-Stokes equation leads to,

$$\left(\partial_y^2+\partial_z^2\right)\upsilon_x(y,z) = \sum_{n=1}^{\infty}\left[f_n''(y)-\frac{n^2\pi^2}{h^2}f_n(y)\right]\sin\left(n\pi\frac{z}{h}\right) \quad . \tag{3.39}$$

Comparing this equation with the expansion in Eq. (3.37), they originates the next solutions:

$$\begin{cases} f_n(y) = 0 & , \text{for } n\, even, \\ f_n''(y) - \frac{n^2\pi^2}{h^2}f_n(y) = -\frac{\triangle p}{\eta L}\frac{4}{\pi}\frac{1}{n} & , \text{for } n\, odd. \end{cases} \quad , \tag{3.40}$$

which the second one is a inhomogeneous second-order differential equation. A general solution is the sum of solutions for homogeneous and a particular solution for a inhomogeneous equations.

$$\begin{cases} f_n^{\mathrm{hom}}(y) = A\cosh\left(\frac{n\pi}{h}y\right) + B\sinh\left(\frac{n\pi}{h}y\right) & , \text{for } n\, odd \\ f_n^{\mathrm{inhom}}(y) = \frac{4h^2\triangle p}{\pi^3\eta L}\frac{1}{n^3} & , \text{for } n\, odd \end{cases} \quad , \tag{3.41}$$

and by including the boundaring conditions $f_n(\pm\frac{w}{2}) = 0$ we arrive to the system of equations,

$$\begin{cases} \frac{4h^2\triangle p}{\pi^3\eta L}\frac{1}{n^3} + A\cosh\left(\frac{n\pi}{h}\frac{w}{2}\right) + B\sinh\left(\frac{n\pi}{h}\frac{w}{2}\right) = 0 \\ \frac{4h^2\triangle p}{\pi^3\eta L}\frac{1}{n^3} + A\cosh\left(\frac{n\pi}{h}\frac{w}{2}\right) - B\sinh\left(\frac{n\pi}{h}\frac{w}{2}\right) = 0 \end{cases} \quad , \tag{3.42}$$

from where we obtain

$$f_n(y) = \frac{4h^2\triangle p}{\pi^3\eta L}\frac{1}{n^3}\left(1 - \frac{\cosh(n\pi\frac{y}{h})}{\cosh(n\pi\frac{w}{2h})}\right) \quad , \text{for } n \text{ odd}, \tag{3.43}$$

and finally the velocity for the Poiseuille flow in the rectangular channel is expressed as

$$v_x(y,z) \equiv \frac{4h^2\triangle p}{\pi^3\eta L}\sum_{n,\,\text{odd}}^{\infty}\frac{1}{n^3}\left[1 - \frac{\cosh(n\pi\frac{y}{h})}{\cosh(n\pi\frac{w}{2h})}\right]\sin\left(n\pi\frac{z}{h}\right) \quad . \tag{3.44}$$

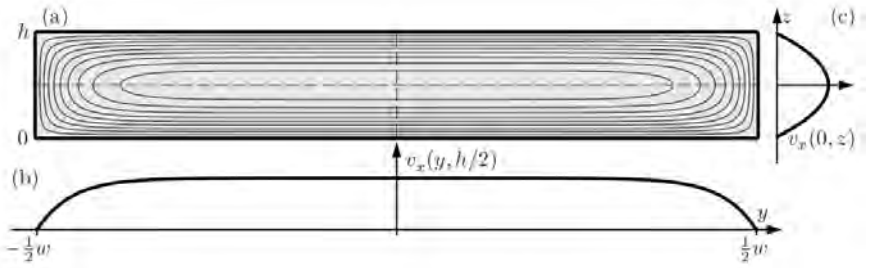

Figure 3.8.: Profile for the velocity solution along the symmetry axis.

In Fig. 3.8 is shown a plot of the contour field lines of the velocity solution.

By using the solution Fig. 3.8 we can calculate the flow rate Q by simple integration evaluation,

$$Q = \int_{-\frac{w}{2}}^{\frac{w}{2}} \mathrm{d}y \int_0^h \mathrm{d}z v_x(y,z) \quad , \tag{3.45}$$

$$Q = \frac{4h^2\triangle p}{\pi^3\eta L}\int_{-\frac{w}{2}}^{\frac{w}{2}} \mathrm{d}y \int_0^h \mathrm{d}z \sum_{n,\,\text{odd}}^{\infty}\frac{1}{n^3}\left[1 - \frac{\cosh(n\pi\frac{y}{h})}{\cosh(n\pi\frac{w}{2h})}\right]\sin\left(n\pi\frac{z}{h}\right) \quad , \tag{3.46}$$

$$Q = \frac{4h^2\triangle p}{\pi^3\eta L}\sum_{n,\,\text{odd}}^{\infty}\frac{1}{n^3}\frac{2h}{n\pi}\left[w - \frac{2h}{n\pi}\tanh\left(n\pi\frac{w}{2h}\right)\right] \quad , \tag{3.47}$$

and by the use of $\sum_{n,\,\mathrm{odd}}^{\infty} \frac{1}{n^4} = \frac{\pi^4}{96}$,

$$Q = \frac{h^3 w \triangle p}{12\eta L}\Big[1 - \sum_{n,\,\mathrm{odd}}^{\infty} \frac{1}{n^5}\frac{192}{\pi^5}\frac{h}{w}\tanh\Big(n\pi\frac{w}{2h}\Big)\Big] \quad . \tag{3.48}$$

It is even possible to reduce this expression by doing the approximation in the limit $\frac{h}{w} \to 0$, that is $\frac{h}{w}\tanh\Big(n\pi\frac{w}{2h}\Big) \to \frac{h}{w}$. Hence

$$Q = \frac{h^3 w \triangle p}{12\eta L}\Big[1 - \frac{192}{\pi^5}\frac{h}{w}\sum_{n,\,\mathrm{odd}}^{\infty} \frac{1}{n^5}\Big] \quad . \tag{3.49}$$

Utilizing the Riemann zeta function notation, $\zeta(x) \equiv \sum_{n=1}^{\infty} \frac{1}{n^x}$, and

$$\sum_{n,\,\mathrm{odd}}^{\infty} \frac{1}{n^5} = \sum_{n=1}^{\infty} \frac{1}{n^5} - \sum_{n,\,\mathrm{even}}^{\infty} \frac{1}{n^5} = \zeta(5) - \sum_{k=1}^{\infty} \frac{1}{(2k)^5} = \frac{31}{32}\zeta(5) \quad . \tag{3.50}$$

Therefore, Q is simply

$$Q = \frac{h^3 w \triangle p}{12\eta L}\Big[1 - \frac{192}{\pi^5}\frac{31}{32}\zeta(5)\frac{h}{w}\Big] \quad , \tag{3.51}$$

$$Q \approx \frac{h^3 w \triangle p}{12\eta L}\Big[1 - 0.63\frac{h}{w}\Big] \qquad , \text{ for } h < w \; . \tag{3.52}$$

For the square case, with $h = w$, the error is 13% while for the ratio $h = w/2$, the error is approximately 0.2%. Compare this flow rate Q with the result obtained for the infinitely parallel-plate channel. See Eq. 3.32.

4. Fabrication of Microsystems using Soft Lithography

4.1. Overview

In this chapter we will focus in the microfabrication of our structures. We specify how the processs is done, which methods are known or common for a determined purpose, which polymeric materials are suitable for microchannels, etc. The Fig. 4.1 shows the structure of this dissertation and the course of the next chapters.

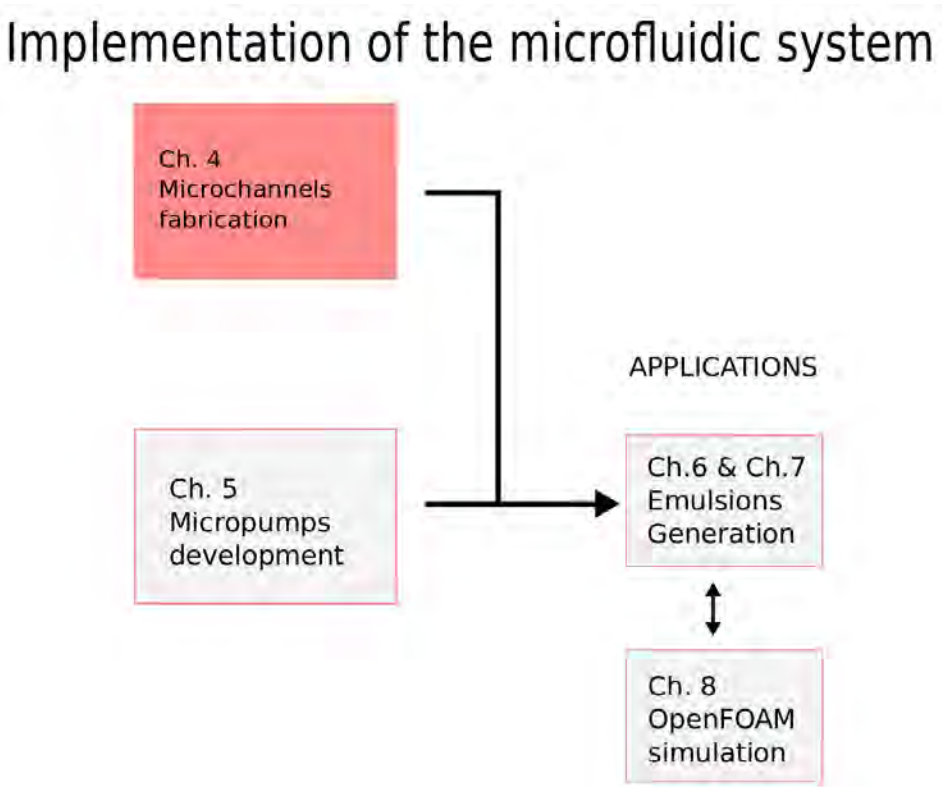

Figure 4.1.: Structure of the implementation of the microfludic system and the emulsion generation application. This chapter we focus in the fabrication of the microsystems.

Soft lithography is a family of techniques for printing, molding and embossing with an elastic polymeric (elastomer) stamp. It permits a variety of forms, tolerates a wide variety of materials and generates 3D structures for microscale well-defined surface chemistries. It has emerged as a technology with innumerable set of applications, for instance: microfluidics [1], development of microsystems as lab-on-a-chip systems [24, 25], applications in cell biology [26],

microelectromechanical and flexible electronics/photonics systems [27], among others. Commonly techniques include [28]: (i) microcontact printing (μCP) of alkanethiols and proteins on gold-coated and glass substrates; (ii) replica molding (REM) for fabrication of microfluidic devices in poly(dimethyl siloxane), and of nanostructures in polyurethane or epoxy; (iii) solvent-assisted micromolding (SAMIM) of nanostructures in poly(methyl methacrylate); among others. In this work we focus in the replica molding (REM) approach.

4.2. Introduction

Soft lithography was originated from photolithography, which is a process used in microfabrication to transfer patterns to a light-sensitive chemical "photoresist". Photolithography was initially applied for fabrication of DNA arrays in the late 1980s [29]. Despite of these great contributions in the beginning, photolithography has a number of limitations related to biological systems, such as the implementation of a clean room, making difficult for most of biologists, chemists and related community. Another difficulty is the absence of control over surface chemistry for fluids as including pattern wetting phenomena, as well as limiting a set of materials. In contrast, soft lithography does not have the limitations described above, making possible to produce planar, curved and flexible devices, low-cost and rapid prototyping.

REM

This technique employs poly(dimethyl siloxane) (PDMS) [30] for the fabrication of microfluidic devices, and has the potential to discuss the clinical research areas in which they have made the greatest impact [28, 31]. This polymeric material offers a rich number of features [32, 33]: (i) physically, it has a shear modulus of 0.25 MPa and Young's modulus of roughly 0.5 MPa, charasteristic of a moderately stiff elastomer, important at the atomic level for sealing formation of the microfluidic system; (ii) It is optically transparent down to 300 nm; (iii) chemically, it is with some degree hydrophobic, with water contact angle $\sim 110^{o}$, but its surface can be modified under exposure to an oxygen plasma to become hydrophilic, this is with water contac angle $\sim 10^{o}$; and (iv) economically for a lab, it is available at acceptable prices $\sim$US$ 200/Kg. Soft lithography also provides a set of interesting tools for nanofabrication, as for instance, structures of 3 cm^2 in area with 100 nm features.

At the current stage of development, soft lithography depends basically on the use of the method to generate the master mold. Once the master is generated, most of the fabrication tasks can be continued for replicating and printing procedures.

During the microfabrication there are crucial stages that must be regardered. (i) When ordering the photomask, the ambiance conditions influence directly over the dimensions of the photomask. We must be sure that the humidity conditions are within the relative humidity range we will describe later. (ii) The fabrication of the master mold is altered considerably along: the variation in acceleration of the single plate rotator during the spinning, the required width of the thin film formed according to the viscosity of the SU8 polymer, the time-light exposition within the photoaligner, etc. Paying attention to every of these steps the success a well done master mold. (iii) The elastomeric stamp has two important aspects:

no bubbles inside it, and the chemical treatment of the surface by the plasma oxygen exposition for selling the channel. In case of using glasses, make the corresponding treatment of them.

Experimental Design

The Figure 4.1 shows the four major steps used for soft lithography prototyping: (i) pattern design; (ii) fabrication of the mask and the master mold; (iii) fabrication of the PDMS stamp; and (iv) fabrication of micro- and nanostructures with the stamp by printing, molding and embossing. The term soft lithography is sometimes referred to as "rapid prototyping" [34].

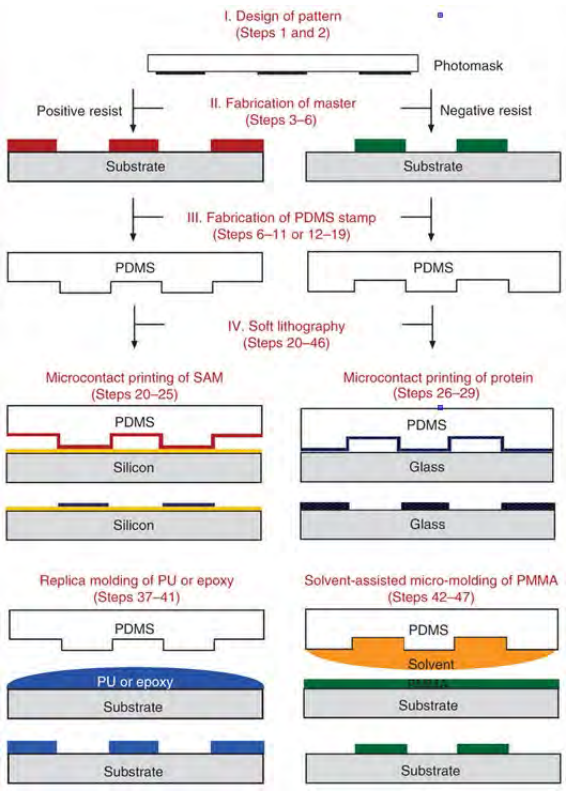

Figure 4.2.: Four major steps involving in soft lithography and three major soft lithography techniques.

Design of pattern

A number of computer-aided design (CAD) softwares are available to design a pattern. There are vector-based drawing softwares as CorelDRAW, Sketchup, Inkscape, among others with high advanced tools and more capabilities. This is the case of Autodesk AutoCAD, see Fig. 4.3, which permits us to get a higher precision and higher drawing speed. The mask design is a crucial part and plays an important role in master template formation for microchannel fabrication. This photomask is a quartz, or fused silica plate, plastic or glass depending of the resolution, and patterned with opaque chrome on its surface [35].

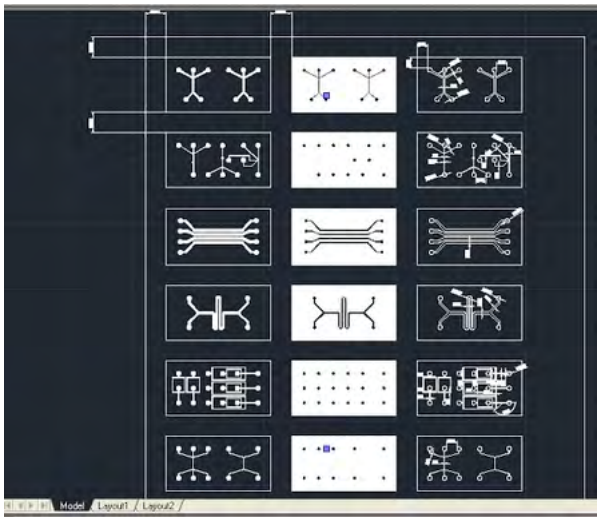

Figure 4.3.: First prototypes designed in Autodesk AutoCAD. The dimensions involved are about tens of micrometers.

Fabrication of mask

Currently most of commercial chrome photomask suppliers use the AutoCAD DXF (Drawing Interchange Format, or Drawing Exchange Format) format for printing. The physical properties of the photomask can be altered by the ambient conditions. Basically, four major factors which can affect the mask dimensions [35], critical for microscale applications.

Temperature influence

As the most materials, they expand with temperature. Film and glass photolithographic masks are not the exceptions. This expansion or contracitons is determined by the thermal expansion coefficient $\alpha(T)$, expressed in mm/°C. Critical temperatures of less than -20°C and bigger than 60°C will damage the film. An optimal temperature is around room temperature, 21°C.

Humidity influence

This is the hardest of the four factors to control adequately, because of the inhomogeneity of humidity distribution in the media environment, which causes variations from area to area and corner to corner. The expansion is determined by the relative humidity expansion coefficient γ_E, expressed in μm/m per unit percentage, %, of change in relative humidity (% RH). For instance, when $\gamma_E = 1$, means that one metre of that material will expand $1\,\mu$m when the humidity increase by 1 %. Similarly when the material shrinks. Typical photomasks are made of polyester which absorbs water and thus expand with incerasing relative humidity. Changes in temperature and humidity at the range of 70 % will cause irreversible changes.

Influence of mechanical tension

The expansion is determined by the elasticity modulus. Photolithographic materials masks suffer mechanical tension variations when it is exposed to vacuum. It is important to reach the vacuum gently at certains controllable conditions of temperature and humidity to be sure it is working under the limits to avoid dimensional changes.

Influence of aging

It is critical for some photolithographic materials as silver halides masks, which are chemical compounds of silver and one of the halogens. There is a tendency to change back to the initial size in several months.

We used a polyester film whose thicknes is 0.18 mm. Our commercial supplier/provider works with a high-resolution commercial printer, with 8,000 d.p.i, a positioning tolerance of ± 0.0127 mm at 20 °C and 60/70 RH, using a MANIA BARCO Crescent 40 photoplotter, see Fig. 4.4. The photomask is a green-blue-light sensitive film, specially designed for ultra-short exposure times, in microseconds, in photoplotters with green laser diodes (500 - 553 nm) or blue argon lasers (488 nm).

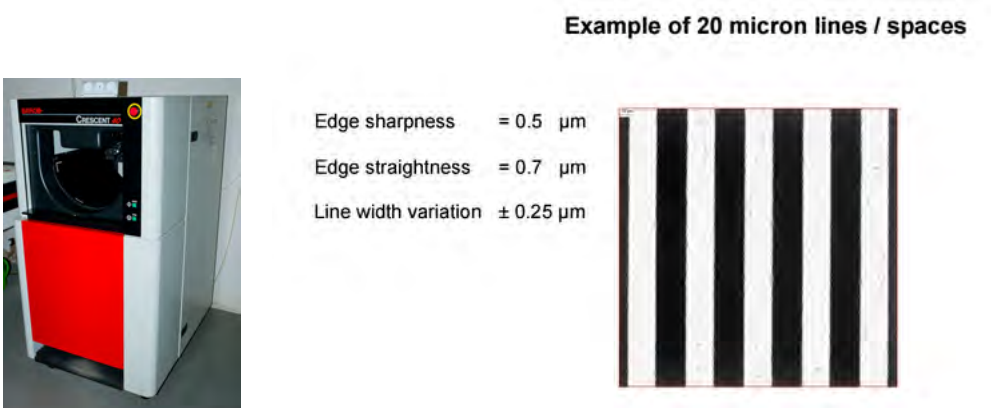

Figure 4.4.: Photoplotter MANIA BARCO Crescent 40 and Sample of micrometer lines resolution.

Fabrication of the master mold

This is the most sensitive part of the whole process. It needs to be done in a careful way following the protocol without flexibility. It is composed by two parts; i) the generation of the micrometric film using a polymeric precursor $SU-8$ and; ii) the exposure to ultraviolet (UV) light for the polymerization initiation. This is shown in more detail in Fig. 4.5.

Fabrication of elastomeric stamp

The key element of soft lithography is obtaining the elastomeric stamp with patterned structures on its surface. Its mechanical properties are critical for transfering a pattern with high fidelity. Generally, any elastomer can be used to form a negative stamp, however most

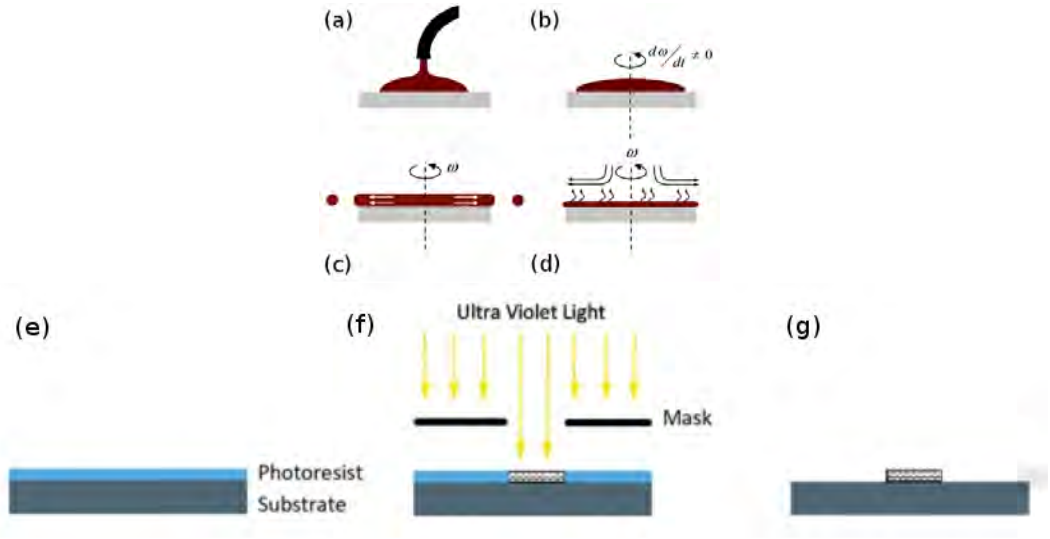

Figure 4.5.: Above; (a) spreading the $SU-8$ polymer over the spinning rotator; (b) This accelerates until reaches a constancy (c) in terms of revolutions per minute (RPM), around a few thousands of RPM. (d) During the spinning the sample is heating for a few seconds to achieve a partial polymerization and fixed firmly on the hot plate; (e) once the photoresist film is generated, (f) it is covered by the UV-sensitive chrome mask and both of them exposed to UV light. (g) The sample is washed by a solvent and remained only the exposed areas to UV light for the next steps of polymerization.

researches has focused on the silicone-based rubber or cross-linked polydimethylsiloxane (PDMS). Specifically, we work with Sylgard 184 from Dow Corning. This is the most commonly used for fabrication of stamps with feature sizes larger than 500 nm [36]. The Fig. 4.6 shows the normal procedure for PDMS embossing. This figure also shows the use of "hard" PDMS (h-PDMS) which is based on vinyl and hydrosilane end-linked polymers with a higher modulus, around $9\,\mathrm{N/mm^2}$, than that of Sylgard 184 PDMS, near to $2\,\mathrm{N/mm^2}$.

REM or embossing of structure in a polymer

According to the schematic Fig. 4.2, REM consists of three major steps, [37]: (i) creating the master mold reliefs; (ii) transfering the pattern into PDMS by REM; and (iii) chemical treatment of the surface of the samples by joining each other. In our work we used frequently the oxygen plasma treatment for surface modification. See Fig. 4.7.

4.3. Materials and Methods

The Laboratory of Microfabricaton [38] (LMF) of the Centro Nacional de Pesquisa em Energia e Materiais (CNPEM), located in Campinas-SP, Brasil, has provided us all the necessary staff and equipment, most of materials and the suitable training in its clean room along the development of this project.

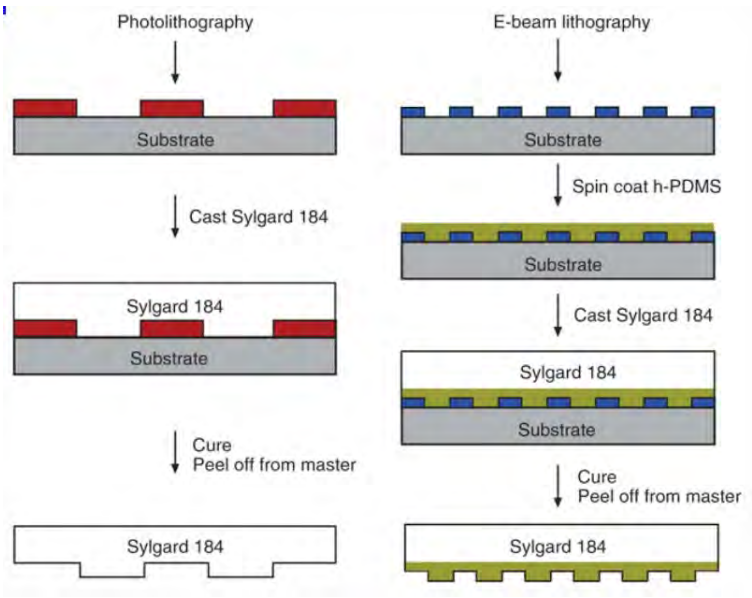

Figure 4.6.: Schematic illustration about the procedure of embossing PDMS.

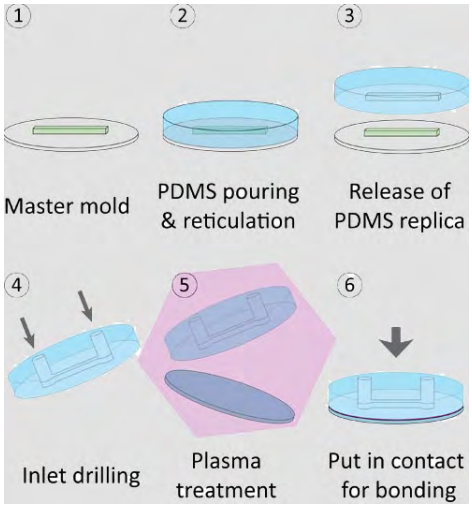

Figure 4.7.: REM of samples.

REAGENTS

1. *Photoresists.* Commonly used negative photoresist, an epoxy-based negative polymer called SU8 photoresist [39], covering the range of film thicknesses from 1 to $> 200\,\mu$m with single spin coat processes. For each film thickness there is a determined number of revolutions per minute. See Fig. 4.9. For instance, choosing a photoresist SU8 − 100, it must be considered some factors: (i) the range of thickness, (ii) the aspect ratio of the patterned reliefs and (iii) the cost and the easiness to work with. For film thicknesses in the submicrometer scale, exists other polymer photoresists, for example, SU8 − 2000 that allow us to work in a short resolution range, 0.5 to 50 μm. This information can be obtained from the MicroChem Corp. site, [40].
2. Sylgard 184 *silicone elastomer base* and Sylgard 184 *elastomer curing agent*, both from Dow Corning [41].

3. SU8 removing; 1-Methoxy-2- acetate (98-100%)
4. Acetone
5. Ethanol

EQUIPMENT

All of the equipment needed for the fabrication can be found in the LMF-CNPEM [42]:

1. Spin coater; for spin coating resists as thin films.
2. UV mask aligner; for photolithography generation. A Karl Suss MJB3 photo-aligner, see Fig. 4.10.
3. Dessicator connected to a vacuum line; for removal bubbles formation.
4. Hotplates; for baking resist films.
5. Nitrogen gas line; for drying stamps and substrates.
6. Oxygen plasma cleaner chamber; for surface modification. A Barrel Asher Plasma Technology SE80, see Fig. 4.14.
7. Optical microscope; for characterizing patterns on masters and stamps at the microscale.
8. Profilometer; for characterizing patterns on masters and stamps at both micro- and nanoscale. A Dektak-150, see Fig. 4.8.

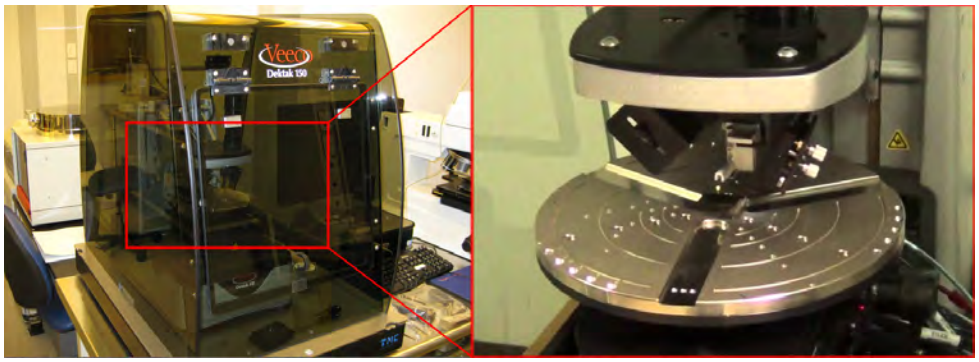

Figure 4.8.: Profilometer Vecco Dektak-150 (left) showing the inner mechanism on right.

PROCEDURE

Design of the pattern

- We used the Autodesk AutoCAD software, by a student licence, to design the patterns.

Fabrication of the photomask

- We have ordered polyester masks from our commercial suppliers/providers. The specifications were commented in sec. 4.2.

Fabrication of the master mold

The fabrication we performed involves 6 steps, from the spinning process until the development of the SU8.

1. Perform photolithographic techniques to fabricate the master mold with patterned SU8 negative-tone photoresit (or SU8 positive-tone) on the quartz substrate surface. To accomplish the best result follow the especifications of the protocole of the respective photoresist. The recommended conditions are: Approximately 1mL of SU8 per inch of substrate diameter. There is an spread and spin cycle at differente accelerations according to Fig. 4.9. In our case we use the $SU8-100$, and for spin coating 2000 rpm for a thickness of 150μm [40]. See Tab. 4.1.

Figure 4.9.: Spin speed vs. thickness curves for $SU8-50$ and $SU8-100$ photoresists.

Product Name	Viscosity (cSt)	Thickness (μms)	Spin Speed (rpm)
SU-8 50	12250	40	3000
		50	2000
		100	1000
SU-8 100	51500	100	3000
		150	2000
		250	1000

Table 4.1.: Thickness vs. spin speed data for $SU8-50$ and $SU8-100$ photoresists. $1\text{cSt} = 1\text{mm}^2 \cdot \text{s}^{-1}$. Water at 20°C has a kinematic viscosity of about 10^{-6}m^2 or 1cSt.

2. After the previous resist-substrate application, it must be pre- and soft- baked to evaporate and densify the film, 10 and 30 minutes at 65°C and 90°C respectively.
3. Then, the sample is exposed to UV light into the UV light mask aligner around 60 and 70 seconds about 365nm. See Fig. 4.10 for photopolimerization initiation.
4. Post baking; 5 and 10 minutes respectively at 65°C and 90°C respectively for densifying and promote polymerization.

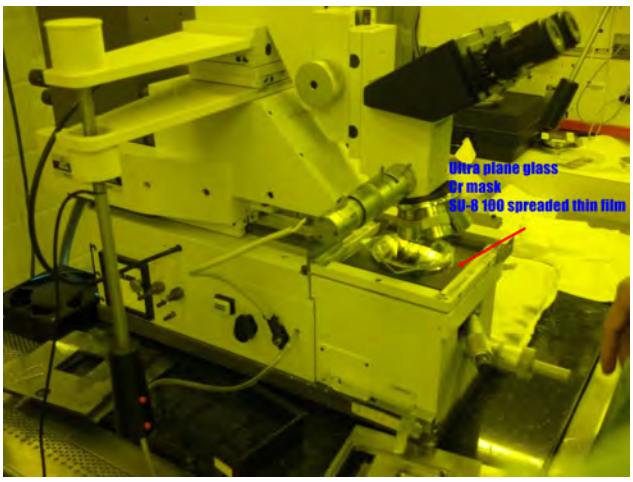

Figure 4.10.: UV mask aligner Karl Suss MJB3 and the sample ready for exposition.

5. Let it cold for about 5 minutes at room temperature for avoiding a thermic shock.
6. Rinse the sample into an specific solvent, 1-Methoxy-2- acetate (98-100%). See Fig. 4.11.

Figure 4.11.: Development of SU-8.

Fabrication of Sylgard 184 PDMS stamp

This stage of 5 steps is about the obtaining of a PDMS stamp, taking account the accumulation of bubbles and being carefull about the thermal shocks.

1. Take a plastic cup and fill with 10 parts of Sylgard 184 base and 1 part of the curing agent by weight. We used approximately 29 g of base and 3 g of curing agent.
2. With a help of a surgical spoon, we mix them completely. Incompleted mixing may affect the curing behaviour, the homogeneity and mechanical properties of the resultant PDMS. The partial mixture is full of trapped bubbles.
3. Remove the bubbles by placing the cup in a desiccator, normally without it, it takes about one day. Connect it to a vacuum system line for about 30 minutes untill all the bubbles disappear.

4. Put the master in a petri dish or in this case we put in a framed arrange, see Fig. 4.12.

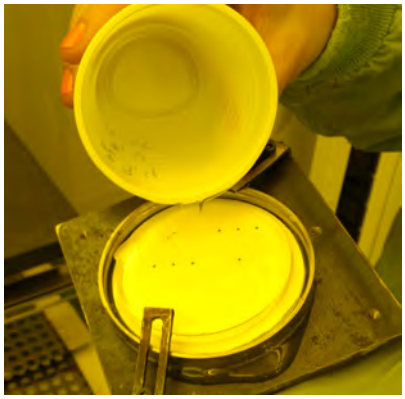

Figure 4.12.: Pouring the mixture of Sylgard onto the mold metal frame.

5. Bake it at 120°C for about 40 minutes.

Fabrication of microfluidic devices

This critical part is important when the final prototypes, microchannels, micropools or any microsystem are created considering the selling or the surface treatment. This is related to the good quality of a plasma oxygen generation.

1. Make the same procedure described previously to obtain the PDMS tamp, or use simply glasses, for selling and close the channels, generated by the master mold.
2. Using a scalpel blade and tweezers, and carefully peel the PDMS stamp off the mold. Cut the PDMS with the desired dimensions for different tamps devices.
3. One may typically use the same master mold to replicate many stamps. Maintain the master mold in a covered container to avoid contamination.
4. Make holes according the structure with the use of a blunt needle. See Fig. 4.13.

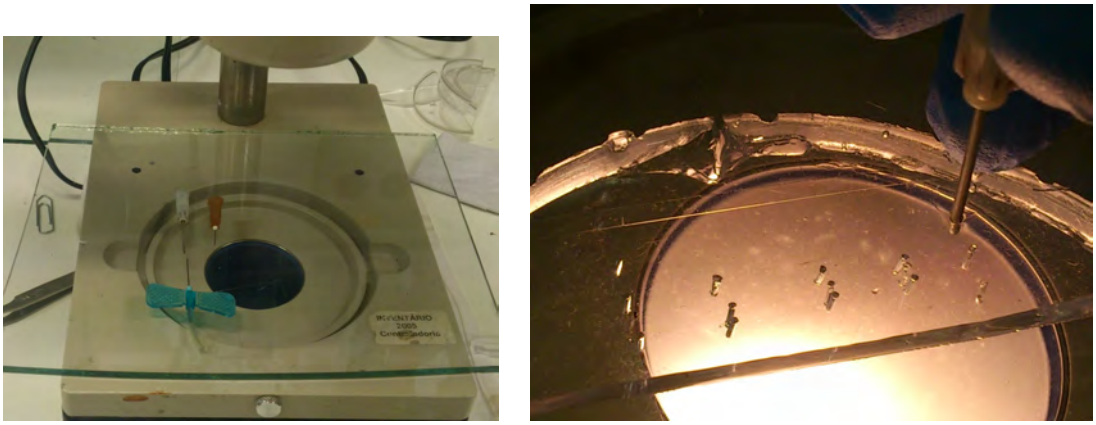

Figure 4.13.: Making holes with a syringe blunt needles.

5. Place the PDMS stamps and tamps in an oxygen plasma cleaner for oxidation for about 2 minutes. Range of inner pressure, 200 mTorr. This treatment generates silanol groups (Si−OH) on the surface of the PDMS replica owing to oxidation. See Fig. 4.14.

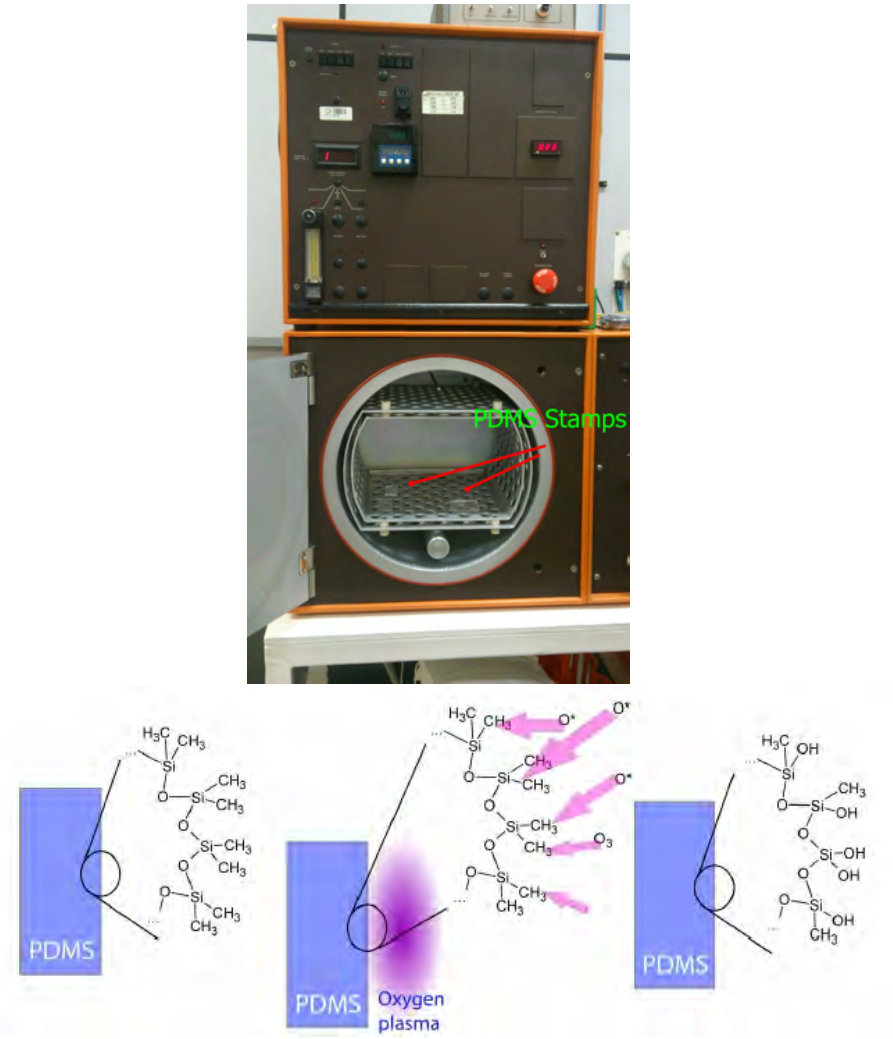

Figure 4.14.: Above; plasma chamber containing PDMS stamps ready to be modified. Below; oxygen ions attacking the surface for deslocating the methyl groups stroungly attached to silice

6. Finally, we have about 20 minutes for manually selling the stamp (with the channels) and the other PDMS or glass tamp. We put the surfaces in contact each other.

Some considerations

- The Fig. 4.15 shows the most common problems when fabricating the master mold. Pairing and sagging of the elastomeric stamp. To avoid this, it must be done previously some optimized calculus for aspect ratios H/L and H/D.

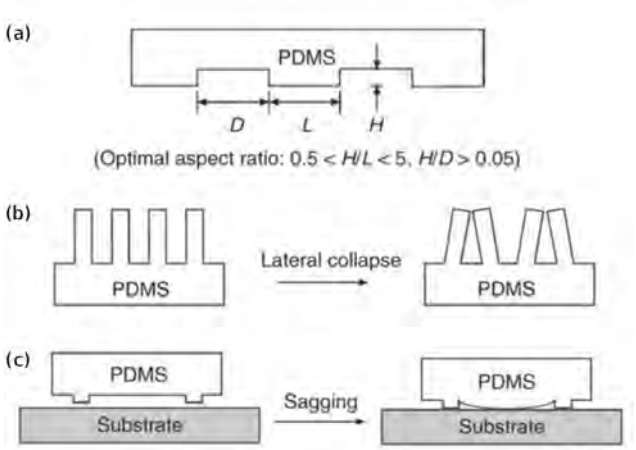

Figure 4.15.: a) PDMS stamps and possible problems that arises because of the softness of the elastomer: b) lateral collapse with commonly aspect ratios $H/L > 5$; and c) sagging of recessed structures with aspect ratios $H/L < 0.5$.

4.4. Partial Results

The Figure 4.15 shows the profile of the master mold for the PDMS generated in the left corner. Some details to consider:

- The cross section is about a quadrangular shape. Not completely with perpendicular lateral walls, probably due to the stage where the SU-8 is exposed to the spreading UV-light.
- The lateral walls are around 75 μm while the top width is near to 198 μm and the bottom one approximately equal to 293 μm .

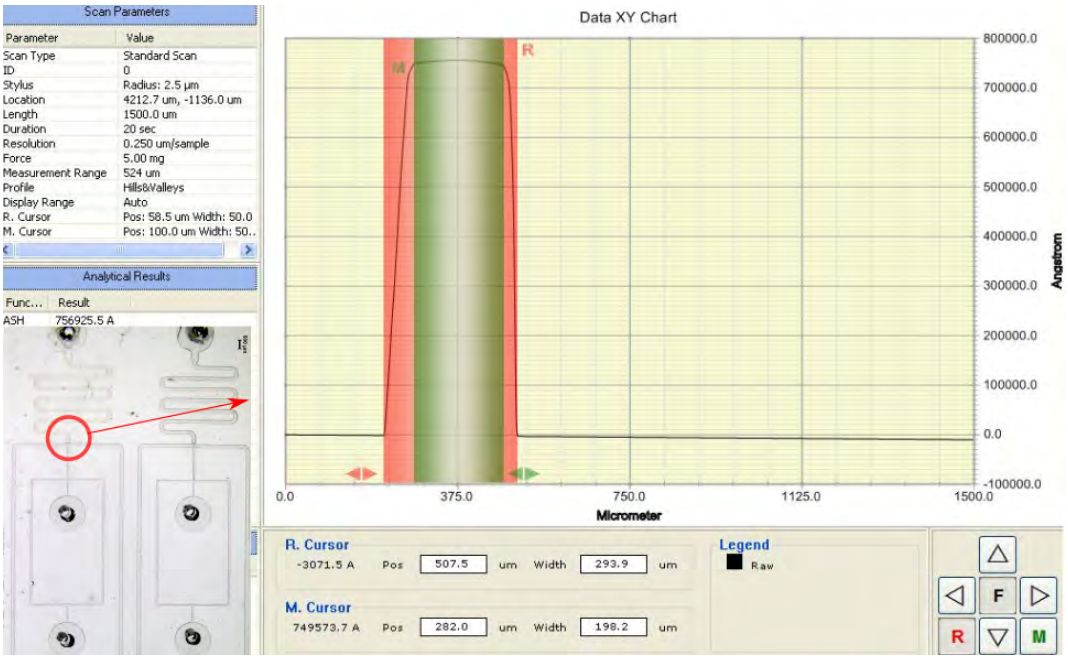

Figure 4.16.: Here is shown the cross section of the SU-8 profile of the sample. We see the inclination of the sample which indicates probably the UV light beam spreading.

The Figure 4.16 shows the microchannels we obtained. We prepare the microdevices by pouring the elastomer over the relieves of the mold. This devices for simple and double emulsions generation.

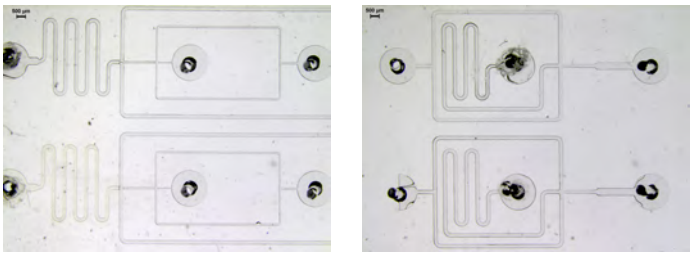

Figure 4.17.: Microchannels fabricated for emulsions in PDMS for double (left) and simple (right) emulsions respectively.

5. Microfluidic System Implementation

Introduction

Biological experiments happens frequently in aqueous medium. The majority of biology researchers and related community manipulates small volumes of liquid, around microliters, for mixing, moving, incubating, separating, controlling by handling tools such as pippete, etc [37, 11]. Microfluidics has overcomed these problems. The last 20 years, automated liquid handlers and microfluidic devices and new tools are being developed [1] to get a better control of volumes and fluxes.

Here we present an inexpensive but effective automated open source syringe system, we called MiniDrop 1.0, created entirely at **LabM**^{2} to run microfluidics chips. The main goal of our system was to use a set of open-source components as much possible, and reduce design complexity in a compact and friendly way. This allow leads to end-users without electronics skills to a better manupulation of microfluidic debices. The system was developed entirely using acrylic plates and polylactic (PLA) acid developed in mechanical lathe and 3D printer machines respectively.

The MiniDrop 1.0 is used for many applications, including controlled fluxes entering and exiting the channels as we shall see in subsequent chapters.

5.1. Micropumps

Technologies have the capability of manipulating and rapid replicating hundreds of experiments in biology. In particular; automated pumps have the potential to enhance the manipulation at the microscale volumes. MiniDrop 1.0 operates pumps with high precision volumes, at the order of few nanoliters and controlling two flow rates.

Existing commercial syringe pumps are good solutions, but they are in a variety of types and programming presentations that normally are expensives and closed source code. This makes difficult a particular group of researches to follow a certain protocol due to errors in customized settings for each pump machine. Besides that, unexpected hardware or software problems practically stop the research temporarily until specialized people find fixe them [43].

We have developed an open-source syringe pump that can be fabricated with low cost investment and to be operated in an easy way by a computer program or manually by push button controllers.

Commonly most commercial imported syringe pumps are capable with the control of only one flow rate [44, 45]. Our MiniDrop 1.0 is able to manipulate two flow rates simultaneously.

The first idea and fitting together

Using Autodesk AutoCAD software we generated a collection of design drawings for individual component of the system. The Fig. 5.1 shows a conceptual idea we developed after many failed attemps. In brief words, it consists of a platform where it is placed the holder for its respective motor steppers and precision syringes.

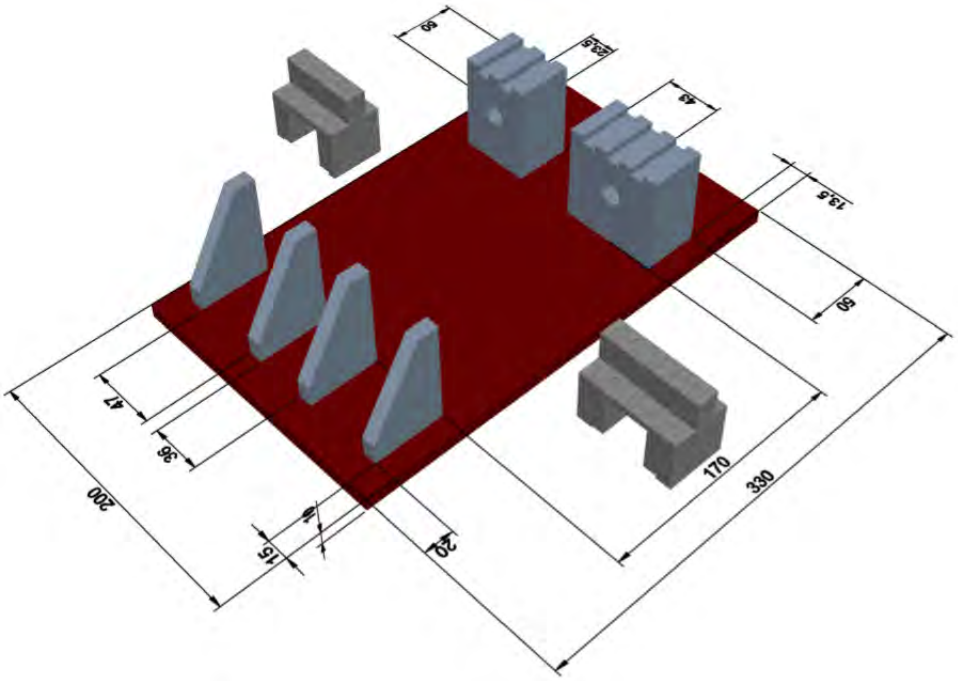

Figure 5.1.: Infusion pumps we designed and developed in the LabM^2.

According to the pictures above, the syringe pump is designed for facility in use and assembly. No mechanical background is required, just fitting and screwing together. Next, we programmed it using an open-source code, using a microcontroller and drivers we will describe in the next sections. This gives the user the desire of controlling the pump in terms of volumes and flow rates to move.

5.2. Automation

The system pushes or pulls the syringes in a finite number of discrete steps. We used a HWIN carrier, see Fig. 5.3, which moves in one direction, 4.25 mm per turn. Connected to microsteppers and controlled by a circuit board composed by an ATmega328 microcontroller and carrier drivers. See Fig. 5.5. Here we will describe some tools and implementation step by step we considered.

5.2.1. Motor steppers

A motor stepper is a brushless DC electric motor that divides its rotation into a number of equal steps and equal angles. The motor stepper is composed by multiple electromagnets

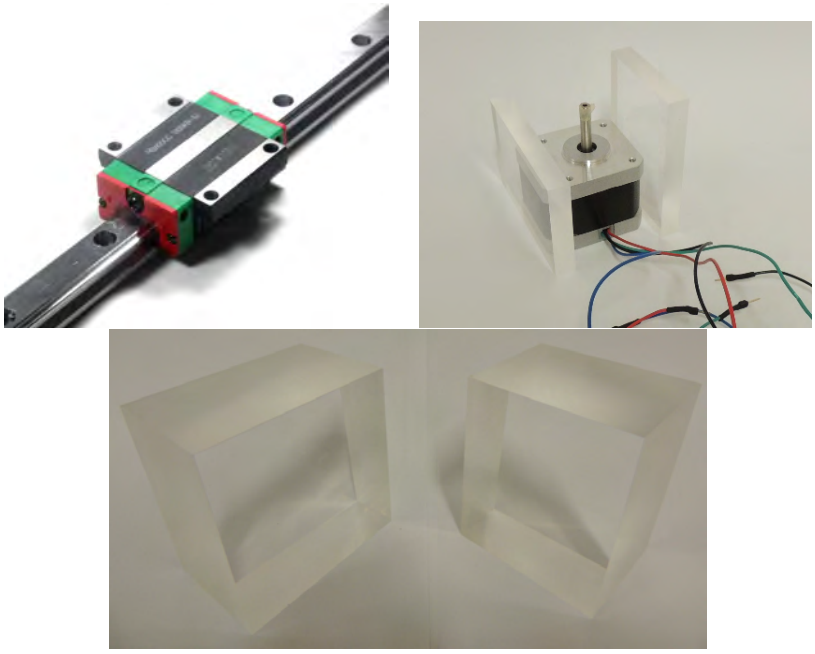

Figure 5.2.: Linear guideway, NEMA 17 stepper motor and acrylic blocks, these last ones were made in the lathe machine at the Physics Institute in the mechanical workshop.

arranged around a central gear-shaped piece of iron. These electromagnets are energized by and external driver circuit or a micro controller [46]. The mechanism of rotation is depicted in the Fig. 5.4.

The motor turns a number of steps to complete a turn. We use a 8.0 kg-cm, 6 Wire, NEMA 23 stepping motor.

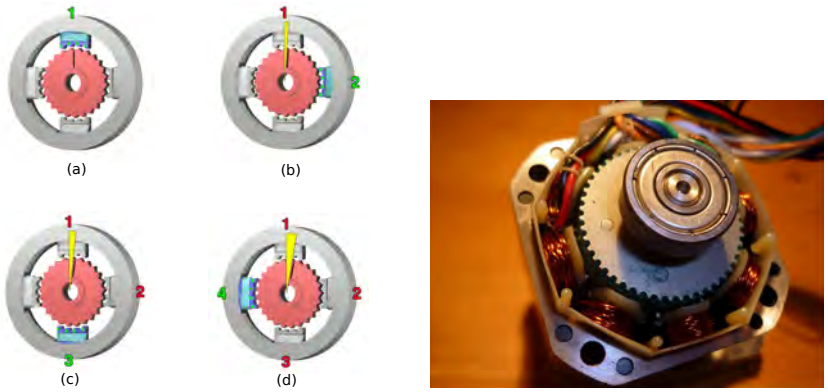

Figure 5.4.: Left; general scheme mechanism about an unipolar motor stepper works. Every time the selected solenoid is turned on orderly, the central magnet, in red, continuously rotates a small angle in one direction. Right; inside a motor steeper. See the number of solenoid coils distributed round the magnet. Pictures adapted from [47].

5.2.2. Drivers Pololu 8825

This breakout board for TI's (Texas Instruments) DRV8825 microsteeping stepper motor driver permits to adjust a current limiting supplied, an over-current and over-temperature

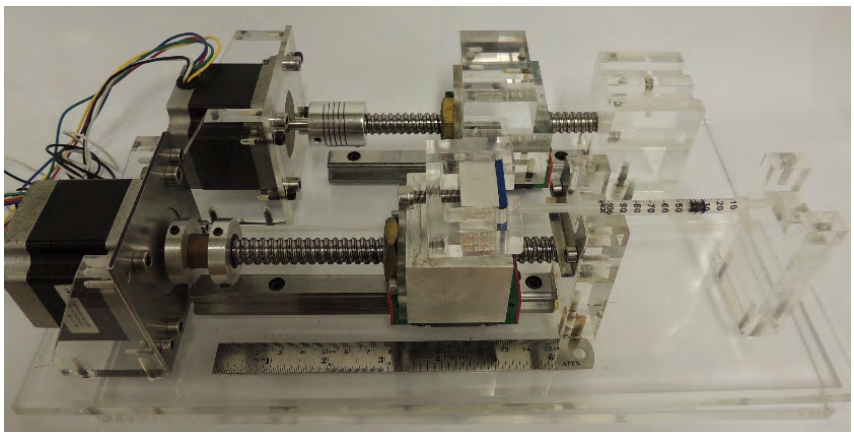

Figure 5.3.: Pumps specialized to move in the range distance of few milimeters per hour.

protection, and six microstep resolutions (down to 1/32-step). It operates from 8.2 V to 45 V and can deliver approximately 1.5 A per phase without a heat dissipator. See Fig. 5.5.

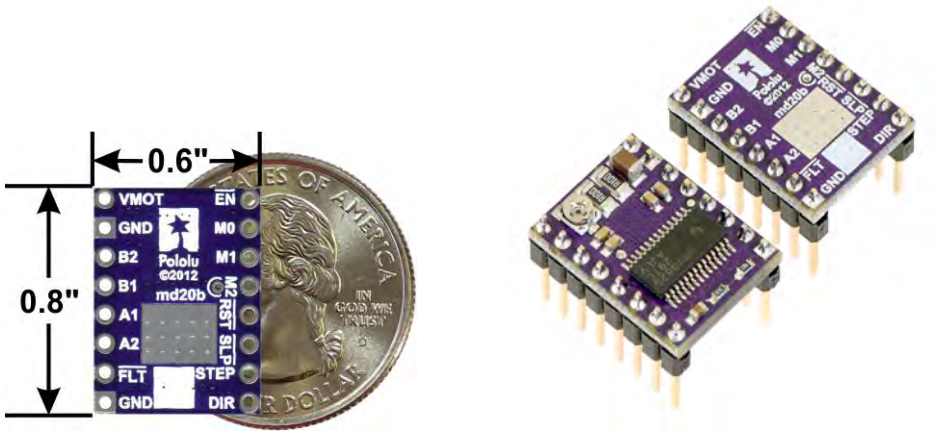

(a) Its small size makes accesible for those who are developing a circtuit.

(b) Rarely the DRV8825 needs a heat dissipator.

Figure 5.5.: Breakboard with the TI's DRV8824/DRV8825 stepper motor driver carrier. Pictures were taken from [48].

This stepper motor driver permits the control of one bipolar stepper motor at up to 2.2 A output current per coil [48]. The input selectors (MODE0, MODE1 and MODE2) enables 6 different microsteps selection modes according to the Tab. 5.1. Each of these selectors have internal 100 kΩ pull down resistors.

MODE 0	MODE 1	MODE 2	Microstep resolution
Low	Low	Low	Full step
High	Low	Low	Half step
Low	High	Low	1/4 step
High	High	Low	1/8 step
Low	Low	High	1/16 step
High	Low	High	1/32 step

Table 5.1.: Microstep selection according to M0, M1 and M2 inputs modes.

Control inputs

When you control each STEP inputs, it is corresponds to every microstep of the stepper motor in the direction selected by the DIR pin. These inputs are internally pulled low by default through internal 100 kΩ . This means that if this pin is disconected, the motor rotates in one direction.

Another not relevant but important considerations are the power states inputs: $\overline{\text{RESET}}$, $\overline{\text{SLEEP}}$ and $\overline{\text{ENBL}}$. They three are pulled low by default, the first one through a 1 MΩ resistor and the second and third ones through internal 100 kΩ pull-down resistor. The $\overline{\text{RESET}}$ and $\overline{\text{SLEEP}}$ must be pull high connected to enable the driver. The default state of the $\overline{\text{ENBL}}$ pin is to enable the driver, so this pin can be left disconnected. See Fig. 5.6.

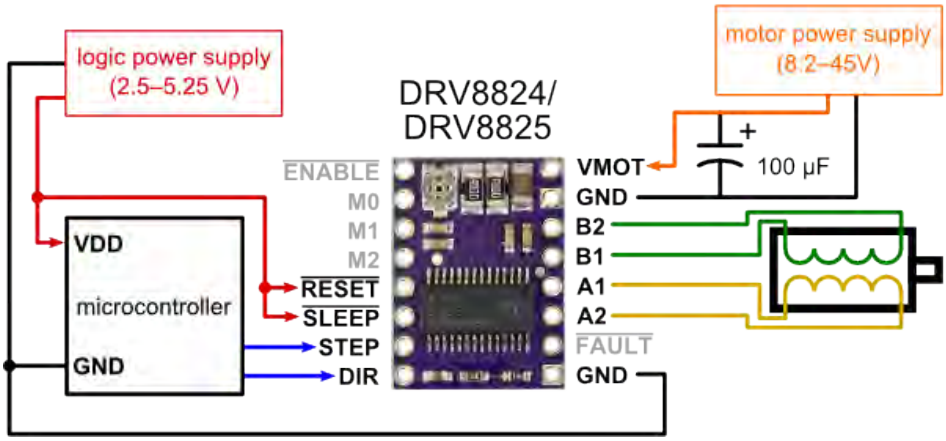

Figure 5.6.: Minimal wiring for connecting a microcontroller to a DRV8824/882 driver and stepper motors represented by A1, A2, B1 e B2. This figure was taken from [48].

Current limiting

The current limit relates to the reference voltage numerically as follows:

$$\text{Current Limit} = \text{VREF} \times 2 \quad , \tag{5.1}$$

This means, for a voltage of 0.5 V, the current limit is 1 A. See the datasheet for more information, this rates depends on mode to mode selection modes.

5.2.3. ATmega328

This is a single-chip microcontroller created by Atmel in the megaAVR family [40]. It combines 32KB ISP flash memory with read-while-write capabilities, 1KB EEPROM, 2KB SRAM, 23 general purpose I/O lines, 32 general purpose working refisters, three flexible timer/counters with compare modes, internal and external interrups, serial programmable USART, a byte-oriented 2-wire serial interface, SPI serial port, 6-channel 10-bit A/D converter (8-channels in TQFP and QFN/MLF packages), programmable watchdog timer with internal oscillator, and five software selectable power saving modes. This device operates between 1.8-5.5 volts. See Fig. 5.7.

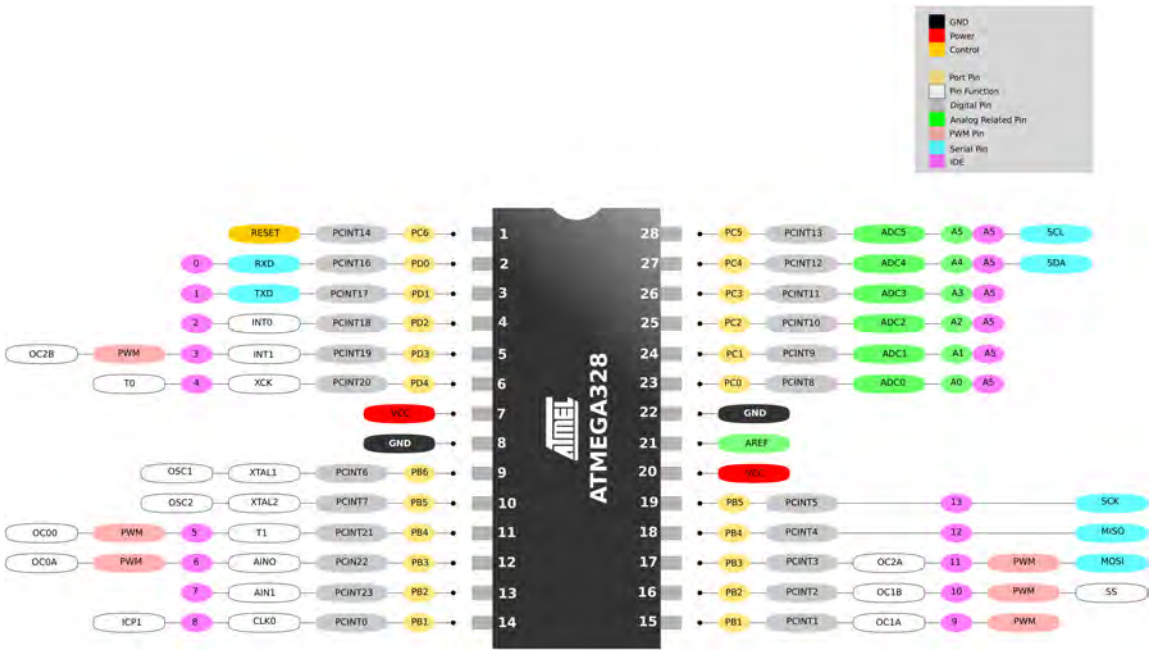

Figure 5.7.: ATmega 328 pinout.

Algorithm

The control for two motor stepper requires the order execution for HIGH and LOW signals alternatively, considering they both can take different values of their periods. See Fig. 5.8.

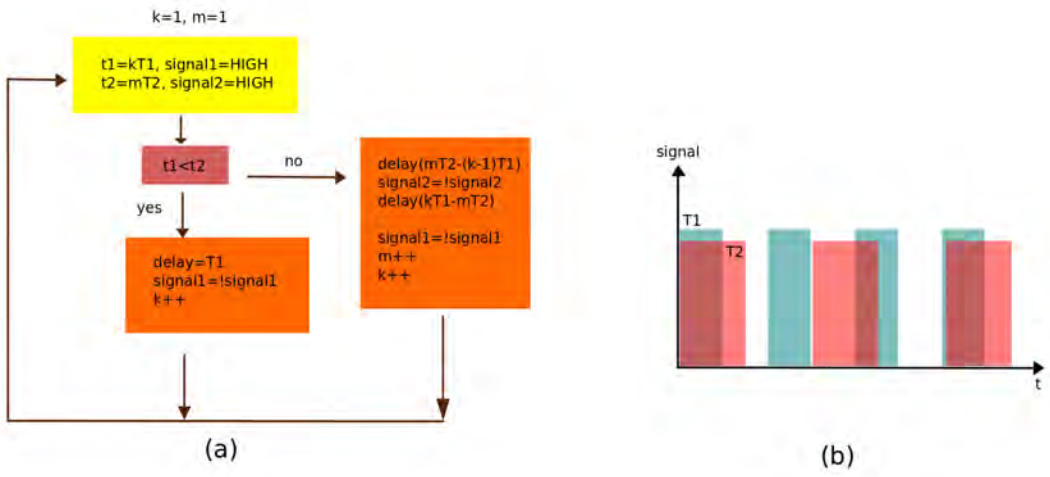

Figure 5.8.: Algorithm of the flow diagram (a) for the manipulation of two different motor steppers periods as shown in (b).

5.3. Auxiliar components and Software tools

In order to auxiliate the accessory mechanical development, we were found interesting hardware and software ideas and tools. One of the most relevant was the usage of a 3D printer and a necessity of an inverted microscope.

5.3.1. Microscope

We have developed a microscope attended to solve a problem: In our project we wanted an inverted microscope.

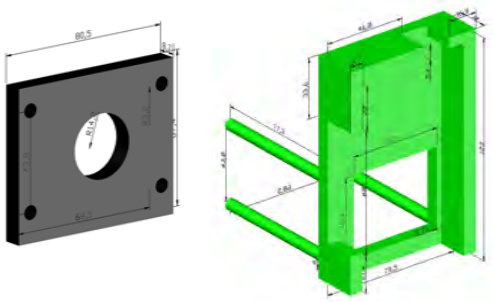

Figure 5.9.: Microscope design concerning to the platform for camera holder.

5.3.2. 3D Printing

Is a hardware and software available for creating solid pieces. There are a variety of 3D printers depended of the technology used. More common in Brazil.

- Fuse Deposition Modeling (FDM) 3D printer. See Fig. 5.11.
- Stereolithography/Digital Light Processing (SLA/DYP) 3D printer.

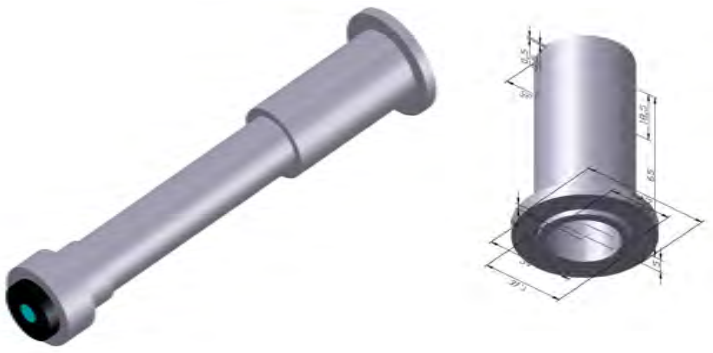

Figure 5.10.: Microscope design concerning to the tube connector between the ocular and the objective and and z- calibration.

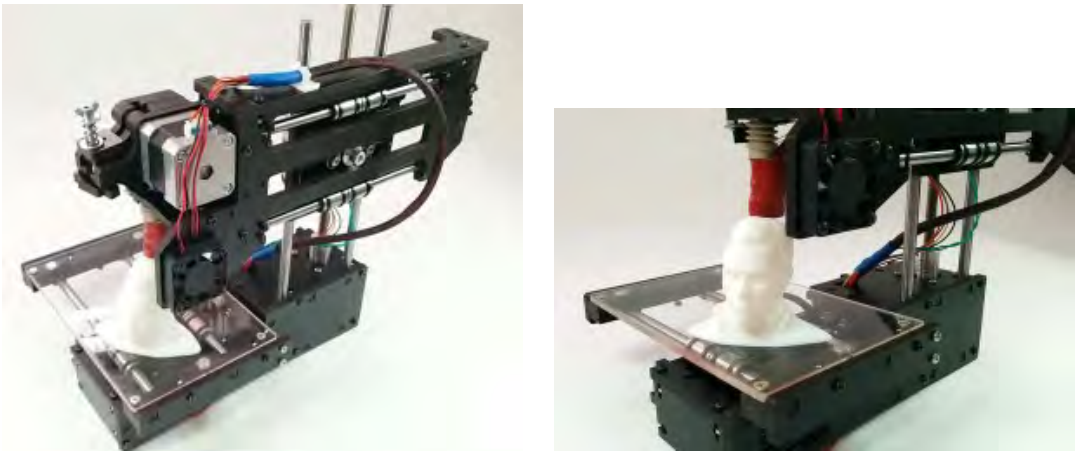

Figure 5.11.: TatoBaby 3D printer used during almost all the research project. Photos adapted from [49].

OpenSCAD

It is a CAD free software application for building 3D CAD (computer-aided designed) solids, [50] through a platform code programming compiler based in C++. This software is mainly oriented for planning and creating models: Machine parts, making interface accessories as well as produce, reproduce and enhance obsolete accesories, etc.

OpenSCAD reads a script file which gives the designer full control over the modelling process. Along the research development has solved to project several geometries as shown in Fig. 5.12 and to generate code coordinates which we used strongly in chapter 8 for an enhanced mesh generator.

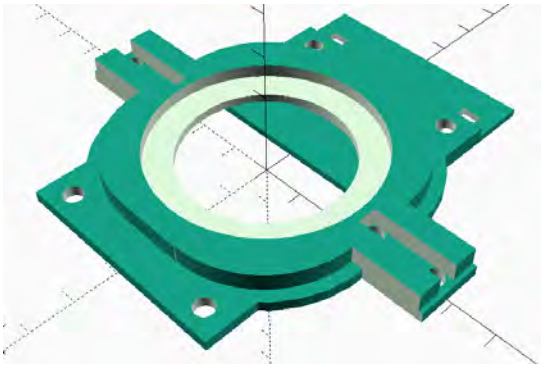

Figure 5.12.: Holder bases for samples. It consists of two main pieces which coupled each other provides a support for the sample.

5.4. All in a “MiniDrop 1.0”

All we mentioned so far it has been traduced in the most friendly and simplest as possible for not specialized user and people who is not involved with electronics or software manipulation. The first version of our micropump controler is shown in Fig. 5.13.

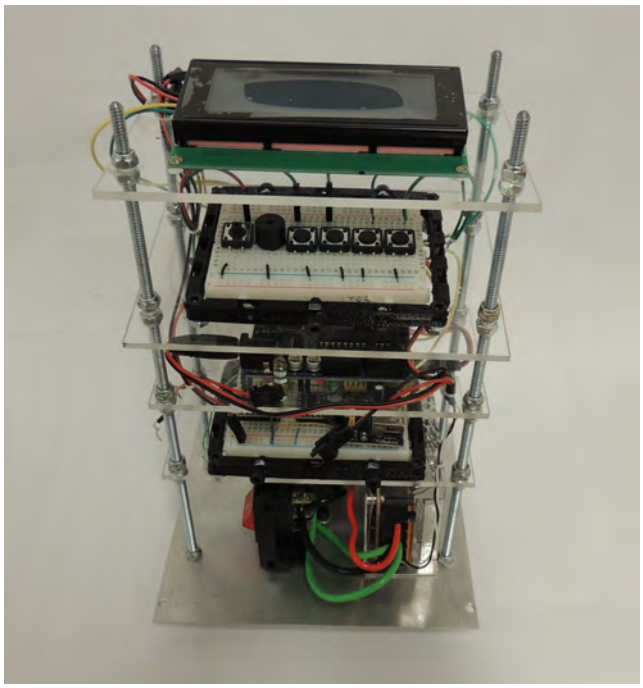

Figure 5.13.: MiniDrop 1.0. System controller developed completely at **LabM**^{2}.

Features

- Advance per step: Depends of the microstep we are using. A maximum precision is around 18.75 nL by step. Note that when working with smaller microsteps, we lose torque which could be a huge problem in microfluidics.

- Syringe pump for infuse/withdraw and push/pull programmable mechanism.
- The system holds until 3 syringes. See Tab. 5.2. One for volumes under 50 mL and the other ones for those under 1 mL.
- It manipulates two different flow rates.
- It manipulates liquid fluxes at very low flow rates. See Tab. 5.2.
- For an insuline syringe, the precision rounds the order of few nanoliters.

Specifications

For a 1 mL insulin syringe, althought there is not necessary a restriction, a minor syringe volume provides a better precision. In the near future we expect to test microliter Hamilton syringes [51], ranging from 0.05 μL to 5 μL.

Specifications	
Drive Motor	1.8º Stepper Motor [47]
Environmental Temperature Tested	21- 33 ºC
Stable Flow Rate	10 μL/min
Maximum Precision	18.75 nL
Pusher Travel Minimum	2 mm/32
Input Power	$12 - 24$ V
Motor Control Drive	Microprocessor, 1 - 1/32 microstepping
Number of Syringes	1 - 3
Number of Microsteps per one revolution	200 - 6400
Pump Function	Infuse/Withdraw
Syringe Rack Type	bellow 1ml

Table 5.2.: Specifications of syringe pump MiniDrop 1.0 . Flow rate minimum was calculated based on an insulin syringe. There is not restriction in using minor syringe volumes.

Further prospects

- We expect programming the MiniDrop 1.0 system, based on a ATmega 328 microcontroller, for a more friendly user interface using a LCD touch screen.
- We expect to focus in fluxes every time smaller. By changing the insuline syringe to a Hamilton syringes [51] we can reduce 20 times smaller in flux and volume.
- We need to enhance the torque of the Motor steps when using microsteppers. Probably the adition of an electronic filter shield can help.

6. Surfactants

6.1. Frustrated Pairs

A *surfactant* is a molecule that has two different parts with opposite characteristics. *Hydrophilic*, eager to mix with water and *hydrophobic* - which abhors water. The first one could be composed by an ion, which compose the "polar head". Tipically this head likes liquids with a high dielectric constant such as water. In other cases, this head is composed by a short chain of neutral units that is soluble in water. An instance of this, POE (polyethylene oxide), formed of units of the type $CH_2{-}CH_2{-}O$. The hydrophobic part is simply formed by one or more aliphatic chains of the type $CH_3(CH_2)_n$. The Fig. 6.1 shows examples of different surfactants and Tab. 6.1 gives a somewhat general view of the hydrophilic and hydrophobic groups that are commonly used.

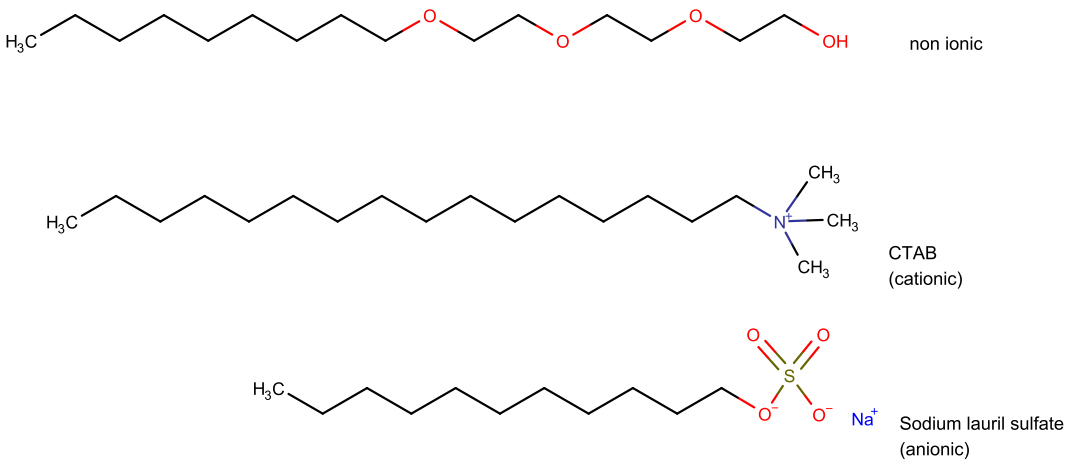

Figure 6.1.: Examples of surfactants.

Hydrophobic part		Hydrophilic part	
Formula	Name	Formula	Name
$CH_3{-}(CH_2)_n{}^-$	Alkyl	$-O{-}SO_3{}^-Na$	Sulfate
$CH_3{-}(CH_2CH_3CH_2)_n{}^-$	Branched alkyl	$-CO{-}O^-Na^+$	Carboxylate
$CH_3{-}(CH_2)_n{}^-$phenyl	Alkyl phenyl	$-N^+(CH_3)Cl^-$	Quaternary ammonium
$CF_3{-}(CF_2)_n{}^-$	Perfluoroalkyl	$-(O{-}CH_2{-}CH_2)_nOH$	Polyethoxy

Table 6.1.: Usual constituents of surfactants. Table adapted from [52].

Both partners are bound together but having different tastes. But, how will such couples behave either individually or in large numbers? We proceed to analyze a few response at the molecular level.

A consequence of surfactant adsorption is the apparition of an expanding force, said $\boldsymbol{\pi}$ the expanding pressure (surface pressure), acting against the normal interfacial tension. This is,

$$\gamma = \gamma_{\text{solvent}} - \boldsymbol{\pi} \quad , \tag{6.1}$$

where γ represents the interfacial tension. Therefore, surfactants tend to lower interfacial tension. For instance, in case $\boldsymbol{\pi} \approx \gamma_{\text{solvent}}$, emulsification can take place because only small quantity surface energy is required.

6.1.1. Notion of Hydrophilic/Lipophilic Balance (HLB)

To answer the previous question we need to know which partner is dominant, this is asking the surfactant is more soluble in water or in oil. Oil is simply a saturated hydrocarbon. Imagine we have a test tube with two liquids, water and oil, with a small quantity of a surfactant. Let us examine what happens with their concentrations in oil c_o and water c_ω[1] at the equilibrium,

$$\frac{c_o}{c_\omega} = k \quad , \tag{6.2}$$

which is known as the *segregation coefficient*. It is easy to imagine that for $k > 1$, we are dealing with a long aliphatic chain, whereas those for which $k < 1$ have a short one. Although this classification has sense it faces some restrictions.

- Which particular oil is chosen has an influence.
- Sometimes surfactants are insoluble in water (or in oil) which leads to an exceedingly large value of k (or exceedingly small for surfactants insoluble in oil). In both cases measuring k becomes impractical.

For these reasons is convenient to use another definition for k. In 1946 Griffin introduce it based on a simple-minded estimation of the work Δw involved in trasnferring a molecule from water to oil. In general, we must have

$$k = \exp(-\Delta w/\kappa_B T) \quad , \tag{6.3}$$

and the value for the work involved,

$$\Delta w = U_H n_H - U_L n_L \quad , \tag{6.4}$$

[1]For now we disregard the quantity of mass at the interface, because it is negligible in comparison to the mass throught the volume.

where U_H is the transfer energy of one hydrophilic group and n_H is the number of such groups in a molecule. The same correspondences are given for U_L and n_L.

By expressing the Equation 6.3 in a logarithmic scheme

$$\log(k) = m_L n_L - m_H n_H \quad , \tag{6.5}$$

where m_L and n_L are phenomenological coefficients at certain temperature.

What has come to be know as the HLB (*hydrophilic lipophilic balance*) is essentially proportional to $\Big(- \log k \Big)$, albeit with slighty modifications. By analogy to the pH values for acids and bases in water, the neutral case for the HLB ($k = 1$) will be assigned the value of 7.

$$HLB = 7 + \alpha(m_H n_H - m_L n_L) = 7 + \alpha(\tilde{m}_H n_H - \tilde{m}_L n_L) \quad , \tag{6.6}$$

where $\tilde{m} = \alpha m$. This normalization coefficient α was chosen to make the HLB values of usual surfactants falls in the range 0 to 14. The Tab. 6.2 shows values for a few important chemical functions.

Hydrophilic groups	$\tilde{m}_H$	Hydrophobic groups	$\tilde{m}_L$
$-CO_2Na$	19.1	$-CH_2$	0.47
$-SO_3Na$	11.0		
$-N-(CH_3)_3-Cl$	9.4		
$-O-$	1.3		
$-OH$	1.9		

Table 6.2.: Some HLB coefficients. Table adapted from [52].

HLB	Applications
$1.5 - 3$	Antifoaming agents
$3 - 6$	Water/oil emulsions
$7 - 9$	Foaming agents/Wetting agents
$8 - 18$	Oil/water emulsions
$13 - 15$	Detergents
$15 - 20$	Dissolving agents for organic products

Table 6.3.: Practical properties associated with HLB ranges. Table adapted from [52].

Again as above we must say that our definition of HLB is not perfect. We are considering that all the entire surfactant groups are completely exposed to water, however, in reality, parts tends to fold back on itself in an attemp to diminish such favorable contacts, and the energy ends up being overestimated.

Currently, numerous authors have proposed improved scales of HLB values. But our purpose in this thesis is merely to explain some of the empirical data in Tab. 6.3.

6.1.1.1. Banckroft Rule

This states as: "The phase in wich an emulsifier is more soluble constitutes the continuous phase". The *Hydrophilic-lipophilic balance* can be used to determine if a surfactant is suitable or not for a required emulsion.

- For O/W emulsions - use emulsifying agents that are more soluble in water that in oil (High HLB surfactant).
- For W/O emulsions - use surfactant solutions that are more soluble in oil than in water (low HLB surfactant).

In other words, according to Bancroft, "the emusion is lead by the emulsifier and this must be soluble in the continuous phase".

6.2. Some Applications of Surfactants

6.2.1. Detergents

The Fig. 6.2 illustrates an idealized function of detergency. Both a support of textule fiber (S) and a particle of grease (P) are hydrophobic. In the presence of a solution of surfactant, very similar to such long tail molecule sodium lauril sulfate (SLS) in Fig. 6.1, their tails attach themselves to the surfaces of both S and P, which renders them hydrophylic by lowering their interfacial energies $\tilde{\gamma}_{PW}$ and $\tilde{\gamma}_{SW}$ with water by a considerable amount. This is,

$$\tilde{\gamma}_{PW} + \tilde{\gamma}_{SW} < \gamma_{PS} \quad , \tag{6.7}$$

where γ_{PS} is the contact energy between P and S (per unit surface). Therefore the surface (S) let the particle (P) go away by a hydrodynamic flow. The mechanism described is dominant but here occurs the following facts:

- *Micellization.* Molecules of greasy dirt are captured by a bunch of surfactants molecules, they round it forming a micelle (with a size less than 10 nm).
- *Emulsification.* What happens here is a similar effect, this time a large drop of grease surrounded by surfactant, with an overall size of about 1μm.

The question is what kind of surfactant is needed for these various functions?

- The surfactant must be soluble in water (this is $HLB > 7$). This is the aliphatic tail should not be too long. If we work with long tails, the penetration process becomes overly sluggish (high HLB, around $13 - 15$).
- The formation of oil in water requires a high HLB. We will discuss this in the next section.

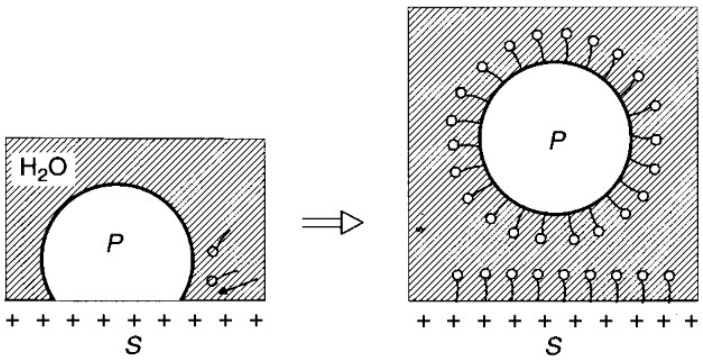

Figure 6.2.: Hydrophobic particle in the presence of a surfactant, which lifts off the microparticle represented by P. Figure adapted from [52].

6.2.2. Emulsions

Emulsions are droplets of water in oil (W/O) or oil in water (O/W) with a typical size of a few microns. See Fig. 6.3. They are produced by forcing mixtures of water, oil and surfactant through a nozzle, rotor, or other mechanical device [52]. We focus the production this mechanical effect, that is, stress, by microfluidic devices and suitable geometries.

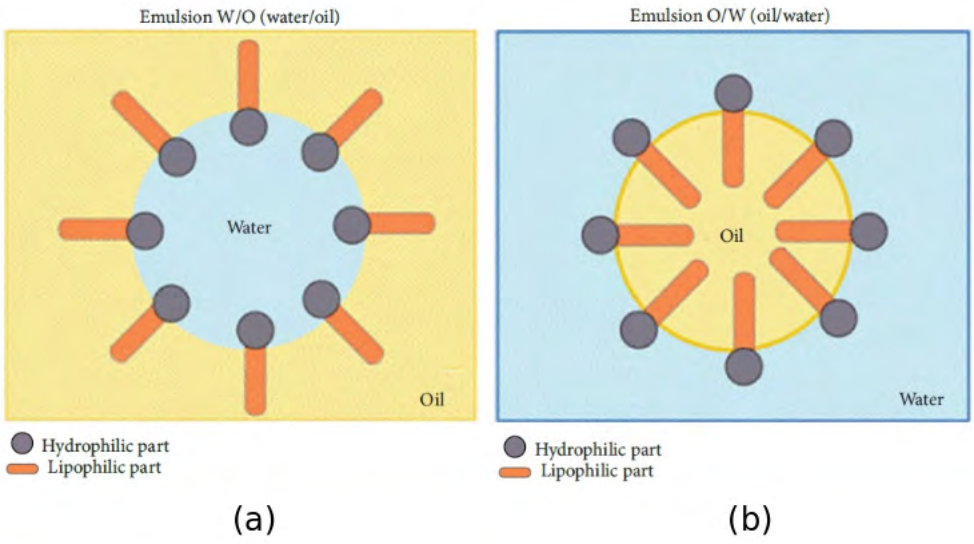

Figure 6.3.: Types of emulsion; Water in Oil shown in (a) and Oil in Water in (b). Figure adapted from [53].

Emulsions are not completely stable even in the presence of a surfactant, there is a finite interfacial energy γ_{OW}. However they help to reduce its energy by a factor of at least 10. For instance, as a rough guideline, a short-lived emulsion requires $\gamma_{OW} = 5\,\mathrm{mJ/m^2}$. A considerable stable emulsion requires an extremely severe $\gamma_{OW} < 5\,\mathrm{mJ/m^2}$. Let us see in more detail for a simple example.

Following the definition of surfactants, *emulsifiers* are substances that stabilize the emulsions. They act mainly at the interface between phases. Typical multiphase systems (two or

more distinctive phases) encountered in foods are water-in-oil (W/O), oil-in-water (O/W), solid-in-oil, gas-in-liquid, gas-, solid- in water, and so on [54].

6.2.2.1. Surface activity

Imagining the molecules in a cup of water. They all experiment the van der Waals forces, equally distributed in all directions, except for those which are at the surface and having a resultant force towards the interior of the liquid. The contracting force at the surface is known as the *surface tension*. Because the surface has a tendency to contract spontaneously in order to minimize the surface area, droplets and bubbles of gas tend to adopt a spherical shape: this reduces the total free energy of the surface. In the case of two immiscible fluids there is an intermolecular force which makes not obvious how the interface will tend to curve. This imbalance generates an interfacial tension, and the interface will adopt a configuration that minimizes the interfacial free energy.

Consider the Fig. 6.4 where all the forces involved stretch the liquid film in one direction. The work done on the system is $F\mathrm{d}x = \gamma \mathrm{d}A$. This kind of work is the path dependent. We can define the work done by the system as $\delta w' = -\gamma \mathrm{d}A$. The energy change is given by

$$\mathrm{d}U = \text{heat absorbed} - \text{work done} \quad , \tag{6.8}$$

$$\mathrm{d}U = T\mathrm{d}S - \Big\{p\mathrm{d}V + (-\gamma \mathrm{d}A)\Big\} \quad , \tag{6.9}$$

$$\mathrm{d}U = T\mathrm{d}S - p\mathrm{d}V - \gamma \mathrm{d}A \quad . \tag{6.10}$$

Using the Gibbs energy representation we have:

$$\mathrm{d}G = \gamma \mathrm{d}A + V\mathrm{d}p - S\mathrm{d}T \quad , \tag{6.11}$$

therefore, for a reversible change at constant temperature and pressure:

$$\mathrm{d}G = \gamma \mathrm{d}A \quad , \tag{6.12}$$

or

$$\gamma = \left(\frac{\mathrm{d}G}{\mathrm{d}A}\right)_{p,T} \quad . \tag{6.13}$$

This result reflects the consistency we showed in the last chapter in terms of Gibbs'. It is sometimes useful to think and represent the surface tension as contracting force around the perimeter of a surface. In units this is equivalent: energy/area = $\mathrm{Jm}^{-2} = \mathrm{Nm}^{-1}$.

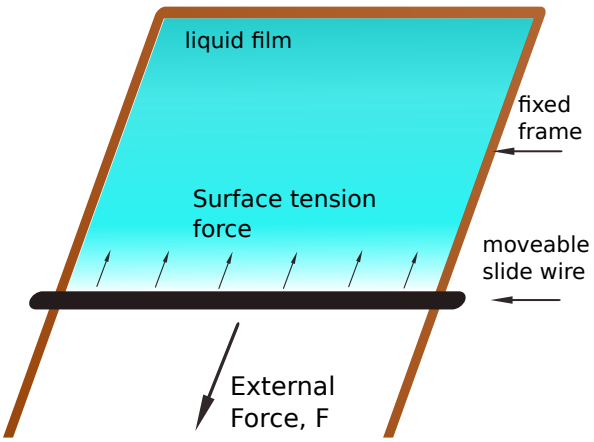

Figure 6.4.: Forced exerted in a liquid film confined to a fixed frame and a moveable slide wire.

The Tab. 6.4 shows some values of surface and interfacial tensions. Mercury surface tension is enormously comparative to the value of water, which is in turn greater than benzene. Another interesting observation is about interfacial tension, which takes intermediate values between the fluids surface tensions involved. For example, at 20 °C, $\gamma_{Bz} > \gamma_{Bz/H_2O} > \gamma_{Bz}$. It must be considered that if the involved phase are the most chemically similar, the interfacial tension is the smallest. Chek the mixture of water and *n*-Octanol phases.

Fluid 1	Fluid 2	Temperature(°C)	Surface tension (mMm^{-1})
Mercury	Air	20	484
Water	Air	20	73
Benzene	Air	20	29
n-Octanol	Air	20	28
Engine oil (30 W)	Air	20	26
Mercury	Water	20	415
Benzene	Water	20	35
n-Octanol	Water	20	9

Table 6.4.: Some values of surface and interfacial tension. Data taken from [55].

6.2.2.2. Work of emulsion formation

Thinking in the previous section about the work made by the moveable wire, the increase in the energy of an emulsion compared to the non-emulsified components is equal to ΔW. This amount of energy can be considered as a measure of the thermodynamic instability of an emulsion.

$$\Delta W = \sigma \cdot \Delta A \quad , \tag{6.14}$$

where σ is the interfacial tension.

The answer about which one is more favorable either oil in water (O/W) or water in oil (W/O) depends on the surfactant used. According to the Bancroft rule; if the surfactant is soluble in oil ($HLB \sim 3$ to 6), it will form W/O emulsions, whereas if it soluble mainly in water ($HLB \sim 8$ to 18), it will form O/W emulsions. This is known as the *Bancroft rule*.

Suppose we wish to emulsify one barrel (approximately 159 L) of oil in water. Imagine we initially have a big drop of about 33.6 cm which is equivalent to 8 drops of 16.8 cm and this to 64 drops of 8.4 cm, and so on. The initial interfacial area is equivalent approximately to $1.42\,\mathrm{m}^2$ and increase to $7.4 \times 10^5\,\mathrm{m}^2$!, by the time we have produced droplets of $0.64\,\mu$m of radius. Note that this increase is five orders of magnitude bigger. Considering the interfacial tension around $35\,\mathrm{mNm}^{-1}$ we would need to increase from 0.05 to 25.9 kJ, this is, we would add absurdity around 26 kJ of energy. If this quantity of energy cannot be provided, say by mechanical shear, then another alternative is to use surfactant chemistry to lower the interfacial free energy or interfacial tension.

The energy plotted in Fig. 6.5 was obtained by multiplying the total area by the interfacial tension.

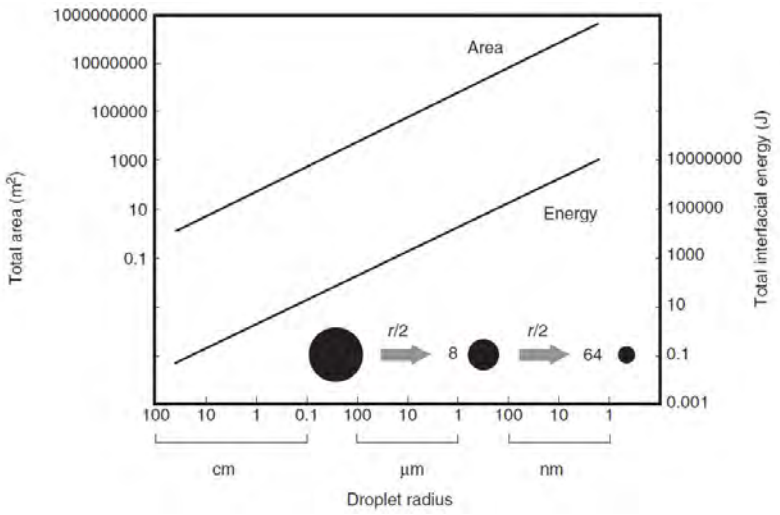

Figure 6.5.: Illustration of total area and energy changes involved in emulsifying one barrel of oil into water by dispersing into progressively droplets. Figure adapted from [55].

Interfacial tension lowering alone may not be sufficient to create an emulsion, in which case other interfacial properties must be adjusted as well. For instance, in the droplets formation extra energy is required to deform previous bigger drops. See Fig. 6.6.

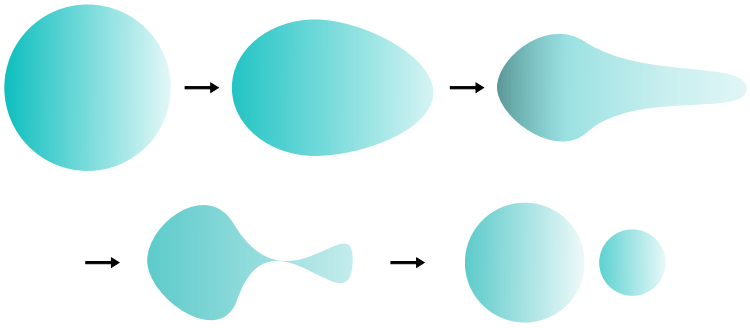

Figure 6.6.: Process of deformation generating smaller drops.

In microfluidics, in laminar flow, this deformation is produced by viscous forces exerted by the surrounding media. If a stream of liquid is injected with low turbulence into another immiscible fluid, this eventually becomes unstable and breaks up into small packets, these are drops. We will see this fact again and in a more detailed way, in the experimental section whith microfluidic devices. In regions with high turbulence the latest process is sooner and produces smaller droplets. The energy required for this formation can be of the order of a thousand of times the thermodynamic energy required discussed earlier. The excess energy is dissipated as heat.

6.2.2.3. The critical Weber number,We

Let us see a phenomenom similar to above, important for the introduction of the Weber number. A liquid sheet flowing through another immiscible fluid or gas. Instability originates waves, leading to separation into ligaments which in turn break up into droplets. See Fig. 6.7.

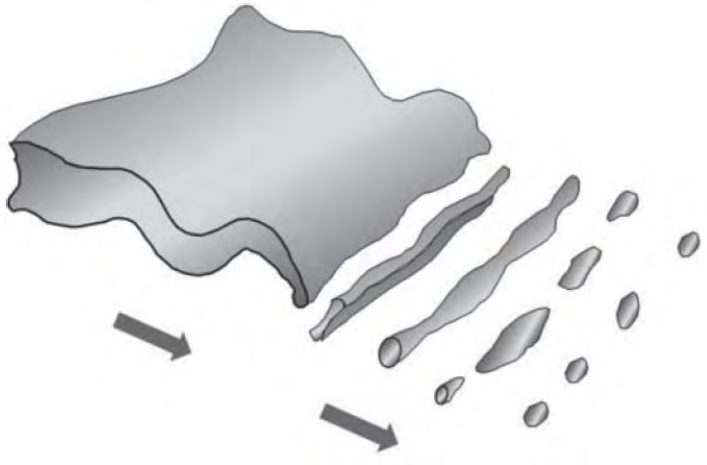

Figure 6.7.: Breaking-up if a liquid sheet under instability. Figure adapted from [55].

This result is influenced by the viscosity of the continuous phase fluid, the amount of mechanical shear produced and the interfacial tension. We parametrize it by the critical Weber number [56] given by

$$We = \frac{\eta_1 \dot{\gamma} R}{\gamma_{12}} \quad , \tag{6.15}$$

where η_1 is the viscosity of the continuous phase, $\dot{\gamma}$ is the shear rate, R is the droplet radius (in case a deformed drop, its characteristic lenght L) produced and γ_{12} is the interfacial tension (here the subscript 2 represents the dispersed phase). For droplet formation in the laminar flow regime, the critical We number ranges from 0.5 to ∞, and depends of the viscosity ratio η_2/η_1 (η_1 for continuous and η_2 for dispersed phases).

Tab. 6.5 shows viscosities for different kinds of oil. Particularly, in the course of our research we used soy beam and canola oils.

Oil samples	pH	Density (ρ) [g/ml]	Dynamic Viscosity (η), [mPa·s]	
	25.5 °C	25.5 °C	25.5 °C	40 °C
Safflower	6.78	0.992	39.7	23.4
Soy beam	6.88	0.920	41.4	23.6
Sunflower	6.02	0.918	41.4	23.1
Canola	5.85	0.929	44.7	25.3
Corn	6.63	0.916	44.7	24.8
Olive	6.96	0.909	43.6	25.6
Hazelnut	6.75	0.919	50.4	26.7
Frying sunflower	5.36	0.915	44.9	24.6

Table 6.5.: Density, pH and dynamic viscosities of oils. Note that for water is 0.89 mPa·s. Data taken from [57].

Fig. 6.8 shows interesting details about the critical We number. For low continuous viscosity phase, we require high-velocity gradients for the droplets deformation. This illustrates very well why turbulent flows are usually needed for emulsification into low-viscosity liquid. According to [55], if $\eta_2/\eta_1 \geqslant 4$, no droplet breaks-up regardless of the We value.

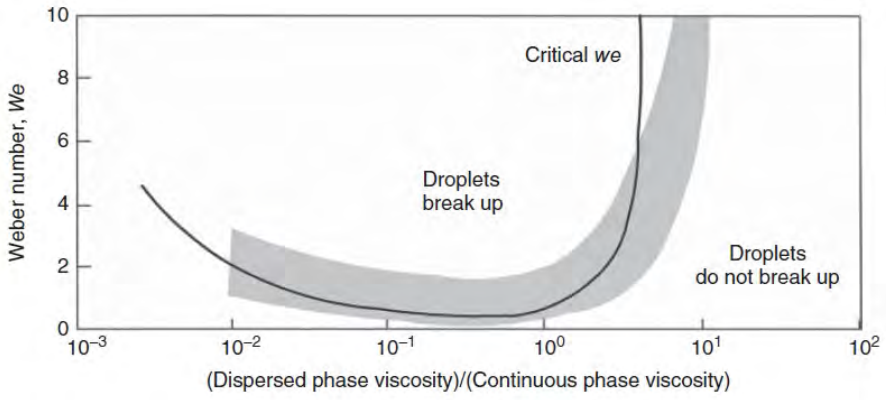

Figure 6.8.: Critical We number for droplets disruption in simple shear flow (curve) and for the resulting average droplet droplet size in a colloid mill (hatched area), as a function of the viscosity ratio of dispersed to continuous phase. Figure adapted from [55, 58].

Fig. 6.9 shows a useful relationship that can be used to predict which kind of emulsion will occur, water-in-oil (W/O) or oil-in-water (O/W). From this figure we can note that for a given ratio η_2/η_1 (dispersed to continuous) and reducing the interfacial tension (lowering the energy for breaking-up the droplet) the critical We number is increased.

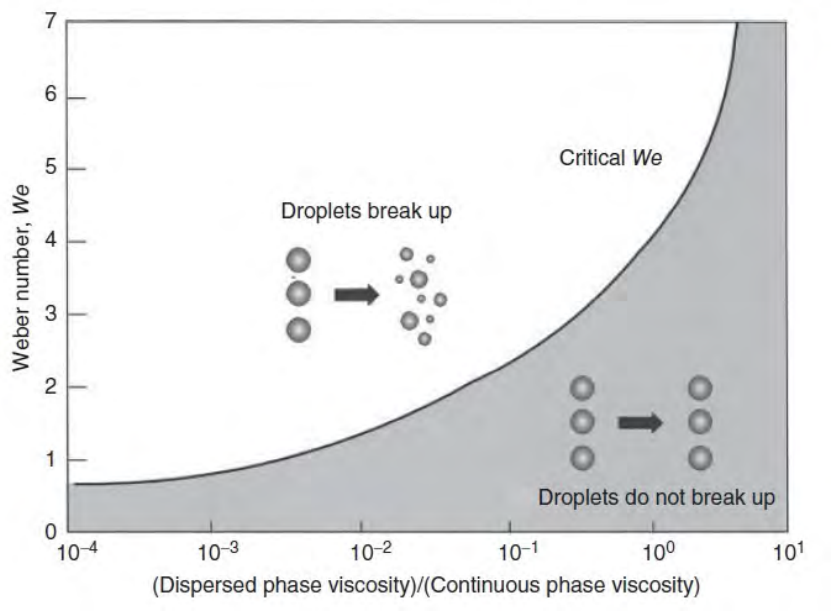

Figure 6.9.: Droplet break-up as a function of viscosity ratio. The solid line represents the critical We number value above which droplet break-up. Figure adapted from [59].

6.2.3. PGPR

Polyglycerol polyricinoleate (PGPR; trade name: ADMUL WOL) is an interesting emulsifier. Due to the property of water binding capacity of the long hydrophilic polyglycerol chain which allows the stable water-in-oil (W/O) emulsion formation. This is, it is soluble in fats and oils and insoluble in water and ethanol. Water-in-oil (W/O) emulsions are less commom than oil-in-water (O/W) ones and fewer studies are dedicated to them. Another authors use this based emulsions for obtaining more complex emulsions ($W_1/O/W_2$ with different aqueous solutions and surfactants) [60]. PGPR is an emulsifier commonly used along with lecithin to diminish the viscosity of chocolate covertures [61]. It is also employed in the fabrication of low fat content products; butter, margarines and salad dressings. Many countries consider officially PGPR does not constitute a human health hazardous [54, 62]. The consistent of PGPR is of a viscous liquid, yellowish, and strongly lipophilic.

Chemically structural, PGPR is made up from polymerized glycerol and polymerized ricinoleic acid. See Fig. 6.10. Glycerol molecules connected by ether bonds, with ricinoleic acid side chains connected by ester bonds [54].

Ricinoleic acid (12-hydroxy-9-cis-octadecenoic acid) is an unsaturated omega-9 fatty acid, see Fig. 6.11, that naturally occurs in mature castor plant (*Ricinus communis L.*, Euphorbiaceae) seeds.

Polymerized ricinoleic acid (see Fig. 6.12) commonly called as ricinoleic acid estolides (any class of long-chain esthers formed usually by hydroxy acids by reaction of two molecules either of the same or of different acids) are obtained by different processes out of the scope of this thesis.

The Fig. 6.13 shows the hydrophilic groups in water phase.

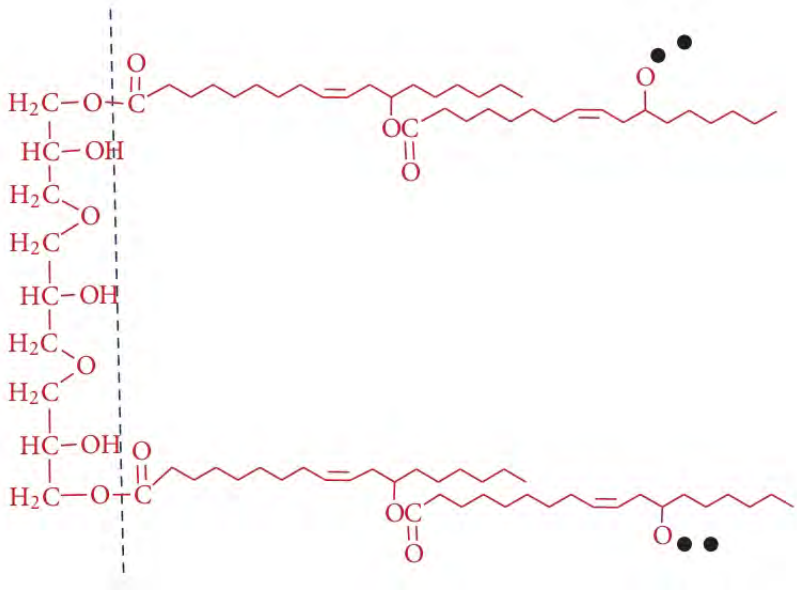

Figure 6.10.: Chemical structure of PGPR. Black dotes denote polyricinoleic acid chains. Figure adapted from [54].

Figure 6.11.: Chemical Structure of ricinoleic acid. Figure adapted from [54].

Some interesting studies show the effect of calcium salts and different PGPR surfactant concentration on the stability of water-in-oil (W/O) emulsions [64].

6.3. Partial Results

We prepared the samples following the concentration procedure bellow. These solutions were introduced in the inputs 1 and 2 respectively.

- Input 1 - water phase concentration: 1 mL of water + 50 mg of red dye. However, eventually we used blue or green.
- Input 2- oil phase concentration: 1 mL of canola's oil + PGPR surfactant (4 %).

The control operation mode used by our micropumps was about 100 μL/h of flux for the input 1 and input 2. This mode obeys to a 1/32 microstep according to Tab. 5.1.

We obtain the droplets showed in Fig. 6.14 in the microdevice showed in it.

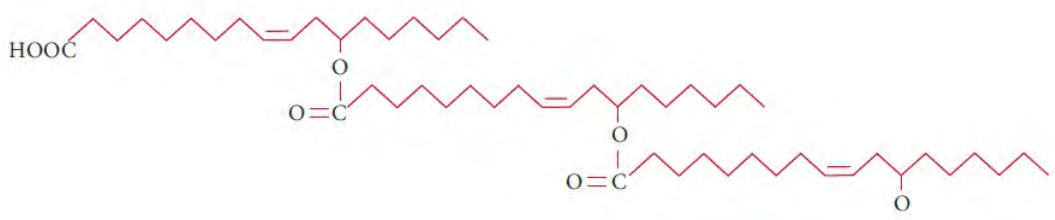

Figure 6.12.: Chemical structure of polyricinoleic acid. Figure adapted from [63].

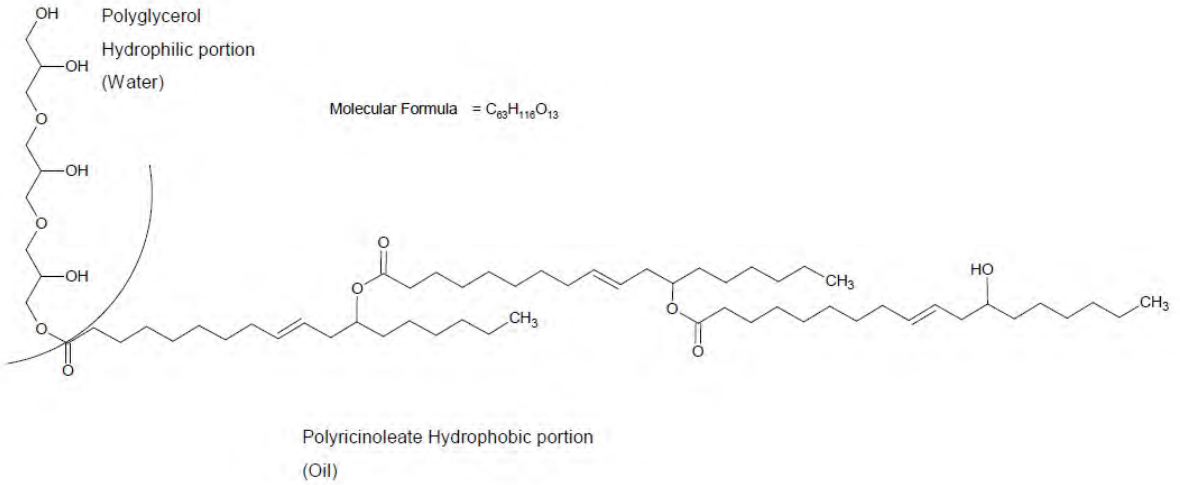

Figure 6.13.: Molecular structure of PGPR in water. Figure adapted from [63].

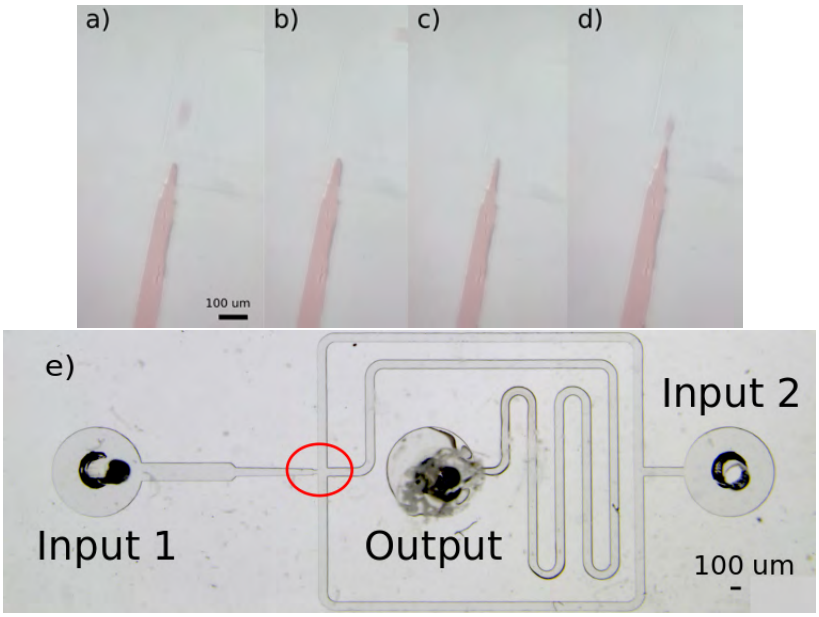

Figure 6.14.: Generation of a droplet within a microchannel for simple emulsions, (a) to (d). It is possible to see the stages about how a droplet is formed. The competition of surface tension forces promotes the rupture and separation of the plug of water. The region of the channels used in the micro device is in red (e).

Following a second arrangement in the microdevice showed in Fig. 6.15 (c), using the same solution concentration of the previous arrangement.

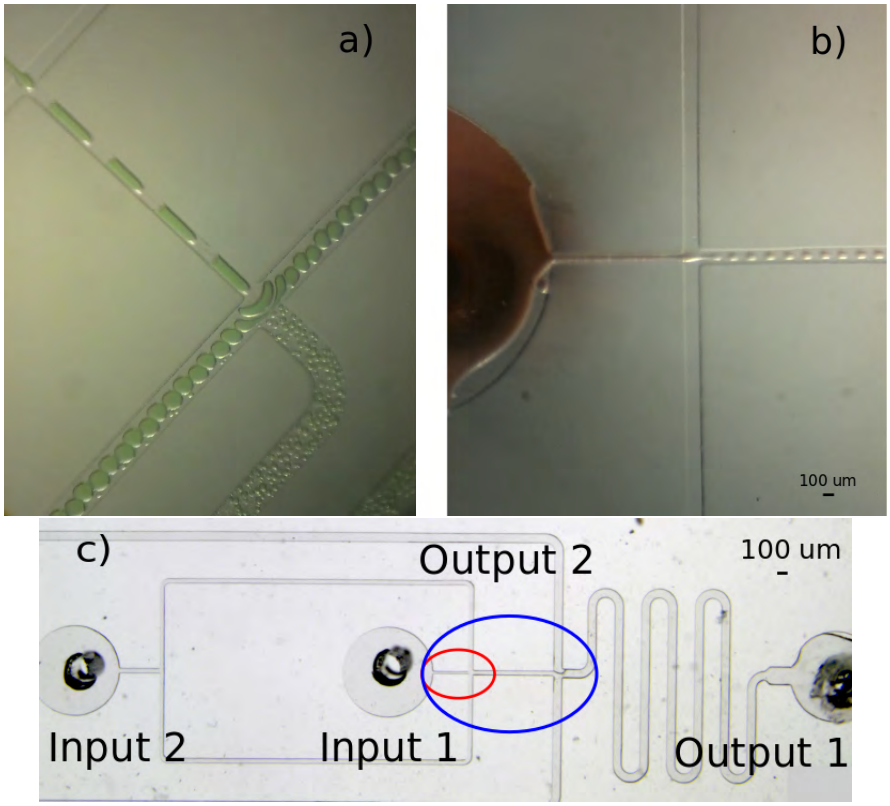

Figure 6.15.: This experiment shows the generation of multiple droplets (a) and (b). Similar to the previous photo, but this time we observed a kind of stabilization and uniform generation of droplets probably due to the second ramal (a) showed in the blue ellipse in the microfluidic device (c).

7. Polymers: From Polyacrylamide, Polydimethylsiloxane (PDMS) to Emulsion polymerization

7.1. Polyacrylamide polymers

Polyacrylamide gel (IUPAC [65], poly(2 -propenamide) or poly(1 -carbamoylethylene), abbreviated as PAM) is a polymer formed by the polymerization of the monomer acrylamide crosslinked to the co-monomer N,N'-methylenebis-acrylamide, commonly called *Bis* Fig. 7.1. This polimerization requires the presence of an initiator, usually ammonium persulfate and a catalyst like N,N,N',N'-tetramethylethylenediamine (TEMED). Polyacrylamide permits the possibility of altering the hardness and crosslinking of the gel by changing the concentrations of acrylamide and *Bis*. Polyacrylamide is frequently used in molecular biology applications, including biochemistry, genetics, and biotechnology [11, 66]. One of the commonest applications in biochemistry is a process called *polyacrylamide* gel *electrophoresis* (PAGE) [66, 67], which involves the separatation of biological macromolecules such as proteins and nucleic acids.

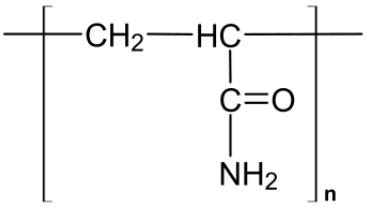

Figure 7.1.: Polyacrylamide. IUPAC name, poly(2 - propenamide). Figure adapted from [68].

7.1.1. PAGE

In gel electrophoresis molecules are presented in their native state or in the denaturant form [1], resulting in the generation of linear pieces of proteins. Then, these unstructured linear chains are charged by *sodium dodecyl sulfate* (SDS) [2] and inserted within the polyacrylamide and run due to the effect of an electric field as depicted in Fig. 7.2. This procedure is called SDS-PAGE. The SDS evenly distributed along the protein provides an homogeneus charge per unit mass resulting in a fractionation size during electrophoresis.

[1] Denaturation can occur when proteins and nucleic acids are subjected to elevated temperatures or extremes indexes of pH, or to high concentrations of salt, organic solvents, urea or other chemichal agents [69].

[2] This creates a charge/mass ratio which is consistent between different proteins.

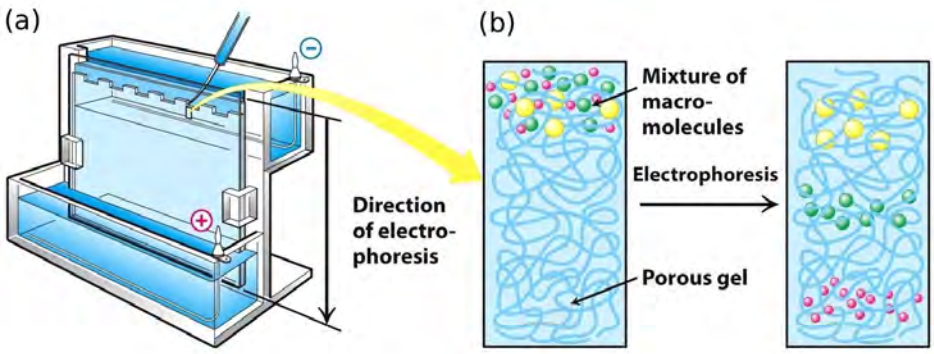

Figure 7.2.: Electrophoresis assay (b) where macromolecules confined inside the wells (b) are forced to move under the effect of an electric field through the polyacrylamide gel (in blue). Figure adapted from Berg, J. M. Biochemistry, Seventh Edition 2012, [67].

In our work we use a slight variation of PAGE protocole for creating our macroemulsions that we explain in the next section.

7.1.2. Chemical ingredients and their roles in polyacrylamide gel formation

Acrylamide (C_3H_5NO**; mW:** 71.08**)**

Its IUPAC name is prop-2-enamide [65]. It is an odorless crystaline solid, soluble in water, ethanol, ether, and chloroform. Acrylamide decomposes in the presence of acids, bases, oxidizing agents, iron, and iron salts [70]. It also decomposes thermally; producing carbon monoxide and oxides of nitrogen, [71] and non-thermally; forming ammonia.

When dissolved in water, in the presence of bisacrylamide, it takes place an interesting aglomeration in molecules. Then they join together spontaneously by head on tail fashion forming linear polymer long strands. The presence of free radical-degenerators promotes in the system the acceleration of such polymerization. This gel formation procedure is widely accepted and used today in experiments of microbiology [72].

Acrylamide is classified as an extremely hazardous substance, concerning cancernogenicity, in the United States and subjected to strict control for producing, storage and uses in significant quantities [73].

Bisacrylamide ($C_7H_{10}N_2O_2$**; mW:** 154.17**)**

Its IUPAC name is N,N'-Methylenebisacrylamide [65]. This linking cross agent allows the formation of polyacrylamide gel. It chemically polymerizes with acrylamide and can be thought as two acrylamide molecules coupled head to head at their non-reactive ends. See Fig. 7.3. In addition, bisacrylamide can crosslink two polyacrylamide resulting in a gel [74].

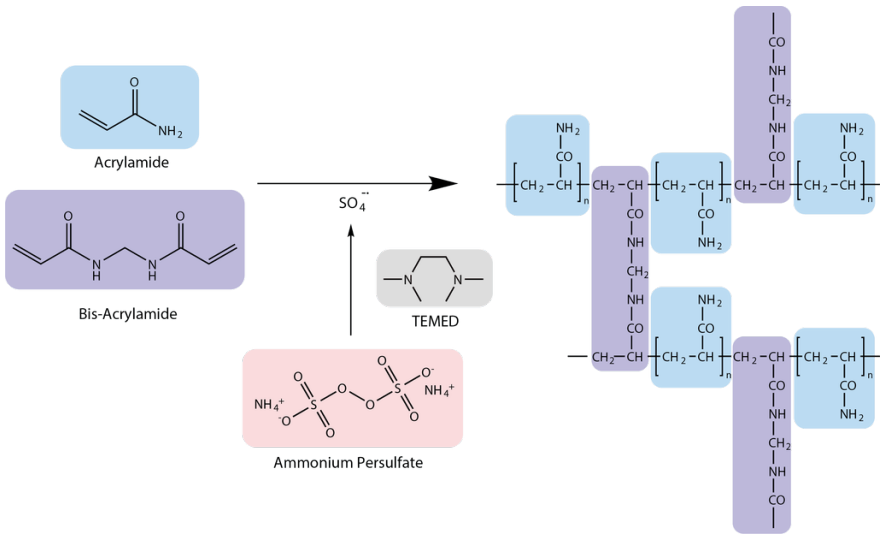

Figure 7.3.: This figure shows the polymerization mechanism catalized by free radicals. TEMED induces the formation of free radicals from unstable ammonium per sulphate (APS). Figure adapted from [75] .

Ammonium persulfate (APS, $N_2H_8S_2O_8$; mW: 228.2)

This unstable molecule provides a source of free radicals. It transfer electrons to the acrylamide/bisacrylamide monomers making them highly chemically reactive towards each other to form the polyacrylamide chain. See Fig. 7.3.

Riboflavine

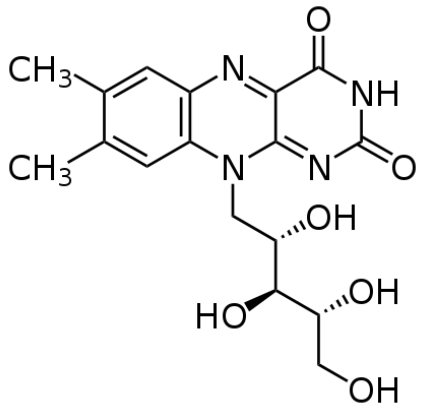

Figure 7.4.: Chemical structure of riboflavin.

It is also known as vitamin B_2, found in some foods as milk, cheese, eggs, legumes, mushrooms and almonds, etc. This vitamin is used as a dietary supplement for riboflavin deficiency and prevent migrains [76]. It has been shown that when UV light is irradiated over riboflavin mixed with blood components, such as red blood cells, blood plasma and platelets, it causes an effective reduction in the harmful ability of pathogens [3] to cause

[3]When riboflavine is exposed to UV light, it permits the release of free radicals. They specifically act on

disease [77, 78, 79]. This technique is suitable for destroying pathogens as viruses, bacteria and parasites.

In polyacrylamide polymerization riboflavin is an interesting alternative source of free radicals, [59].

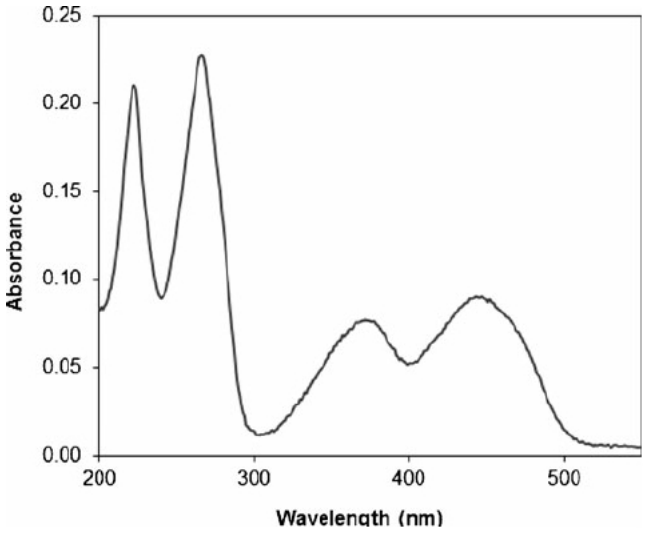

Figure 7.5.: Absorption spectrum of riboflavin aqueous solution (0.08 mg/mL) measured in a demountable quartz cuvette with the path length of 0.5 mm. Riboflavin is characterized by maximum of absorbance in UV range (222, 266, 373 nm) and in visible light range (445 nm) excitations, [80].

Due to its absorbance peaks in the ultraviolet region excitation, see Fig. 7.5, the riboflavin emission is around the green range wavelenght, allowing us in our work to identify the microspheres through their fluorescence [81].

Tetramethylethylenediamine (TEMEDA or TEMED, $(CH_3)_2NCH_2CH_2N(CH_3)_2$)

It is a colourless liquid and its toxic odor is remarkably similar to that of rotting fish [82]. It is highly recommended to work inside a fume hood. TEMED is derived from ethylenediamine by replacementent of the four amine hydrogens with the four methyl groups [83].

TEMED is also employed as a ligand for metal ions to form stable complexes with many metal halides as zinc chloride and cooper(I) iodide. It serves as a bidentate ligand through two sites of the complex. See Fig. 7.6.

the nucleic acids of such pathogens, altering them and consequently damaging.

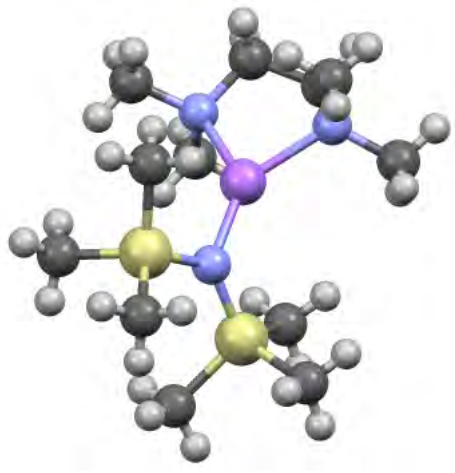

Figure 7.6.: TEMED moving towards the midle of lithium bis(trimethyl)amide. Notice the bidentate function ligand it satisfies. Figure from Henderson et al., [84].

In our work we use polyacrylamide for gel formation of microspheres according to the formula in Tab. 7.1.

Components	Volume (μl)
Acrylamide	188
Bisacrylamide	27
Water	675
APS	100
TEMED	0.5

Table 7.1.: Polyacrylamide formula for emulsion polimerization.

And in the presence of riboflavine, the formula is given by Tab. 7.2.

Components	Volume (μl)
Acrylamide	188
Bisacrylamide	27
Water	275
APS	100
TEMED	0.5
Riboflavin	400

Table 7.2.: Polyacrylamide formula for emulsion polimerization with fluorescence.

7.2. Soft lithography polymers

7.2.1. SU-8 photoresist

It is a light-sensitive epoxy based negative photoresist molecule. Negative means that such exposed areas to UV light are cross-linked and the remainder of the film remains soluble

and can be washed away. The molecule is composed by 8 epoxy groups as it is shown in Fig. 7.7.

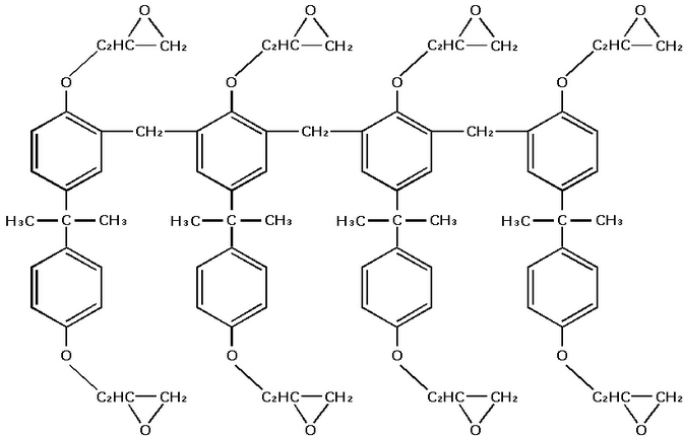

Figure 7.7.: SU-8 molecule.

We mentioned in chapter 4 that the film thickness rangs around less than 1 μm up to above 300 μm [85], depending of the spinning process involving thousands of revolutions per minute.

The maximum wavelength absorption for UV light rounds about 365 nm [4]. Typical solvent to remove the remainder of the film is gamma-butyrolactone, which is a cleaning superglue remover used in some wet aluminum electrolytic capacitors, or cyclopentanone as the primary solvent [5].

SU-8 is a common photoresist used in the fabrication of microfluidic devices and other complex system such microelectromechanical system parts and one of the biocompatible materials known and often used in bio-MEMS (biomedical - or biological - microelectromechanical systems).

The epoxy groups cross-link each other to give the final consistence in the following form: when the areas are exposed to UV light, the cationic hydrogen protonates the epoxy groups allowing the epoxy rings opening. The result is a carbocation which is generally unstable because the carbon does not have eight electrons to satisfy the octet rule. The hydrogens proceed as shown in Fig. 7.8 sequencially attacked by the release of hydrogens in the multiple carbocations.

[4] It is not practical to expose SU-8 to g-line, 365 nm: blue

[5] This means to wich energy of the radiation emitted by the specimen is first transferred as excitation energy

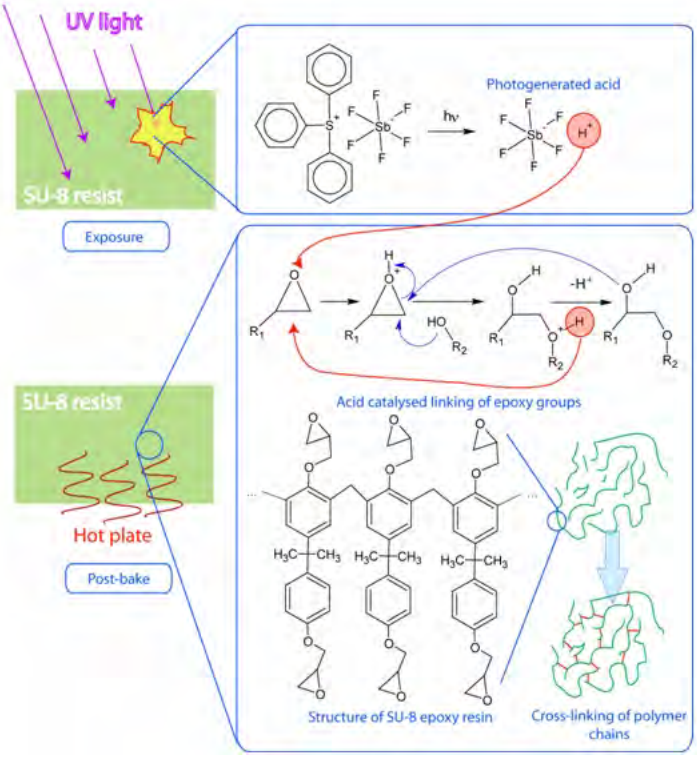

Figure 7.8.: SU-8 polymerization.

The subsequents reactions for polymerization are promoted by baking them in two steps as we mentioned in the chapter of microfabrication.

7.2.2. Polydimethylsiloxane (PDMS) and Sylgard 184

Widely known as PDMS, it belongs to a group of organosilicon compounds that are commonly referred to as silicones. It is widely also known for its unusual rheological or flow properties. This silicon is optically clear, and is generally inert, non-toxic, and non-flammable [86].

About its mechanical properties, PDMS is viscoelastic, this is, it acts like a viscous liquid, similar to honey and an acts as an elastic solid, similar to rubber [87]. PDMS shear modulus varies with preparation conditions, but is typically in the range of 100 kPa and 3 MPa [88].

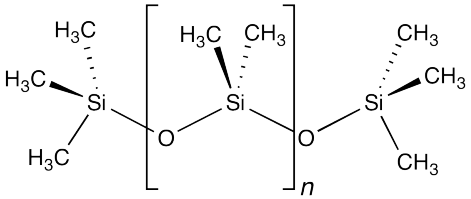

Figure 7.9.: Poly(dimethylsiloxane). Taken from [86].

PDMS is also commonly used as a stamp material for fabrication of microstructures via softlithography, making it the most common material for microfluidic devices [1]. This fabrication process consists of creating an elastic stamp, which enables the transfer of patterns

of the range of few micrometers and nanometers [36, 37]. This feature makes suitable the usage in areas of optic telecommunications or biomedical research [26, 25]. The resolution depends greatly of the photomask used in the process of microfabrication.

Commercially, PDMS is found as Sylgard 184 Silicone Elastomer. It comes in two reactive compositions, base and catalitic agent. In Fig. 7.10 the agent base is composed mainly by (a) and (b) components and the catalitic part by (c). They both are mixed in the proportion weight $10 : 1$, resulting in a viscous consistence full of bubbles as we described in the soft-lithography process in chapter 4.

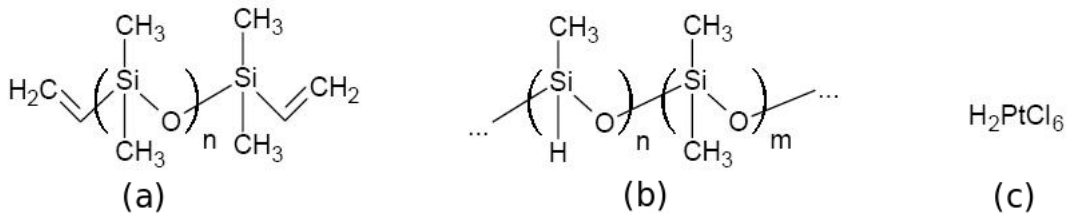

Figure 7.10.: PDMS basic components; (a) and (b) form the base components and the (c) as the catalitic one.

For microfluidic devices fabrication, once PDMS is polymerized, sometimes it is desirable to change the wettability for selling or changing the surface properties. For instance, to achieve a hydrophilicity, the Fig. 7.11 shows how the strong covalent methyl groups are dislocated by the bombardment of an oxygen plasma. Consequently new, but unstable, silanol groups are formed.

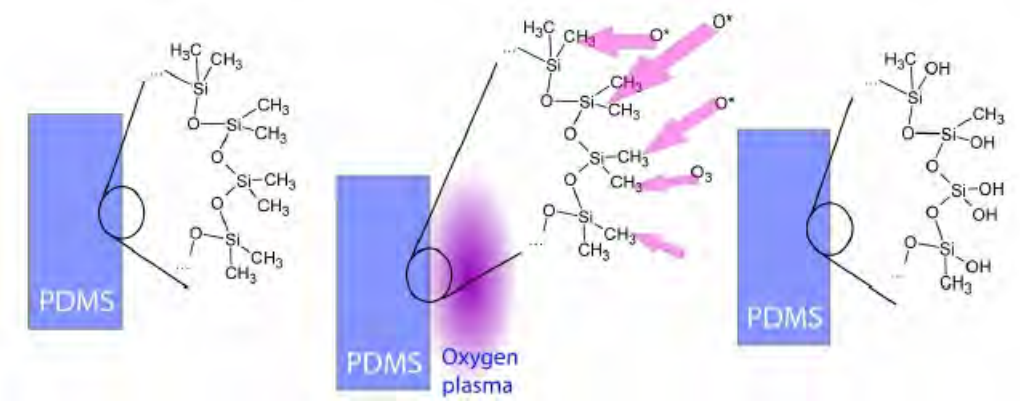

Figure 7.11.: Oxygen bombardment over the PDMS surface full of methyl groups. After this process the surface turns hydrophilic for some minutes. Ideal for changing the surface wettability, and allowing the selling junction surface to surface.

Finally, it is possible to join each other generating new covalent bonds for selling and water releasing. See Fig. 7.12.

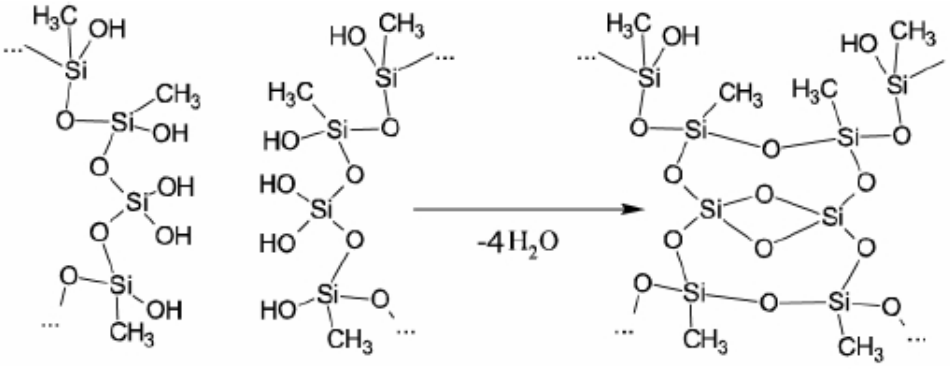

Figure 7.12.: Both PDMS are hydrophilically modified and put in contact to each other. This final leads to release water.

7.3. Methods and Partial Results

We prepared the sample following the next procedure for obtaining polyacrylamide microspheres.

INPUT 1:

- Acrylamide .....188 μL
- Bisacrylamide.....27 μL
- TEMED.....0.5 μL
- APS.....100 μL
- Water.....685 μL

INPUT 2:

- Canola oil 1 mL + PGPR surfactant (4 %).

The control operation mode used for our micropumps was about 100 μL/h of flux for Input 1 and 2. This mode obeys to a 1/32 microstep as in the previous section sec. 6.3.

We obtain the droplets or microspheres, showed in Fig. 7.13, in the microdevice showed in e). Theses spheres were collected for further analysis.

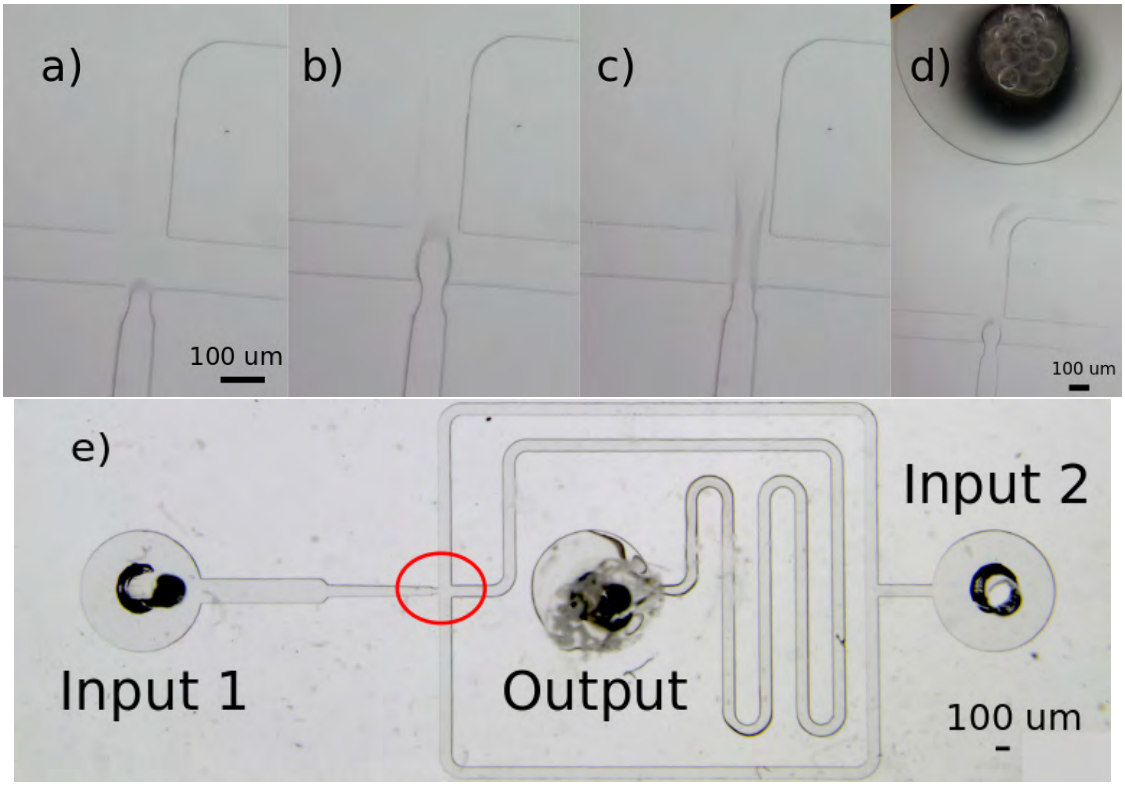

Figure 7.13.: Generation of droplets within a microchannel for simple emulsions. The stages are shown in (a), (b) and (c). The formation of the drop is altered by the presence of polyacrylamide. See figure (c) how the drop formation is dilated, an effect different from Fig. 6.14 where the rupture takes less effort. In (d) is shown all the microspheres collected and conserved for posterior analysis. (e) shows the microfluidic device used.

8. SnappyHexMesh for Computational Fluid Dynamics and Microfluidics

Microfluidics offers several configuration geometries for different setups. Nowadays, the increasing parallelization in computational simulations for many experiments is strong and highly recommended. In this sense, our research group has been constantly committed to develop computational applications.

The interest on solving differential equations via computational methods is increasing dramatically during the past half century. According to [89] more than one third of the researchers population in fluid mechanics has occupied their attention.

This chapter provides an introduction to the computational OpenFoam application, snappyHexMesh, which is a mesh generator for any complex geometry [9]. A general look inside OpenFoam and applications, our research colleage Caio Martins developed during his MSc Project Proposal [90].

8.1. Mesh generation with *snappyHexMesh*

In few words snappyHexMesh is a mesh generator by using an existing mesh and *chisels* into the desired mesh. Some requirements are:

1. A good dictionary located in `system/snappyHexMeshDict`.
2. Good geometrical files. These are:
    a) STL and/or OBJ files with defined surfaces.
    b) eMesh feature edge files, that define feature edges.

snappyHexMesh is quite similar to a mesh sculptor than a mesh generator, because it uses an existing background general mesh and, on the basis of that, it is possible to modify, fit and *sculpt* it. Its main characteristics:

- fine and refine the base mesh;
- adjust the mesh for fitting a particular geometry;
- and, one of the more relevant features, add boundary layers near the boundary patches.

We will see in details these adaptations and limitations in sec. 8.1.5 .

8.1.1. Creation of a Mesh

The utility **blockMesh** is used to create hexaedral structured meshes. The form and distribution of these blocks are controlled by a set of instructions and parameters into the

dictionary `constant/polyMesh/blockMeshDict`. Each block consists of 8 vertices and 12 edges orderly distributed. See Fig. 8.1

- Dictionary file `constant/polyMesh/blockMeshDict`.
- Dictionary file `system/controlDict` .

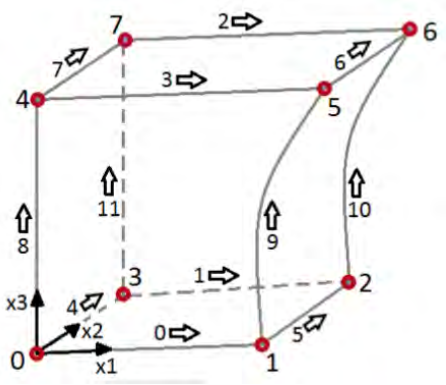

Figure 8.1.: Mesh block with 8 vertices and 12 edges with fixed order. Figure adapted from [91].

8.1.2. snappyHexMesh

This utility was developed by Mattijs Jansens, Eugene de Villiers and Andrew Jackson [91]. Posteriorly, extended and enhances versions with multiple charactetistics include:

- Improve layers and layer specifications methods.
- Generations of internal layers.
- Proximity based refinement.
- Automatic block creation and decomposition
- Mesh wrapping and small leak closure.
- Formats like *standard triangle language* or *STereoLithography* (stl) and Nastran (nas) files are supported for geometry data.
- Among many other extensions...

The requirements are:

- Dictionary file `system/snappyHexMeshDict`.
- The geometry data (stl, nas, or obj) in `constant/triSurface`.
- Hexaedral base mesh (decomposed if running in parallel).
- Dictionary file `system/decomposeParDict` for parallel runs.
- All system dictionaries (eg. `controlDict`, `fvSchemes`, `fvSolutions`.

8.1.3. snappyHexMesh Metodology

Step 1

Creating a base mesh using the utility **blockMesh**. The cells have approximately a unity for an Aspect Ratio for optimum behaviour. See Fig. 8.2.

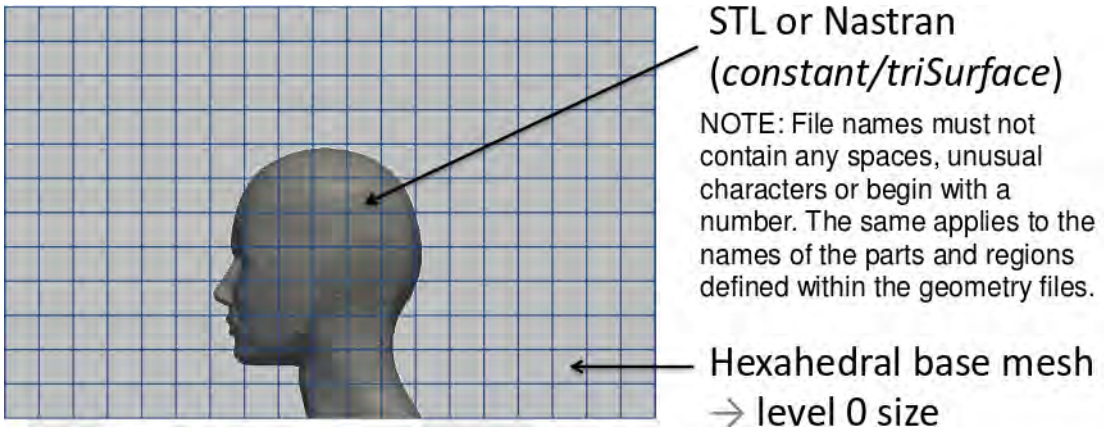

Figure 8.2.: Creating a blockMesh base. Picture adapted from [91].

Step 2

Then *refining* the base mesh and *removing* the unusual cells. As a result a castelated mesh geometry is originated. See Fig. 8.3. Into such figure is possible to distinguish big and small cubes. The bigger "cubes", which in two dimensions is represented by a square, is denominated as Level 0. The Level 1 is conformed by a cube of size a quarter parte of the Level 1, and so on, the cubes Level 2 and 3 follow the same iteration.

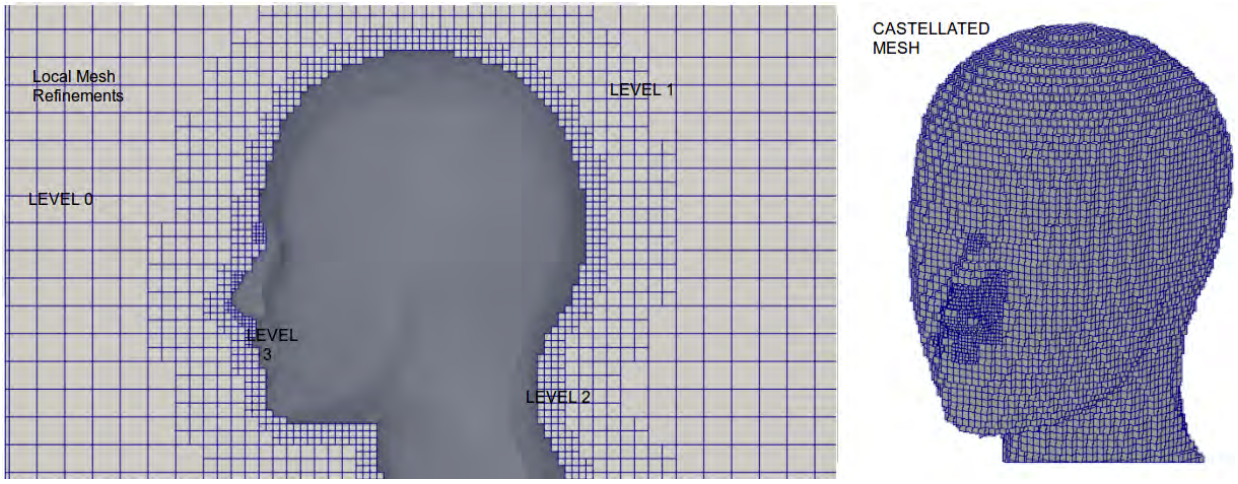

Figure 8.3.: Local Mesh Refinements: Refining locally the base mesh and removing unusual cells. On the left, the different denominations for cubes. On the right, the generated castellated mesh. Picture adapted from [91].

Step 3

Once the irrelevant blocks are extracted, it should snap those ones which are in contact with the surface. See Fig. 8.4. Finally, additional layers over the border will increase the quality of the mesh base.

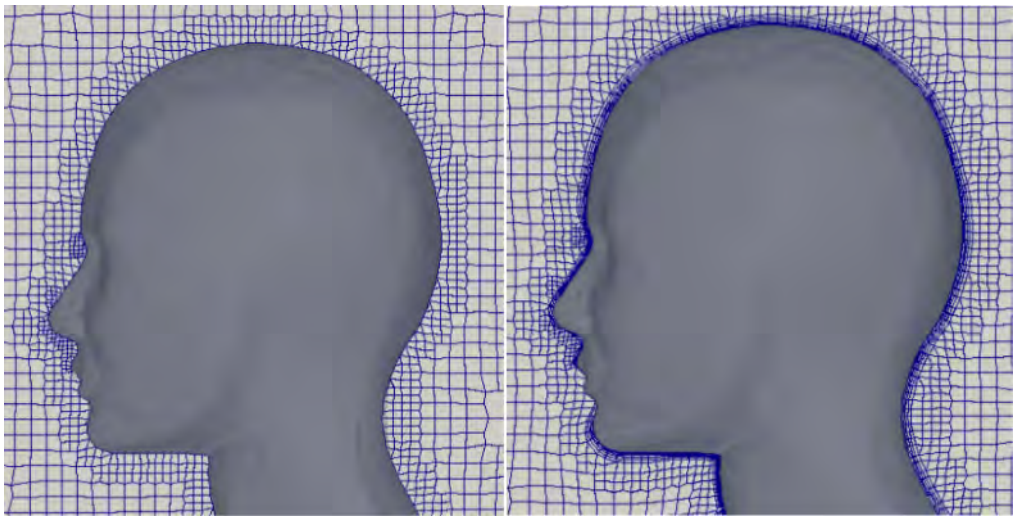

Figure 8.4.: Snapping and addition of layers at the boundary regions. Picture adapted from [91].

In the next section we describe briefly the main directories and some sub-directories of the snappyHexMesh dictionary, `snappyHexMeshDict`, and explain how the previous processes are automatically completed.

8.1.4. snappyHexMeshDict

This file consists of five main sections or sub-directories with specific tasks for each process:

- castellatedMesh: to activate on creation of the castellated mesh.
- snap: to activate on surface snapping controls.
- addLayers: to activate the surface layer insertion.
- geometry: which introduces the geometry entities for meshing.
- castellatedMeshControls: to introduce features refinements.
- snapControls: to control mesh surface snapping.
- addLayersControls: to control and introduce layer mesh growth
- meshQualityControls: to control of the mesh quality metrics.

8.1.5. snappyHexMeshDict specifications

Here we describe details of some important sub-directories.

`castellatedMeshControls`: The splitting process includes the next main entries:

- `locationInMesh`: Describe the position vector that indicates the volume region to be meshed.
- `maxGlobalCells`: cell limit generated during refinement before removal.
- `maxLocalCells`: maximum number of cells per processor during refinement.
- `nCellsBetweenLevels`: number of buffer layers of cells between succesive levels of refinement.
- `features`: list of features for refinement.
- `refinementSurfaces`: dictionary of surfaces for refinement.
- `refinementRegions`: dictionary of regions for refinement.

The `features` subdirectory contains a name of an `edgeMesh` file and the `level` of refinement:

```
features
(
    {
        file "features.eMesh";  //file containing edge mesh
        level 2;                //level of refinement
    }
);
```

The `edgeMesh` file contains the features to be extracted from the tri-surface file using the utility `surfaceFeatureExtract`, following the instructions in the `surfaceExtractDict` configuration file.

The `refinementSurfaces` specifies the minimum and maximum level of refinement in the form (<`minimum`><`maximum`>). The minimum level is applied to cells in the intersection surfaces. The second level, specifically those multiple intersections that makes an angle bigger than the defined `resolveFeatureAngle`.

```
refinementSurfaces
{
    main
    {
        // Surface-wise min and max refinement level
        level (2 2);
    }
}

resolveFeatureAngle 30;
```

Cell removal

Once the surface splitting is completed, we have to consider two criteria for cells removing, or cell retaining. 1) The region in wich cells are retained are identified by a location vector, specified by the`locationInMesh`. 2) Cells are retained through the border if, roughly speaking, 50% or more of their volume lies between the region. See Fig. 8.5.

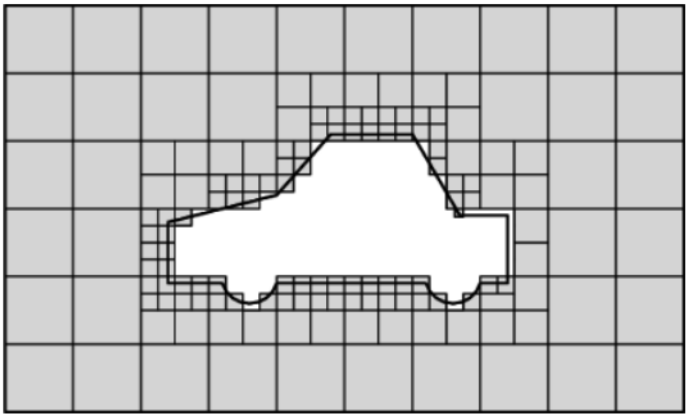

Figure 8.5.: Cell removal in `snappyHexMesh`. Picture adapted from [9].

Cell splitting in specified regions

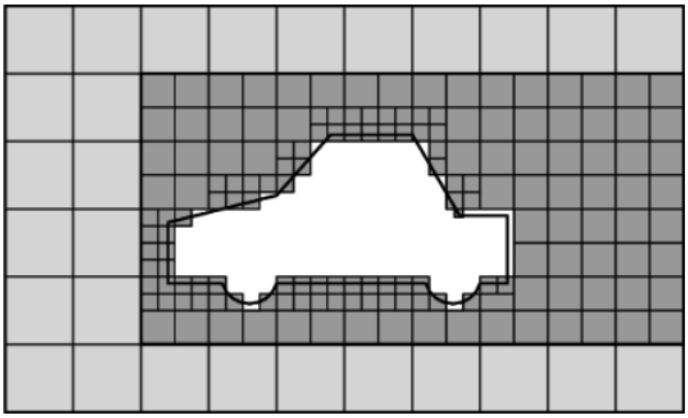

Figure 8.6.: Cell splitting in different regions. Picture adapted from [9].

For cells belonging to one or more specified volume regions as is shown in Fig. 8.6, the `refinementRegions` sub-dictionary contains entries for refinement of such volumes specified in the `geometry` sub-dictionary. These can be:

- `inside`; which refines inside the volume regions
- outside; refines outside the volume regions
- distance; refines according to the distance from the surface. It is possible to refine at different levels with the format (<`distance`><`level`>).

```
refinementRegions
{
    refinementBox
    {
        mode inside;
        levels ((1E15 4));
    }

    sphere.stl
    {                                   //refinement level 5 within 1.0 m
        mode distance;                  //refinement level 3 within 2.0 m
        levels ((1.0 5) (2.0 3));       //levels must be ordered nearest first
    }
}
```

In the case of `inside` and `outside`, the distance is not required but it is recommended to specify.

Snapping to surfaces

The next step requires to move the vertex points towards the border. For a rough example see Fig. 8.7. But it is not so simple, in an orderly way the process involves to:

1. displace the vertices in the castellated boundary towards the surface;
2. make a relaxation of the internal mesh with the previous modifications;
3. find the vertices that violates the mesh quality, this is: *check* the mesh;
4. reduce the displacement between the neighbour vertices and repeat the process from 1 to 3.

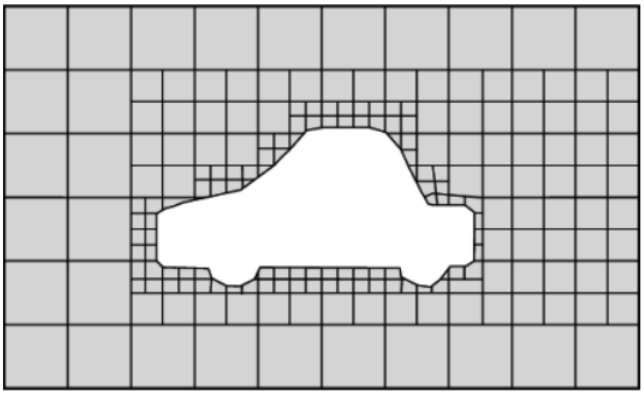

Figure 8.7.: Surface snapping using `snappyHexMesh`. Note how the vertex points of the border has been altered compared to Fig. 8.6. Picture adapted from [9].

The short algorithm exposed above is developed following the next settings in the `snapControls` sub-dictionary in`snappyHexMeshDict`.

- `nSmoothPatch`: number of smooth patch iterations before finding the correspondence to surface. It is recommended to consider 3.
- `tolerance`: ratio of distance for points to be attracted by surface feature point or edge, to local maximum edge length. Typically 2.0 .

- `nSolveter`: number of mesh displacement relaxation iterations. It is recommended $30 - 100$.
- `nRelaxIter`: maximum number of snapping relaxation iterations. It is recommended 5.

Mesh layers

After the snapping process, some cells next to the border seems to be irregular, in this case optionally, it is possible to introduce additional layers of hexaedral cells aligned to the boundary surface as it is shown in Fig. 8.8.

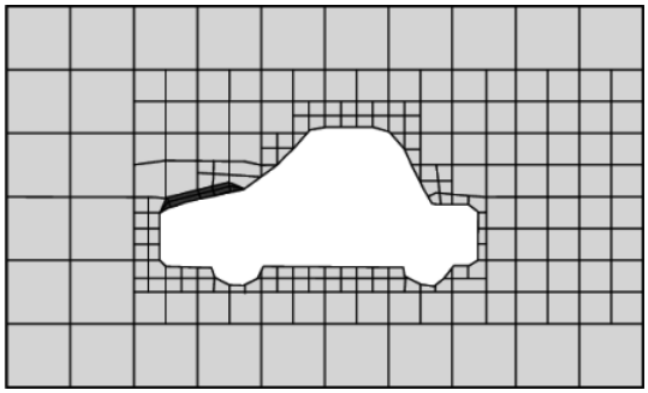

Figure 8.8.: Layer addition in `snappyHexMesh`. Picture adapted from [9].

This insertion of layers deals with shrinking the existing mesh, broadly as follows:

1. back from the surface, it is projected a thickness in the direction normal to the surface;
2. with the latest projected boundary it is solved the relaxation internal mesh;
3. check the validation criteria. Otherwise the projected thickness is reduced and return to step 2. If this validation does not still satisfy the criteria, the layers wont be included.
4. If validation is satisfied, inserted the mesh layers.
5. check the mesh again; if checks fail, layers are removed and return to step 2.

Finally, in adding the mesh layers, just 4 parameters to modify in the `addLayersControls` sub-dictionary:

- `expansionRatio`: expansion ratio factor for successive layers.
- `thickness`: total thickness of all layers of cells.
- `firstLayerThickness`: thickness of the layer nearest the wall.
- `finalLayerThickness`: thickness of the layer furthest from the wall.

From these 4 parameters, it is recommended to specify only 2, because there are risk of being over-specified.

8.2. Methods and Partial Results

For an approximated droplet generation, we use the properties of the fluid introduced in the OpenFoam utilities. At the moment of the development of this project we have found an approximated fluid that promotes the generation of droplets according to our experiments in sec. 6.3 and sec. 7.3. In Fig. 8.9 we see that one of the fluid parameter values is for water and the other is an unknown fluid of kinematic viscosity $1.48\text{x}10^{-5}\,\text{m}^2/\text{s}$ and its density around $500\,\text{Kg}/\text{m}^3$.

```
dimensions      [0 1 -1 0 0 0 0];

internalField   uniform (1 1 0);

boundaryField
{
    inlet_fluid 2
    {
        type            fixedValue;
        value           uniform (0.1 0 0);

    }

    inlet_water
    {
        type            fixedValue;
        value           uniform (0 0.05 0);
    }
```

```
phase1 //water
{
    transportModel  Newtonian;
    nu              nu [ 0 2 -1 0 0 0 0 ] 1e-06;
    rho             rho [ 1 -3 0 0 0 0 0 ] 1000;
}

phase2 //fluid 2
{
    transportModel  Newtonian;
    nu              nu [ 0 2 -1 0 0 0 0 ] 1.48e-05;
    rho             rho [ 1 -3 0 0 0 0 0 ] 500;
}
```

Figure 8.9.: On the left are shown the inlet velocities for water and for "fluid 2". Water velocity is about $0.05\,\text{m}/\text{s}$ and $0.1\,\text{m}/\text{s}$ for the other. Note that this second fluid is not oil, but produce very kindly our droplets according to our experiments in sec. 6.3 and sec. 7.3. On the right are introduced the transport parameters of the fluids. Note that for water the kinematic viscosity introduced is $1.0\text{x}10^{-6}\,\text{m}^2/\text{s}$ and its density about $1000\,\text{Kg}/\text{m}^3$.

Note here that in our simulation, shown in Fig. 8.10, we have used the known method volume of fluid (VOF) [92], to characterized the two phases inside the channels. Water fluid is represented by red and the other fluid by blue.

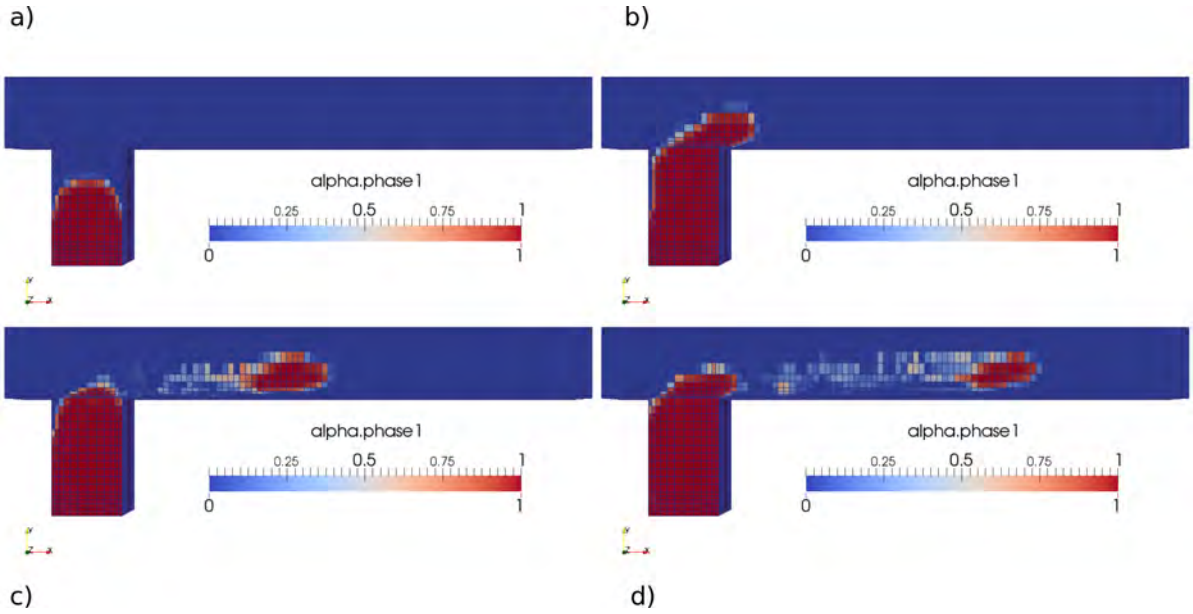

Figure 8.10.: Computational simulation of droplets generated by insering two kind of fluids. In a) we see how the two phases of fluids blue and red. Noting that the angle of contact for the red fluid is bigger than 90 °. In (b) we see the ramal and the competitions of surface tension forces, promoting the rupture (c) of a plug of red fluid. In (d) it is shown the continuous creation of droplets. This simulation was developed in collaboration with Francisco Tovar from the RMIT in Melbourne - Australia and the prof. Murilo Pereira de Almeida from the University of Ceará.

9. Final Considerations

9.1. Conclusions

- The electromechanical infusion pumps, the MiniDrop 1.0, have been entirely developed in our laboratory. This system is now prepared for multiple purpose applications.
- We managed to control two infusion pumps using just one controller. This attribute makes the MiniDrop 1.0 suitable for working various inputs fluxes spontaneuously.
- We managed to control the microsteps of the stepper motors and consequently to obtain a flux precision less than 10 nL using the 1/32 microstepper.
- We get partially polyacrylamide spheres which will be used for a complex fluid like blood.
- We could generate the formation of droplets using the volume of fluid method (VOF). Additionaly, we have considered the suitable contact angle between the fluid and the inner wall.

9.2. Difficulties

- During the development of the instrumentation pump project, the torque has been a constant difficulty to be solved furtherly. Each microstep is being slightly irregular, from previous and subsequent steps, sufficiently to cause considerable alterations at the nanoliter range.
- The lack of measures has difficulted the validation of our control of flow rates and volumes. An immediate achievement to be reached in brief is the implementation of a tracking velocimeter, based on images treatment, and using the open source software Processing [93]. A microPIV being implemented in our laboratory. See Fig. 9.1.
- Our results simulated in OpenFoam need to be solved to generate a mesh similar to our experiments geometry. We also need to work in the implementation of the properties of the fluid 2.

9.3. Further prospects

Additionaly, we performed microelectrodes combined with microfluidic devices. It is not the focus of this research but we expect to use in the near future. Fig. 9.2 shows a channel passing between gold electrodes at both sides. If we imagine an ionic solution flow passing trough the channel, an electric field could deviate the ions in it for left or right.

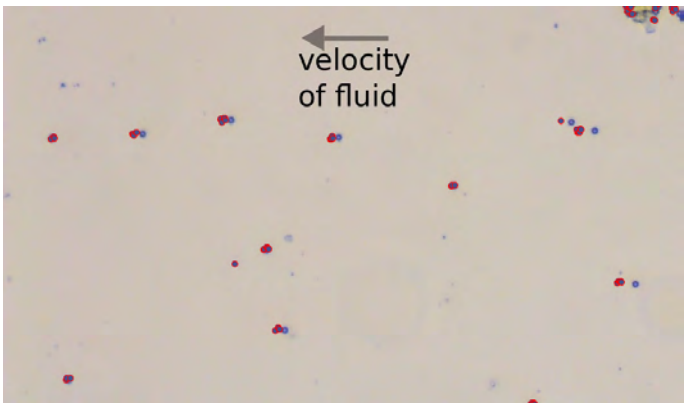

Figure 9.1.: Tracking particles by using Processing [93], which is a free and open source software to teach programming fundamentals within a visual context .

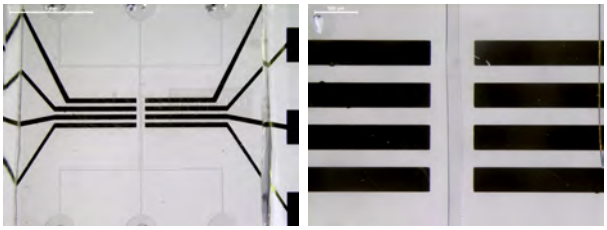

Figure 9.2.: Microelectrodes performed via sputtering deposition over a treated glass. The microfluidic device is then selled by such glass containing the arrange showed. The left picture is a zoom in of the right.

The Fig. 9.3 shows a more complex arrange of electrodes for neurons culture. In the left side, the dispositive is covered almost completely by SU-8 to isolate electrodes, except the central area which is exposed for cell culture. It is expected to receive and send signals, make stimulus, interpret a series of data, etc.

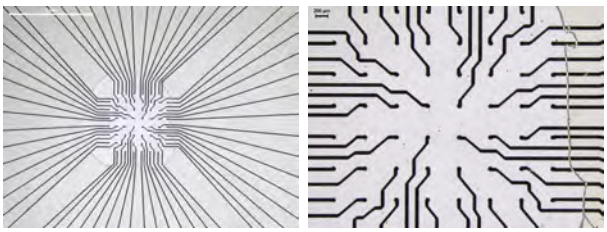

Figure 9.3.: Microelectrodes performed by the same process of the previous microelectrodes. This microdevice is intended for working in neurons stimulation signaling. The left picture is a zoom in of the right.

A. Vector Identities

A.1. Vector and Tensor Identities

Consider the next Levi-Civita identity

$$\epsilon_{ijk}\epsilon_{lmn} = \delta_{il}\delta_{jm}\delta_{kn} + \delta_{im}\delta_{jn}\delta_{kl} + \delta_{in}\delta_{jl}\delta_{km} - \delta_{il}\delta_{jn}\delta_{km} - \delta_{in}\delta_{jm}\delta_{kl} - \delta_{im}\delta_{jl}\delta_{kn} \tag{A.1}$$

In the simpler form in Physics calculus it is useful the next identity many times

$$\epsilon_{ijk}\epsilon_{lmk} = \delta_{il}\delta_{jm} - \delta_{im}\delta_{jl} \tag{A.2}$$

In ideal fluids we use sometimes the next application for Euler equation for the vector $\boldsymbol{v} \times (\boldsymbol{\nabla} \times \boldsymbol{v})$. Evaluating in the tensorial form,

$$\Big[\boldsymbol{v} \times (\boldsymbol{\nabla} \times \boldsymbol{v})\Big]_i = \epsilon_{ijk}\epsilon_{klm}v_j\partial_l v_m \tag{A.3}$$

$$= v_m\partial_i v_m - v_l\partial_l v_i \tag{A.4}$$

by noting that $v_m\partial_i v_m = \frac{1}{2}\partial_i v_m^2$ then

$$\Big[\boldsymbol{v} \times (\boldsymbol{\nabla} \times \boldsymbol{v})\Big]_i = \frac{1}{2}\partial_i v_m^2 - v_l\partial_l v_i \tag{A.5}$$

or in vectorial notation,

$$\boldsymbol{v} \times (\boldsymbol{\nabla} \times \boldsymbol{v}) = \frac{1}{2}\boldsymbol{\nabla} v^2 - (\boldsymbol{v} \cdot \boldsymbol{\nabla})\boldsymbol{v} \tag{A.6}$$

B. Viscous fluids

B.1. The equations of motion of a viscous fluid. A general approach.

From Equation B.6, utilizing Gauss's theorem it is expressed by,

$$(\partial_t \rho)\upsilon_i + \rho \partial_t \upsilon_i = \partial_j \Big[- \Pi_{ij} + \sigma'_{ij} \Big] + \rho g_i + \rho_{\text{el}} E_i \qquad , \tag{B.1}$$

$$(\partial_t \rho)\upsilon_i + \rho \partial_t \upsilon_i = -\partial_j \Big(\rho \upsilon_i \upsilon_j \Big) - \partial_j \Big(p \delta_{ij} \Big) + \partial_j (\sigma'_{ij}) + \rho g_i + \rho_{\text{el}} E_i \qquad , \tag{B.2}$$

by combining the pressure and viscous stress tensor σ' into a full stress tensor σ, taking the same idea of Equation2.30 about the prime indicatives,

$$(\partial_t \rho)\upsilon_i + \rho \partial_t \upsilon_i = -\partial_j \Big(\rho \upsilon_i \upsilon_j \Big) + \partial_j (\sigma_{ij}) + \rho g_i + \rho_{\text{el}} E_i \qquad . \tag{B.3}$$

Deriving the first term of the second equality, $-\partial_j \Big(\rho \upsilon_j \upsilon_i \Big) = -\partial_j \Big(\rho \upsilon_j \Big) \upsilon_i - \rho \upsilon_j \partial_j \Big(\upsilon_i \Big)$, and using the continuity relation, $-\partial_j \Big(\rho \upsilon_j \Big) = \partial_t \rho$, we arrive to:

$$\rho \partial_t \upsilon_i + \rho \upsilon_j \partial_j \Big(\upsilon_i \Big) = \partial_j \sigma_{ij} + \rho g_i + \rho_{\text{el}} E_i \qquad , \tag{B.4}$$

where the left hand may be understood as the inertial force densties, and the right one as the intrinsic or applied force densities. For Newtonian fluids the viscosity coefficients η and ζ can be considered as constants,

$$\partial_j \sigma_{ij} = \partial_j (-p \delta_{ij}) + \partial_j \sigma'_{ij} = -\partial_i p + \eta \partial_j \partial_j \upsilon_i + \beta \eta \partial_i (\partial_j \upsilon_j) \qquad , \tag{B.5}$$

which subtituted in B.4 becomes the *Navier-Stokes* equation,

$$\rho \partial_t \upsilon_i + \rho \upsilon_j \partial_j \Big(\upsilon_i \Big) = -\partial_i p + \eta \partial_j^2 \upsilon_i + \beta \eta \partial_i (\partial_j \upsilon_j) + \rho g_i + \rho_{\text{el}} E_i \qquad , \tag{B.6}$$

$$\rho\Big[\partial_t \boldsymbol{\upsilon} + (\boldsymbol{\upsilon}\cdot\boldsymbol{\nabla})\boldsymbol{\upsilon}\Big] = -\boldsymbol{\nabla}p + \eta\nabla^2\boldsymbol{\upsilon} + \beta\eta\boldsymbol{\nabla}(\boldsymbol{\nabla}\cdot\boldsymbol{\upsilon}) + \rho\mathbf{g} + \rho_{\text{el}}\mathbf{E} \qquad . \tag{B.7}$$

In microfluidics is frequently made the approximation for an incompressible fluid,

$$\rho\partial_t\upsilon_i + \rho\upsilon_j\partial_j\Big(\upsilon_i\Big) = -\partial_i p + \eta\partial_j^2\upsilon_i + \rho g_i + \rho_{\text{el}}E_i \qquad , \tag{B.8}$$

$$\rho\Big[\partial_t \boldsymbol{\upsilon} + (\boldsymbol{\upsilon}\cdot\boldsymbol{\nabla})\boldsymbol{\upsilon}\Big] = -\boldsymbol{\nabla}p + \eta\nabla^2\boldsymbol{\upsilon} + \rho\mathbf{g} + \rho_{\text{el}}\mathbf{E} \qquad . \tag{B.9}$$

B.1.1. Energy flux and heat-transfer equation

The last governing equation of fluid dynamics is related to energy. It is natural to work with thermodynamic quantities per unit mass, which are directly related to the molecules present in the fluid. In this sense, let us express the first law of thermodynamics per unit mass,

$$\mathrm{d}\epsilon = T\mathrm{d}s - p\mathrm{d}(\frac{1}{\rho}) = T\mathrm{d}s + \frac{p}{\rho^2}\mathrm{d}\rho \qquad , \tag{B.10}$$

In analogy with the momentum flux changes in section sec. 2.1.3, we calculate the rate of change $\partial_t E(\Omega\, t)$ as:

$$\partial_t E(\Omega\, t) = \partial_t \int_\Omega \mathrm{d}\mathbf{r}\Big[\frac{1}{2}\rho\upsilon^2 + \rho\epsilon\Big] \qquad , \tag{B.11}$$

and in analogy to the rage of change of the momentum, we have a convection energy term, a change due to pressure and friction and that due to thermal gradients at the surface by heat conduction. In microfluidics, for simplicity we are going to disregard the term due to heat sources and sinks inside Ω:

$$\partial_t E(\Omega,\, t) = \partial_t E^{\text{conv}}(\Omega,\, t) + \partial_t E^{\text{pres}}(\Omega,\, t) + \partial_t E^{\text{visc}}(\Omega,\, t) + \partial_t E^{\text{conduct}}(\Omega,\, t) \qquad . \tag{B.12}$$

In analogy with the mass current density $\mathbf{J}$, we can construct an energy flux density $\mathbf{J}_\epsilon = (\frac{1}{2}\rho\upsilon^2 + \rho\epsilon)\boldsymbol{\upsilon}$, which is the convection of the energy out of the region,

$$\partial_t E^{\text{conv}}(\Omega\, t) = -\int_{\partial\Omega} \mathrm{d}a\, \mathbf{n}\cdot\mathbf{J}_\epsilon = -\int_{\partial\Omega} \mathrm{d}a\, n_j v_j\Big[\frac{1}{2}\rho\upsilon^2 + \rho\epsilon\Big] \qquad . \tag{B.13}$$

The minus sign is because the convention of the surface normal points outwards. The power transferred into the region due to the stress forces over the surface is given by the product $\boldsymbol{\upsilon} \cdot (\sigma \mathrm{n} \mathrm{d}a)$,

$$\partial_t E^{\mathrm{pres}}(\Omega\, t) + \partial_t E^{\mathrm{visc}}(\Omega\, t) = \int_\Omega \mathrm{d}a\, \upsilon_k \sigma_{kj} n_j = \int_\Omega \mathrm{d}a\, n_j [-p\delta_{ik} + \sigma'_{jk}]\upsilon_k \qquad , \tag{B.14}$$

where we have used the symmetry of the tensor $\sigma'_{kj} = \sigma'_{jk}$.

The thermal flux density is defined as the energy rate per unit area and unit time given in $\mathrm{Jm}^{-2}\mathrm{s}^{-1}$, which can be expanded in derivatives of temperature. Taking acount only small temperatures variations, we consider only the first derivative which is the known Fourier's law of heat for an isotropic medium,

$$\mathbf{J}_\epsilon = -\kappa \boldsymbol{\nabla} T \qquad , \tag{B.15}$$

where κ is called the thermal conductivity of the fluid with units $\mathrm{Wm}^{-}1\mathrm{K}^{-}1$. For water at $20\,^{\mathrm{o}}\mathrm{C}$ is

$$\kappa_{\mathrm{water}}(20\,^{\mathrm{o}}\mathrm{C}) = 0.597\,\mathrm{Wm}^{-1}\mathrm{K}^{-1} \qquad . \tag{B.16}$$

The rate of energy due to heat conduction is expressed in terms of heat flux density by using the Fourier's law,

$$\partial_t E^{\mathrm{conduct}}(\Omega\, t) = -\int_{\partial\Omega} \mathrm{d}a\, \mathbf{n} \cdot \mathbf{J}_{\mathrm{heat}} = \int_{\partial\Omega} \mathrm{d}a\, n_j (\kappa \partial_j T) \qquad . \tag{B.17}$$

Let us see another interesting version of the third using the Gauss's theorem for rewritting integrals into the volume,

$$\partial_t \Big(\frac{1}{2}\rho\upsilon^2 + \rho\epsilon \Big) = -\boldsymbol{\nabla} \cdot \Big([\frac{1}{2}\rho\upsilon^2 + \rho\epsilon + p]\boldsymbol{\upsilon} - \sigma' \cdot \boldsymbol{\upsilon} - \kappa \boldsymbol{\nabla} T \Big) \qquad , \tag{B.18}$$

or in the index notation,

$$\partial_t \Big(\frac{1}{2}\rho\upsilon^2 + \rho\epsilon \Big) = -\partial_j \Big([\frac{1}{2}\rho\upsilon^2 + \rho\epsilon + p]\upsilon_j - \sigma'_{jk}\upsilon_k - \kappa \partial_j T \Big) \qquad . \tag{B.19}$$

The total flux energy density $\mathbf{J}_{\mathrm{erg}}$ can be expressed as the vector:

$$\mathbf{J}_{\mathrm{erg}} = [\frac{1}{2}\rho\upsilon^2 + \rho\epsilon + p]\boldsymbol{\upsilon} - \sigma' \cdot \boldsymbol{\upsilon} - \kappa \boldsymbol{\nabla} T \qquad . \tag{B.20}$$

As we mentioned initially in this section, it is customary to represents energy equation involving thermodynamical quantities as entropy s per unit mass times ρT. Let us perform the time derivative on the left-hand side,

$$\partial_t\Big(\frac{1}{2}\rho\upsilon^2+\rho\epsilon\Big)=(\frac{1}{2}\upsilon^2+\epsilon)\partial_t\rho+\rho\upsilon_j\partial_t\upsilon_j+\rho\partial_t\epsilon \qquad , \tag{B.21}$$

and by using the continuity equation, $\partial_t\rho=-\partial_j(\rho\upsilon_j)$, and the general equation for a viscous fluid, previous to Navier-Stokes equation, $\rho\upsilon_j\partial_t\upsilon_j=\upsilon_j\partial_i\sigma_{ij}-\rho\upsilon_j\upsilon_i\partial_i\upsilon_j$

$$\partial_t\Big(\frac{1}{2}\rho\upsilon^2+\rho\epsilon\Big)=(\frac{1}{2}\upsilon^2+\epsilon)\Big[-\partial_j(\rho\upsilon_j)\Big]+\Big[\upsilon_j\partial_i\sigma_{ij}-\rho\upsilon_j\upsilon_i\partial_i\upsilon_j\Big]+\rho\partial_t\epsilon \qquad , \tag{B.22}$$

and bringing the entropy s into play for the energy,

$$\rho\partial_t\epsilon=\rho T\partial_t s+\frac{p}{\rho}\partial_t\rho=\rho T\partial_t s-\frac{p}{\rho}\partial_j(\rho\upsilon_j) \qquad , \tag{B.23}$$

and for the pressure,

$$\mathrm{d}(\epsilon+p/\rho)=T\mathrm{d}s+\frac{1}{\rho}\mathrm{d}p \qquad , \tag{B.24}$$

from which follows,

$$-\upsilon_j\partial_j p=-\rho\upsilon_j\partial_j(\epsilon+\frac{p}{\rho})+\rho T\upsilon_j\partial_j s \qquad , \tag{B.25}$$

and by using Equations B.23 and B.25 into Equation B.21:

$$\partial_t\Big(\frac{1}{2}\rho\upsilon^2+\rho\epsilon\Big)=(\frac{1}{2}\upsilon^2+\epsilon)\Big[-\partial_j(\rho\upsilon_j)\Big]+\Big[-\rho\upsilon_j\partial_j(\epsilon+\frac{p}{\rho})+\rho T\upsilon_j\partial_j s+\upsilon_j\partial_i\sigma'_{ij}-\rho\upsilon_i\partial_i(\frac{\upsilon^2}{2})\Big]+\rho T\partial_t s-\frac{p}{\rho}\partial_j(\rho\upsilon_j) \tag{B.26}$$

to finally arrive to:

$$\partial_t\Big(\frac{1}{2}\rho\upsilon^2+\rho\epsilon\Big)=-\partial_j\Big[(\frac{1}{2}\rho\upsilon^2+\rho\epsilon+p)\upsilon_j\Big]+\rho T\Big[\upsilon_j\partial_j s+\partial_t s\Big]+\upsilon_i\partial_j\sigma'_{ij} \qquad . \tag{B.27}$$

Equaling this expression with Equation B.19 we can deduce that

$$\rho T\Big[\partial_t s + \upsilon_j \partial_j s\Big] = \sigma'_{jk}\partial_k \upsilon_j + \partial_j(\kappa \partial_j T) \qquad , \tag{B.28}$$

or in vector notation

$$\rho T\Big[\partial_t s + (\boldsymbol{\upsilon}\cdot\boldsymbol{\nabla})s\Big] = \sigma' : \boldsymbol{\nabla}\upsilon + \boldsymbol{\nabla}\cdot(\kappa\boldsymbol{\nabla}T) \qquad , \tag{B.29}$$

or in simpler form,

$$\rho T\frac{\mathrm{d}s}{\mathrm{d}t} = \sigma' : \boldsymbol{\nabla}\upsilon + \boldsymbol{\nabla}\cdot(\kappa\boldsymbol{\nabla}T) \qquad , \mathrm{d}ta \tag{B.30}$$

where we have used the double dot product defined as:

$$T : S \equiv \sum_{i,j} T_{ij}S_{ji} = T_{ij}S_{ji} = \mathrm{Tr}(TS) \qquad . \tag{B.31}$$

The Equation B.29 is the second version version of the third governing equation of the fluid dynamic system, also called the *general heat-transfer equation*. Its left hand represents the total derivative of the entropy per unit mass and the right hand represents that due to sources for heat gain; this is viscous friction and thermal conduction. Note the difference with the Equation 2.15, without these sources, we have an ideal fluid.

In microfluidics where we have low velocities compared to speed of sound, we may neglect pressure variations. In consequence, for the entropy $s = s(T, p)$ with practically p constant we have,

$$\partial_t s = (\partial_T s)_p \partial_t T \qquad \text{and} \qquad \boldsymbol{\nabla} s = (\partial_t s)_p \boldsymbol{\nabla} T \qquad . \tag{B.32}$$

Considering the well known fact that $T(\partial_T s)_p = c_p$, where c_p is the specific heat at constant pressure, our general het-transfer equation is expressed as:

$$\rho c_p\Big[\partial_t T + (\boldsymbol{\upsilon}\cdot\boldsymbol{\nabla})T\Big] = \boldsymbol{\nabla}\cdot(\kappa\boldsymbol{\nabla}T) + \sigma' : \boldsymbol{\nabla}\upsilon \qquad , \tag{B.33}$$

In microfluidics we may consider a next assumption too; neglecting the temperature dependence of ρ, η, κ and c_p, and take them as constants.

C. Liquid film flow on an inclined plane

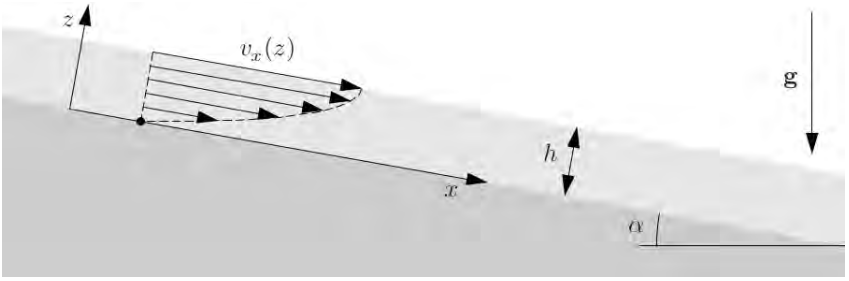

Figure C.1.: An infinite liquid film (light gray) flowing over an inclined plane (dark gray). Note that the gravitational field has an inclination angle α with respect to the plane. Take a look on the resulting velocity profile of the liquid film.

Suppose we have a liquid film flowing down an infinitely wide inclined plane. See Fig. C.1. Notice the inclined plane has an inclination angle α and consequently the acceleration field can be decomposed into two components, parallel g_x and normal g_z to the plane. Only the x component $g_x = g \sin \alpha$ accelerates the film down, i.e. accelerates every particle of the flow, until the velocity reaches a maximum value that viscous forces compensate g_x. Since there is an invariance in the x-y plane, and since the velocity depends only on z, we conclude that the fluid is moving in the x direction only. That is,

$$\boldsymbol{\upsilon}(\mathbf{r}) = \upsilon_x(z)\mathbf{e}_x \qquad . \tag{C.1}$$

For a steady flow clearly $\partial_t \boldsymbol{\upsilon} = 0$ and considering the non-linear term as null, $(\boldsymbol{\upsilon} \cdot \boldsymbol{\nabla})\boldsymbol{\upsilon} = 0$. We rewrite the Navier-Stokes equation with the boundary conditions as

$$\eta \partial_z^2 \upsilon_x(z) = -\rho g \sin \alpha \qquad , \tag{C.2}$$

$$\upsilon_x(0) = 0 \qquad \text{, (no-slip)} \tag{C.3}$$

$$\eta \partial_z \upsilon_x(h) = 0 \qquad \text{, (no stress)} \tag{C.4}$$

this last condition is because there is no viscous stress on the free surface at $z = h$. The result is the half parabola,

$$v_x(z) = \sin\alpha \frac{\rho g}{2\eta}(2h - z)z = \sin\alpha \frac{\rho g h^2}{2\eta}\left(1 - \frac{z}{h}\right)\frac{z}{h} \quad . \tag{C.5}$$

D. Special cross-section cases for Poiseuille flow

D.0.0.1. Case: elliptic cross-section

For an ellipse, Fig. 3.5(a), the boundary curve

$$\partial\mathcal{C}: \quad 1 - \frac{y^2}{a^2} - \frac{z^2}{b^2} = 0 \quad , \tag{D.1}$$

as discussed previously we choose a trial solution, which satisfies the boundary condition, Eq. (3.24) at $\partial\mathcal{C}$ for $\upsilon_x(y,z)$

$$\upsilon_x(y,z) = \upsilon_0\left(1 - \frac{y^2}{a^2} - \frac{z^2}{b^2}\right) \quad , \tag{D.2}$$

and by replacing it in the Navier-Stokes equation, Eq. (3.23), we arrive at

$$\left(\partial_y^2 + \partial_z^2\right)\upsilon_x(y,z) = -\frac{\triangle p}{\eta L} = -2\upsilon_0\left(\frac{1}{a^2} + \frac{1}{b^2}\right) \quad \text{for} \quad (y,z) \in \mathcal{C} \quad , \tag{D.3}$$

and therefore we are able to determine the value for υ_0

$$\upsilon_0 = \frac{\triangle p}{2\eta L}\frac{a^2 b^2}{a^2 + b^2} \quad . \tag{D.4}$$

The problem of computing the respective flow rate Q the problem is then reduced to the problem of evaluating an integral over the area of an ellipse,

$$Q = \int_{\mathcal{C}:\text{ellipse}} \mathrm{d}y\mathrm{d}z \quad , \tag{D.5}$$

By employing cylindrical coordinates $(y,z) \to (\rho,\phi)$, and by using its respective jacobian

determinant $|\partial_{(\rho,\phi)}(y,z)|$ within the limits $0 \leq \rho \leq 1$ and $0 \leq \phi \leq 2\pi$ we obtain

$$y(\rho,\phi) = a\rho\cos\phi \quad , \tag{D.6}$$

$$z(\rho,\phi) = b\rho\sin\phi \quad , \tag{D.7}$$

the velocity then becomes

$$\upsilon_x(\rho,\phi) = \upsilon_0(1-\rho^2) \quad , \tag{D.8}$$

and hence,

$$\int_{\mathcal{C}:\text{ellipse}} \mathrm{d}y\mathrm{d}z = \int_{\mathcal{C}} \mathrm{d}\rho\mathrm{d}\phi \left|\frac{\partial(y,z)}{\partial(\rho,\phi)}\right| = \int_{\mathcal{C}} \mathrm{d}\rho\mathrm{d}\phi \begin{vmatrix} \partial_\rho y & \partial_\rho z \\ \partial_\phi y & \partial_\phi z \end{vmatrix} \quad , \tag{D.9}$$

$$\int_{\mathcal{C}:\text{ellipse}} \mathrm{d}y\mathrm{d}z = ab\int_0^{2\pi}\mathrm{d}\phi\int_0^1 \mathrm{d}\rho\,\rho \quad . \tag{D.10}$$

Therefore, the flow rate is

$$Q = \int_{\mathcal{C}} \mathrm{d}y\mathrm{d}z\upsilon_x(y,z) = ab\int_0^{2\pi}\mathrm{d}\phi\int_0^1 \mathrm{d}\rho\,\rho\,\upsilon_x(\rho,\phi) = \frac{\pi}{4}\frac{1}{\eta L}\frac{a^3b^3}{a^2+b^2}\triangle p \quad . \tag{D.11}$$

D.0.0.2. Case: circular cross-section

By studying the ellipse case, we osbserve the circular one as a specific situation with $a = b$. and hence the trial function for velocity $\upsilon_x(y,z)$ and consequently the flow rate Q, Equations (D.4) and (D.5), originate

$$\upsilon_x(y,z) = \frac{\triangle p}{4\eta L}\Big(a^2 - y^2 - z^2\Big) \quad , \tag{D.12}$$

$$Q = \frac{\pi a^4}{8\eta L}\triangle p \quad . \tag{D.13}$$

The same results can be obtained directly by employing cylindrical coordinates $(x, y, z) = (x, r\cos\phi, r\sin\phi)$, by considering the symmetry along the x direction, $\boldsymbol{\upsilon} = \upsilon_x(r)\mathbf{e}_x$, and taking into account that the Laplacian in cylindrical coordinates is $\nabla^2 = \partial_x^2 + \partial_r^2 + \frac{1}{r}\partial_r + \frac{1}{r^2}\partial_\phi^2$

$$\Big[\partial_r^2 + \frac{1}{r}\partial_r\Big]\upsilon_x(r) = -\frac{\triangle p}{\eta L} \quad , \tag{D.14}$$

whose complete solution is a composition of a general solution for the homogeneous equation, $\upsilon_x'' + \upsilon_x'/r = 0$, and a particular solution to the inhomogeneous equation,

$$\begin{cases} \upsilon_x^{\text{inhom}}(r) = A + B\ln r \quad , \\ \upsilon_x^{\text{hom}}(r) = -(\triangle p/4\eta L)r^2 \quad , \end{cases} \tag{D.15}$$

and with the help of the boundary conditions,

$$\upsilon_x(a) = 0 \quad , \tag{D.16}$$

$$\upsilon_x'(0) = 0 \quad , \tag{D.17}$$

we arrive at

$$\upsilon_x(r,\phi) = \frac{\triangle p}{4\eta L}(a^2 - r^2) \quad , \tag{D.18}$$

$$Q = \int_0^{2\pi} \mathrm{d}\phi \int_0^1 \mathrm{d}r\, r\, \frac{\triangle p}{4\eta L}(a^2 - r^2) = \frac{\pi a^4}{8\eta L}\triangle p \quad . \tag{D.19}$$

D.0.0.3. Case: equilateral triangular cross-section

While there is not an analytical solution for a general triangular shape, we will see that luckily for an equilateral triangular channel, we can arrive at a constant when applying the Navier-Stokes equation to an appropiate trial solution.

Suppose we are considering the geometry in Fig. 3.5c, where the cross-section is formed by the intersection of the three half-planes, $z \geq -\sqrt{3}y$, $z \geq \sqrt{3}y$, and $z \geq -\sqrt{3}y$. We predict the trial function in the following form:

$$\upsilon_x(y,z) = \frac{\upsilon_0}{a^3}\Big(\frac{\sqrt{3}}{2}a - z\Big)\Big(z - \sqrt{3}y\Big)\Big(z + \sqrt{3}y\Big) \quad . \tag{D.20}$$

which clearly satisfies the boundary condition at $\partial\mathcal{C}$. By replacing the above trial solution in the Navier-Stokes equation, we obtain

$$\Big(\partial_y^2 + \partial_z^2\Big)v_x(y,z) = -2\sqrt{3}\frac{v_0}{a^2} \quad , \tag{D.21}$$

which is satisfied by setting $v_0 = \frac{1}{2\sqrt{3}}\frac{\triangle p}{\eta L}a^2$. Finally, we determine the flow rate Q by simple integration over y and then over z,

$$Q = 2\int_0^{\frac{\sqrt{3}}{2}a} \mathrm{d}z \int_0^{\frac{1}{\sqrt{3}}z} \mathrm{d}y v_x(y,z) = \frac{4v_0}{3\sqrt{3}a^3}\int_0^{\frac{\sqrt{3}}{2}a} \mathrm{d}z\Big(\frac{\sqrt{3}}{2}a - z\Big)z^3 \quad , \tag{D.22}$$

arriving finally at,

$$Q = \frac{\sqrt{3}}{320}\frac{a^4}{\eta L}\triangle p \quad . \tag{D.23}$$

Bibliography

[1] George M Whitesides. The origins and the future of microfluidics. *Nature*, 442(7101):368–373, 2006.

[2] Thiago P Segato, Samir A Bhakta, Matthew T Gordon, Emanuel Carrilho, Peter A Willis, Hong Jiao, and Carlos D Garcia. Microfab-less microfluidic capillary electrophoresis devices. *Analytical Methods*, 5(7):1652–1657, 2013.

[3] Chris Backhouse, Marcia Caamano, Frank Oaks, Eric Nordman, Albert Carrillo, Ben Johnson, and Sue Bay. Dna sequencing in a monolithic microchannel device. *Electrophoresis*, 21(1):150–156, 2000.

[4] Henrik Bruus. *Theoretical microfluidics*. Oxford university press Oxford, 2007.

[5] Adam R Abate, Julian Thiele, Marie Weinhart, and David A Weitz. Patterning microfluidic device wettability using flow confinement. *Lab on a Chip*, 10(14):1774–1776, 2010.

[6] Nae Yoon Lee and Bong Hyun Chung. Novel poly (dimethylsiloxane) bonding strategy via room temperature "chemical gluing". *Langmuir*, 25(6):3861–3866, 2009.

[7] Wenli Zhang and Richard E Eitel. Biostability of low-temperature co-fired ceramic materials for microfluidic and biomedical devices. *International Journal of Applied Ceramic Technology*, 9(1):60–66, 2012.

[8] Arduino. Arduino home, 2017. [Online; accessed 14-February-2017].

[9] CFD Direct. Openfoam user guide, 2017.

[10] Hossein Fadaei, John M Shaw, and David Sinton. Bitumen–toluene mutual diffusion coefficients using microfluidics. *Energy & Fuels*, 27(4):2042–2048, 2013.

[11] Tsung-Hua Yang. Recent applications of polyacrylamide as biomaterials. *Recent Patents on Materials Science*, 1(1):29–40, 2008.

[12] WJ Lan, SW Li, JH Xu, and GS Luo. Rapid measurement of fluid viscosity using co-flowing in a co-axial microfluidic device. *Microfluidics and Nanofluidics*, 8(5):687–693, 2010.

[13] Larisa Florea, Cormac Fay, Emer Lahiff, Thomas Phelan, Noel E O'Connor, Brian Corcoran, Dermot Diamond, and Fernando Benito-Lopez. Dynamic ph mapping in microfluidic devices by integrating adaptive coatings based on polyaniline with colorimetric imaging techniques. *Lab on a Chip*, 13(6):1079–1085, 2013.

[14] William D Ristenpart, Jiandi Wan, and Howard A Stone. Enzymatic reactions in microfluidic devices: Michaelis- menten kinetics. *Analytical chemistry*, 80(9):3270–3276, 2008.

[15] Staffan L Sjostrom, Haakan N Joensson, and Helene Andersson Svahn. Multiplex analysis of enzyme kinetics and inhibition by droplet microfluidics using picoinjectors. *Lab on a Chip*, 13(9):1754–1761, 2013.

[16] Hoyoung Yun, Kisoo Kim, and Won Gu Lee. Cell manipulation in microfluidics. *Biofabrication*, 5(2):022001, 2013.

[17] Zhigang Wu, Ben Willing, Joakim Bjerketorp, Janet K Jansson, and Klas Hjort. Soft inertial microfluidics for high throughput separation of bacteria from human blood cells. *Lab on a Chip*, 9(9):1193–1199, 2009.

[18] Weijia Zhang, Kazuharu Kai, Dong Soon Choi, Takayuki Iwamoto, Yen H Nguyen, Helen Wong, Melissa D Landis, Naoto T Ueno, Jenny Chang, and Lidong Qin. Microfluidics separation reveals the stem-cell–like deformability of tumor-initiating cells. *Proceedings of the National Academy of Sciences*, 109(46):18707–18712, 2012.

[19] Ali Asgar S Bhagat, Hansen Bow, Han Wei Hou, Swee Jin Tan, Jongyoon Han, and Chwee Teck Lim. Microfluidics for cell separation. *Medical & biological engineering & computing*, 48(10):999–1014, 2010.

[20] A Valero, JN Post, JW Van Nieuwkasteele, PM Ter Braak, W Kruijer, and A Van Den Berg. Gene transfer and protein dynamics in stem cells using single cell electroporation in a microfluidic device. *Lab on a Chip*, 8(1):62–67, 2008.

[21] Lin Luan, Matthew W Royal, Randall Evans, Richard B Fair, and Nan M Jokerst. Chip scale optical microresonator sensors integrated with embedded thin film photodetectors on electrowetting digital microfluidics platforms. *IEEE Sensors Journal*, 12(6):1794–1800, 2012.

[22] Richard B Fair. Digital microfluidics: is a true lab-on-a-chip possible? *Microfluidics and Nanofluidics*, 3(3):245–281, 2007.

[23] Daniel J Laser and Juan G Santiago. A review of micropumps. *Journal of micromechanics and microengineering*, 14(6):R35, 2004.

[24] Vijay Srinivasan, Vamsee K Pamula, and Richard B Fair. An integrated digital microfluidic lab-on-a-chip for clinical diagnostics on human physiological fluids. *Lab on a Chip*, 4(4):310–315, 2004.

[25] Petra S Dittrich and Andreas Manz. Lab-on-a-chip: microfluidics in drug discovery. *Nature Reviews Drug Discovery*, 5(3):210–218, 2006.

[26] Jamil El-Ali, Peter K Sorger, and Klavs F Jensen. Cells on chips. *Nature*, 442(7101):403–411, 2006.

[27] B Bilenberg, Theodor Nielsen, B Clausen, and Anders Kristensen. Pmma to su-8 bonding for polymer based lab-on-a-chip systems with integrated optics. *Journal of Micromechanics and Microengineering*, 14(6):814, 2004.

[28] Eric K Sackmann, Anna L Fulton, and David J Beebe. The present and future role of microfluidics in biomedical research. *Nature*, 507(7491):181–189, 2014.

[29] Teruo Fujii. Pdms-based microfluidic devices for biomedical applications. *Microelectronic Engineering*, 61:907–914, 2002.

[30] J Cooper McDonald and George M Whitesides. Poly (dimethylsiloxane) as a material for fabricating microfluidic devices. *Accounts of chemical research*, 35(7):491–499, 2002.

[31] Majid Ebrahimi Warkiani, Lidan Wu, Andy Kah Ping Tay, and Jongyoon Han. Large-volume microfluidic cell sorting for biomedical applications. *Annual review of biomedical engineering*, 17:1–34, 2015.

[32] AC Dagger and JA Semlyen. Studies of cyclic and linear poly (dimethylsiloxanes): 33. preparation and characterization of per-deuterated linears and cyclics. *Polymer*, 39(12):2621–2627, 1998.

[33] Dong Qin, Younan Xia, and George M. Whitesides. Soft lithography for micro- and nanoscale patterning. *Nat. Protocols*, 5(3):491–502, Mar 2010.

[34] Dong Qin, Younan Xia, and George M Whitesides. Rapid prototyping of complex structures with feature sizes larger than 20 μm. *Advanced Materials*, 8(11):917–919, 1996.

[35] How to choose the right photomask to fabricate your su-8 microfluidic mold.

[36] Teri W Odom, J Christopher Love, Daniel B Wolfe, Kateri E Paul, and George M Whitesides. Improved pattern transfer in soft lithography using composite stamps. *Langmuir*, 18(13):5314–5320, 2002.

[37] Younan Xia, Jabez J McClelland, Rajeev Gupta, Dong Qin, Xiao-Mei Zhao, Lydia L Sohn, Robert J Celotta, and George M Whitesides. Replica molding using polymeric materials: A practical step toward nanomanufacturing. *Advanced Materials*, 9(2):147–149, 1997.

[38] Lmf-laboratory of microfabrication.

[39] Sung-Min Lee, Seung Hwa Oh, and Kyung Cheol Choi. Highly transparent su-8 photoresist barrier rib for a transparent ac plasma display panel. *Journal of Display Technology*, 7(1):40–43, 2011.

[40] Products and facilities.

[41] Down corning, silicon-based technology.

[42] Cnpem-laboratory of microfabrication/facilities.

[43] Will Patrick. Open source syringe pump, 2003.

[44] Harvardapparatus / standard infuse syringe pumps for microfluidics.

[45] Ne-1002x programmable microfluidics syringe pump.

[46] Stepper motor wikipedia. Steeper motor, 2017.

[47] 1.8º motor stepper motor specialist.

[48] Pololu Robotics and Electronics. Drv8825 stepper motor driver carrier, high current.

[49] 3D printer. Tato equipamentos eletrônicos, 2015.

[50] Clifford Wolf Marius Kintel. Openscad, the programmers solid 3d cad modeller.

[51] 700 series microliter syringes.

[52] Pierre-Gilles De Gennes, Françoise Brochard-Wyart, and David Quéré. *Capillarity and wetting phenomena: drops, bubbles, pearls, waves*. Springer Science & Business Media, 2013.

[53] Detergents and soups.

[54] Josefa Bastida-Rodríguez. The food additive polyglycerol polyricinoleate (e-476): structure, applications, and production methods. *ISRN Chemical Engineering*, 2013, 2013.

[55] Laurier L Schramm. *Emulsions, foams, suspensions, and aerosols: microscience and applications*. John Wiley & Sons, 2014.

[56] Eric Dickinson and Pieter Walstra. *Food colloids and polymers: stability and mechanical properties*. Elsevier, 1993.

[57] Ayten Sagiroglu, Hakki Mevlut Ozcan, Sebnem Selen Isbilir, Hatice Paluzar, and Neslihan M Toprakkiran. Alkali catalysis of different vegetable oils for comparisons of their biodiesel productivity. 2013.

[58] Pieter Walstra. Principles of emulsion formation. *Chemical Engineering Science*, 48(2):333–349, 1993.

[59] EE Isaacs, RS Chow, and LL Schramm. Emulsions: Fundamentals and applications in the petroleum industry. *Advances in Chemistry Series*, 231, 1992.

[60] M. Matos, G. Gutiérrez, J. Coca, and C. Pazos. Preparation of water-in-oil-in-water (w1/o/w2) double emulsions containing trans-resveratrol. *Colloids and Surfaces A: Physicochemical and Engineering Aspects*, 442:69 – 79, 2014. Selected papers from the 26th European Colloid and Interface Society conference (26th {ECIS} 2012).

[61] HF Bamford, KJ Gardner, GR Howat, and AF Thomson. use of polyglycerol polyricinoleate in chocolate. *Revue internationale de la chocolaterie*, 1970.

[62] R Wilson, BJ Van Schie, and D Howes. Overview of the preparation, use and biological studies on polyglycerol polyricinoleate (pgpr). *Food and Chemical Toxicology*, 36(9):711–718, 1998.

[63] Mark Stewart Taylor. *Stabilisation of water-in-oil emulsions to improve the emollient properties of lipstick*. PhD thesis, University of Birmingham, 2011.

[64] Andrés L Márquez, Alejandra Medrano, Luis A Panizzolo, and Jorge R Wagner. Effect of calcium salts and surfactant concentration on the stability of water-in-oil (w/o) emulsions prepared with polyglycerol polyricinoleate. *Journal of colloid and interface science*, 341(1):101–108, 2010.

[65] International union of pure and applied chemistry.

[66] DL Nelson. i cox, mm" lehninger principles of biochemistry"(2013), 2013.

[67] J.M. Berg, J.L. Tymoczko, and L. Stryer. *Biochemistry, Seventh Edition*. W.H. Freeman, 2012.

[68] Polyacrylamide.

[69] J Marmur and POP Ts'o. Denaturation of deoxyribonucleic acid by formamide. *Biochimica et biophysica acta*, 51(1):32–36, 1961.

[70] Acrylamide for molecular biology.

[71] Wikipedia. Acrylamide — wikipedia, the free encyclopedia, 2017. [Online; accessed 8-February-2017].

[72] Samuel Raymond. Acrylamide gel electrophoresis. *Annals of the New York Academy of Sciences*, 121(1):350–365, 1964.

[73] Richard P Pohanish. *Sittig's handbook of toxic and hazardous chemicals and carcinogens*. William Andrew, 2008.

[74] Wikipedia. Polyacrylamide gel electrophoresis — wikipedia, the free encyclopedia, 2017. [Online; accessed 8-February-2017].

[75] Sds-page.

[76] Charly Gaul, Hans-Christoph Diener, and Ulrich Danesch. Improvement of migraine symptoms with a proprietary supplement containing riboflavin, magnesium and q10: a randomized, placebo-controlled, double-blind, multicenter trial. *The journal of headache and pain*, 16(1):32, 2015.

[77] Raymond P Goodrich, A RICHARD, DENISE I GILMOUR, JUNZHI LI, CHRISTOPHER B MARTIN, and S MATTHEW. The antiviral and antibacterial properties of riboflavin and light: Applications to blood safety and transfusion medicine. *Flavins: Photochemistry and Photobiology*, 6:83, 2006.

[78] Vijay Kumar, Owen Lockerble, Shawn D Kell, Patrick H Ruane, Matthew S Platz, Christopher B Martin, Jean-Luc Ravanat, Jean Cadet, and Raymond P Goodrich. Riboflavin and uv-light based pathogen reduction: extent and consequence of dna damage at the molecular level. *Photochemistry and photobiology*, 80(1):15–21, 2004.

[79] Patrick H Ruane, Richard Edrich, Deanna Gampp, Shawn D Keil, R Lynne Leonard, and Raymond P Goodrich. Photochemical inactivation of selected viruses and bacteria in platelet concentrates using riboflavin and light. *Transfusion*, 44(6):877–885, 2004.

[80] Marta Orlowska, Tatiana Koutchma, Michael Grapperhaus, John Gallagher, Raymond Schaefer, and Cheryl Defelice. Continuous and pulsed ultraviolet light for nonthermal treatment of liquid foods. part 1: effects on quality of fructose solution, apple juice, and milk. *Food and Bioprocess Technology*, 6(6):1580–1592, 2013.

[81] Marta Orlowska, Tatiana Koutchma, Michael Grapperhaus, John Gallagher, Raymond Schaefer, and Cheryl Defelice. Continuous and pulsed ultraviolet light for nonthermal treatment of liquid foods. part 1: Effects on quality of fructose solution, apple juice, and milk. *Food and Bioprocess Technology*, 6(6):1580–1592, 2013.

[82] Richard K Haynes, Simone C Vonwiller, and Matthew R Luderer. Tetramethylethylenediamine. *e-EROS Encyclopedia of Reagents for Organic Synthesis*, 2004.

[83] Temed.

[84] Kenneth W Henderson, Andrea E Dorigo, Qi-Yong Liu, and Paul G Williard. Effect of polydentate donor molecules on lithium hexamethyldisilazide aggregation: An x-ray crystallographic and a combination semiempirical pm3/single point ab initio theoretical study. *Journal of the American Chemical Society*, 119(49):11855–11863, 1997.

[85] K König, H Seidel, M Afshar, M Klötzer, D Feili, and M Straub. 1 nanoprocessing using near-infrared sub-15 femtosecond laser microscopes. *Optically Induced Nanostructures: Biomedical and Technical Applications*, page 3, 2015.

[86] Wikipedia. polydimethylsiloxane, 2017. [Online; accessed 10-February-2017].

[87] James E Mark, Harry R Allcock, and Robert West. *Inorganic polymers*. Oxford University Press, 2005.

[88] JC Lötters, W Olthuis, PH Veltink, and P Bergveld. The mechanical properties of the rubber elastic polymer polydimethylsiloxane for sensor applications. *Journal of Micromechanics and Microengineering*, 7(3):145, 1997.

[89] Joel H Ferziger, Milovan Peric, and Anthony Leonard. Computational methods for fluid dynamics, 1997.

[90] Caio Martins. Fluid distribution optimization in porous media using leaf venation patterns. Master's thesis, University of Sao Paulo - Institute of Physics, Institute of Physics - USP, Brazil, 2017.

[91] Andrew Jackson. A comprehensive tour of snappyhexmesh, 7th openfoam workshop, 2012.

[92] Cyril W Hirt and Billy D Nichols. Volume of fluid (vof) method for the dynamics of free boundaries. *Journal of computational physics*, 39(1):201–225, 1981.

[93] Processing community. The processing software, free and open source„ 2017.